

AD-753 168

APPLICATION OF NONLINEAR INTERACTIONS IN  
ACOUSTIC MEDIA TO MICROWAVE SIGNAL PRO-  
CESSING DEVICES

Michael Waldner

Hughes Research Laboratories

Prepared for:

Rome Air Development Center

November 1972

DISTRIBUTED BY:

**NTIS**

National Technical Information Service  
U. S. DEPARTMENT OF COMMERCE  
5285 Port Royal Road, Springfield Va. 22151

AD 753168

RADC-TR-72-276  
Final Technical Report  
November 1972



APPLICATION OF NONLINEAR INTERACTIONS IN ACOUSTIC MEDIA  
TO MICROWAVE SIGNAL PROCESSING DEVICES

Hughes Research Laboratories

Approved for public release;  
distribution unlimited.

NOT FOR TECHNICAL  
REPRODUCTION

Rome Air Development Center  
Air Force Systems Command  
Griffiss Air Force Base, New York

UNCLASSIFIED

Security Classification

DOCUMENT CONTROL DATA - R & D

(Security classification of title, body of abstract and indexing annotation must be entered when the overall report is classified)

1. ORIGINATING ACTIVITY (Corporate author) Hughes Research Laboratories Malibu, California 90265		2a. REPORT SECURITY CLASSIFICATION UNCLASSIFIED	
		2b. GROUP N/A	
3. REPORT TITLE APPLICATION OF NONLINEAR INTERACTIONS IN ACOUSTIC MEDIA TO MICROWAVE SIGNAL PROCESSING DEVICES			
4. DESCRIPTIVE NOTES (Type of report and inclusive dates) Final Report			
5. AUTHOR(S) (First name, middle initial, last name) Michael Waldner, et al			
6. REPORT DATE November 1972		7a. TOTAL NO. OF PAGES <del>108</del> 116	7b. NO. OF REFS 11
8a. CONTRACT OR GRANT NO F30602-71-C-0196  Job Order No. 55730702		8b. ORIGINATOR'S REPORT NUMBER(S) None	
		9b. OTHER REPORT NO(S) (Any other numbers that may be assigned this report) RADC-TR-72-276	
10. DISTRIBUTION STATEMENT Approved for public release; distribution unlimited.			
11. SUPPLEMENTARY NOTES RADC Project Engineer: Henry Friedman (OCTE) AC 315 330-4251		12. SPONSORING MILITARY ACTIVITY Rome Air Development Center (OCTE) Griffiss Air Force Base, New York 13441	
13. ABSTRACT  Nonlinear interactions of surface waves in acoustic media can lead to the implementation of a number of signal processing functions. The work under this contract was directed toward the implementation of the convolution function using piezoelectric crystals, primarily lithium niobate, as the acoustic medium. The objective was to obtain broadband operation, to minimize spurious signals, to characterize the devices in this mode of operation, and to evolve a design theory for these devices. The development of suitable broadband input transducers and the design of the coupling structure were both major elements of the effort. Three devices were delivered as a result of the work; prime concentration was directed toward completion of a broadband device encompassing the frequency range of 95 to 180 MHz, with a convolution time of 15 $\mu$ sec. Narrower band devices operating at 195 MHz center frequency with a convolution time of 15 $\mu$ sec and at 146 MHz with a convolution time of 8 $\mu$ sec were also delivered.  Details of illustrations in this document may be better studied on microfiche.			

DD FORM 1473  
1 NOV 66

I

UNCLASSIFIED

Security Classification

14. KEY WORDS	LINK A		LINK B		LINK C	
	ROLE	WT	ROLE	WT	ROLE	WT
Microwave Acoustics Ultrasonic Surface Waves Lithium Niobate Nonlinear Surface Waves Signal Processing Signal Correlation Convolution Pulse Compression						

**APPLICATION OF NONLINEAR INTERACTIONS IN ACOUSTIC MEDIA  
TO MICROWAVE SIGNAL PROCESSING DEVICES**

**Michael Waldner  
et al**

**Hughes Research Laboratories**

**Approved for public release;  
distribution unlimited.**

FOREWORD

This Final Report was prepared at Hughes Research Laboratories, Malibu, California, under contract F30602-71-C-0196, Job Order Number 55730702, for Rome Air Development Center, Griffiss Air Force, New York. Mr. Henry Friedman (OCTE) was the RADC Project Engineer.

This report has been reviewed by the RADC Information Office (OI) and is releasable to the National Technical Information Office (NTIS).

This technical report has been reviewed and is approved.

*Henry Friedman*  
Approved: HENRY FRIEDMAN  
Project Engineer  
Electron Devices Section

*Arthur J. Frohlich*  
Approved: ARTHUR J. FROHLICH  
Chief, Techniques Branch  
Surveillance & Control Division

FOR THE COMMANDER: *Fred I. Diamond*  
FRED I. DIAMOND  
Chief, Plans Office

## EVALUATION MEMO ON FINAL REPORT

The work under this contract resulted in the development and evaluation of experimental model devices employing a new approach for performing signal processing functions such as correlation, convolution, pulse compression, time delay, etc. These devices utilize the nonlinear interactions of surface acoustic waves and have inherent advantages of small size, light weight, low cost, and high reliability. Surface acoustic wave devices will make possible improved signal processing functions in USAF radar and communication systems. The work was in support of TPO 18.

*Henry Friedman*

HENRY FRIEDMAN  
PROJECT ENGINEER  
ELECTRON DEVICES SECTION

## TABLE OF CONTENTS

	ABSTRACT . . . . .	iii
	LIST OF ILLUSTRATIONS . . . . .	vii
1.	INTRODUCTION . . . . .	1
2.	NONLINEAR INTERACTION DEVICES: BACKGROUND . . . . .	3
3.	EXPERIMENTAL AND THEORETICAL INVESTIGATION OF NONLINEAR INTERACTION DEVICES . . . . .	11
	3.1 Choice of Materials . . . . .	11
	3.2 Transducer Design . . . . .	14
	3.3 Elimination of Spurious Signals . . . . .	27
	3.4 Design Parameters . . . . .	39
	3.5 Time Distortion . . . . .	49
	3.6 Coarse Grating Couplers . . . . .	52
	3.7 Diffraction Effects . . . . .	60
	3.8 Propagation Losses . . . . .	64
	3.9 Dispersion Effects . . . . .	65
4.	DEVELOPMENT OF ELECTRONIC MEASUREMENT APPARATUS . . . . .	73
	4.1 Autoconvolution Apparatus . . . . .	73
	4.2 Coarse Grating Test Apparatus . . . . .	76
	4.3 FM CHIRP Test Apparatus . . . . .	79
5.	DELIVERED DEVICES . . . . .	85
	REFERENCES . . . . .	93
	APPENDIX — General Aperiodic Transducer Design: Nonaperture Weighted . . . . .	95
	DD FORM 1473 . . . . .	109

## LIST OF ILLUSTRATIONS

Fig. 1.	Surface Wave Nonlinear Interactions . . . .	4
Fig. 2.	Surface Wave Nonlinear Interactions . . . .	5
Fig. 3.	Signal Processing Modes: Convolution Operation . . . . .	7
Fig. 4.	Signal Processing Modes: Correlation Operation . . . . .	7
Fig. 5.	Signal Processing Modes: Variable Time Delay Operation . . . . .	8
Fig. 6.	Signal Processing Modes: Pulse Operation . . . . .	9
Fig. 7.	Broadband Surface Wave Delay Line . . . . .	17
Fig. 8.	Computed and Measured Insertion Loss for 40% Bandwidth . . . . .	17
Fig. 9.	Comparison of Computed and Measured Insertion Loss for an Octave-Bandwidth Nondispersive Delay Line . . . . .	20
Fig. 10.	Measured Performance of 95 to 180 MHz Broadband Convolver . . . . .	22
Fig. 11.	Broadband Design Results for 21 $\mu$ sec Delay . . . . .	26
Fig. 12.	Delay Line Insertion Loss: Modified Broadband Design . . . . .	26
Fig. 13.	Rectangular Plate Coupler with Periodic Input Transducers on Y-Cut Z-Propagating Lithium Niobate . . . . .	28
Fig. 14.	Surface Wave Convolution Filter Showing Spurious Signals . . . . .	29
Fig. 15.	Details of Spurious Signal with Rectangular Coupling Plate . . . . .	30
Fig. 16.	Parallelopiped Coupling Plate . . . . .	32

Fig. 17.	Averaging Effect of Angled Ends of Parallelopiped . . . . .	32
Fig. 18.	Results with Parallelopiped Plate . . . . .	33
Fig. 19.	Broadband Convolution Filter Schematic . . . . .	34
Fig. 20.	Pulse Distortion in Broadband Convolution Filter . . . . .	35
Fig. 21.	Bulk Wave Generation Effect . . . . .	36
Fig. 22.	Suppression of Bulk Wave Interference . . . . .	38
Fig. 23.	Bulk Wave Suppression . . . . .	38
Fig. 24.	Convolver Configuration: Geometrical Signals . . . . .	40
Fig. 25.	Equivalent Circuit of Convolver . . . . .	41
Fig. 26.	Convolver Design Equations . . . . .	43
Fig. 27.	Results of Design Analysis . . . . .	44
Fig. 28.	Measured Performance of 95 to 180 MHz Broadband Convolver . . . . .	45
Fig. 29.	Measured Performance of 45 to 90 MHz Broadband Convolver . . . . .	47
Fig. 30.	Narrow Band, Plate Coupled Convolution Filter . . . . .	50
Fig. 31.	Time Distortion in Plate Coupled Convolver . . . . .	53
Fig. 32.	Coarse Grating Constructions . . . . .	53
Fig. 33.	Transmission through Coarse Grating . . . . .	55
Fig. 34.	Mounted Coarse Grating Convolver . . . . .	58
Fig. 35.	Coarse Grating Conversion Factor . . . . .	59
Fig. 36.	Time Distortion in Coarse Grating Coupler . . . . .	61
Fig. 37.	Schematic Representation of Beam Spreading . . . . .	61

Fig. 38.	Dispersion Curves for an Aluminum Film on Y-Z Lithium Niobate and ST Quartz . . . . .	66
Fig. 39.	Pulse Distortion caused by Dispersion in Surface Wave Correlation . . . . .	68
Fig. 40.	Phase Velocity and Propagation Loss for SiO <sub>2</sub> Film on Lithium Niobate . . . . .	72
Fig. 41.	Plate Coupled Convolver Test Apparatus . . . . .	74
Fig. 42.	Two-Input Acoustic Surface Wave Correlator Test Setup . . . . .	78
Fig. 43.	Pulse Compression Test Schematic . . . . .	81
Fig. 44.	Pulse Compression using Electronic Generation of CHIRP Signal and Convolver for Compression . . . . .	84
Fig. 45.	Broadband Plate Coupled Convolver. . . . .	86
Fig. 46.	Delay Line Insertion Loss . . . . .	89
Fig. 47.	Delay Line Insertion Loss . . . . .	89
Fig. 48.	Broadband Convolver . . . . .	90
Fig. 49.	Narrow Band Convolver . . . . .	91
Fig. 50.	Narrow Band Convolver . . . . .	92

## 1. INTRODUCTION

The goal of this program was to design and fabricate experimental models of microwave signal processing devices embodying nonlinear interaction of surface acoustic waves. The program was directed at realizing three signal processing functions: convolution, variable time delay, and pulse compression. As a consequence of the results obtained early in the program, the major thrust became the development of a broadband convolution filter with large time-bandwidth product, the determination of the qualitative design criteria for the device, the development of constructions that would minimize the presence of signal distorting outputs due to spurious signals, and the detailed design of broadband input and output transducers which would give a flat frequency response. Devices with two types of coupling structures were tested; these were a plate coupled structure and a coarse grating coupling structure. The goal of the program was to deliver devices that would accommodate an integration time of 15  $\mu$ sec for the convolution integral. These devices can also be used in the variable time delay mode and as pulse compression filters. An understanding of the limitations of the device in these modes of operation was developed; details are included in this report.  $\text{LiNbO}_3$  and  $\text{Bi}_{12}\text{GeO}_{20}$  devices were tested early in the program. On the basis of results obtained, a decision was made to concentrate the efforts on Y-cut, Z-propagating lithium niobate. This material showed conversion efficiencies as good as the bismuth germanium oxide with other incidental advantages. Namely, it shows acoustic beam focusing properties which limit diffraction losses and has a higher surface wave propagation velocity, which allows a larger bandwidth for given limitations in the minimum size of the fingers in the input and output interdigital surface wave transducers.

Three devices were delivered to RADC under this program:

- A large bandwidth (95 to 180 MHz) convolver with a maximum integration time of 15  $\mu$ sec. This device employed an aperture weighted linear FM transducer design based upon that suggested in our original proposal but modified to give a more nearly flat frequency response.

- A moderate bandwidth (20% at 145 MHz) design using simple periodic input transducers with an integration time of 15  $\mu$ sec. This design gives a smaller insertion loss than the broadband design.
- A 14% bandwidth (at 195 MHz) design with an integration time of 3  $\mu$ sec. This device was largely optimized in the direction of providing the minimum insertion loss at the sacrifice of some bandwidth and integration time.

As might be expected, the program has resulted in the definition of some areas in which further work could be done to improve the performance and the characterization of this class of devices. These areas are:

- Methods for improving conversion efficiencies.
- Further optimization of the device for the specific functions of variable time delay and pulse compression.
- Operation of the device in other modes, specifically as a time reversal filter.
- Experimental characterization of the phase transfer characteristics of the device.

Results accomplished under Contract F30602-71-C-0196 were augmented by Hughes funded research directly related to the nonlinear filter, the prime subject of this contract effort. Therefore, this report includes some results obtained in the parallel effort that were applied to the construction and test of several subject devices. Precisely, this includes development of the test setup for pulse compression, the basic studies on general aperiodic structures and the experimental test of the delay line based on this approach (specific designs were obtained under the contract), some of the experimental work on the highly periodic coarse grating structure, and the iterative modification of the aperture weighted transducer to effect flat frequency response.

## 2. NONLINEAR INTERACTION DEVICES: BACKGROUND

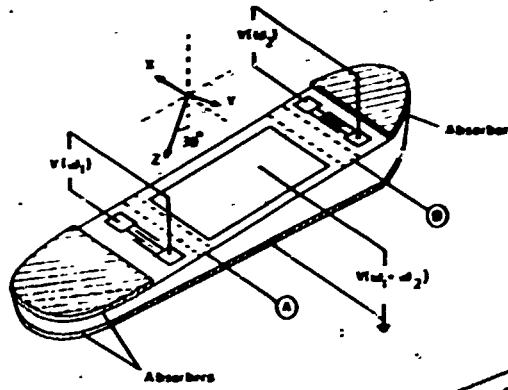
As a basis for the further discussion of the work on this program, the mode of operation of the devices is summarized in this section.

Svaasand<sup>1</sup> demonstrated the nonlinear interaction of surface waves for the configurations shown in Fig. 1. The significant point is that for both input signals at a frequency  $\omega$  on the end interdigital transducers, a signal is observed on the central plate at a frequency of  $2\omega$ . This output signal is a consequence of the nonlinearity of the acoustic medium in which a polarization is produced by the acoustic surface waves near the surface, which is determined by the square of the elastic strain. If, at a given place under the central plate, strains produced by the two input signals are overlapping, a polarization proportional to the product of the strains is produced. It is this multiplication due to the strain that produces frequency doubling. Moreover, since the input signals travel under the plate and the signals introduced over a period of time are present under the plate, the plate also performs an integration over time.

Luukkala and Kino<sup>2</sup> have reported similar devices as shown in Fig. 2. The device in Fig. 2(a) is essentially similar to Svaasand's, while the device in Fig. 2(b) shows a coarse interdigital finger transducer in the central section. The upper device gives an output on the plate at a frequency  $2\omega$  for interacting signals imposed on the end transducers at  $\omega$ . The grating structure allows the use of two different input frequencies,  $\omega_1$  and  $\omega_2$ , with an output at the sum frequency. The difference between  $\omega_1$  and  $\omega_2$  is determined by the periodicity of the central transducer, where  $\omega_1 - \omega_2 = (2\pi/\ell)V_S$ ,  $V_S$  is the surface wave velocity and  $\ell$  is the finger-pair spacing.

Luukkala<sup>3</sup> has constructed the strip coupler structure of Fig. 2(c). In this case, the lateral field generated by the nonlinearity is detected. This will work only on some crystal cuts; for instance, Y-cut Z-propagation  $\text{LiNbO}_3$  is not appropriate.

1342-34



Reproduced from  
best available copy. C

**SIDE VIEW**  
All measures  
in mm

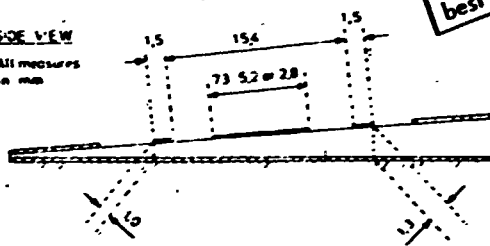
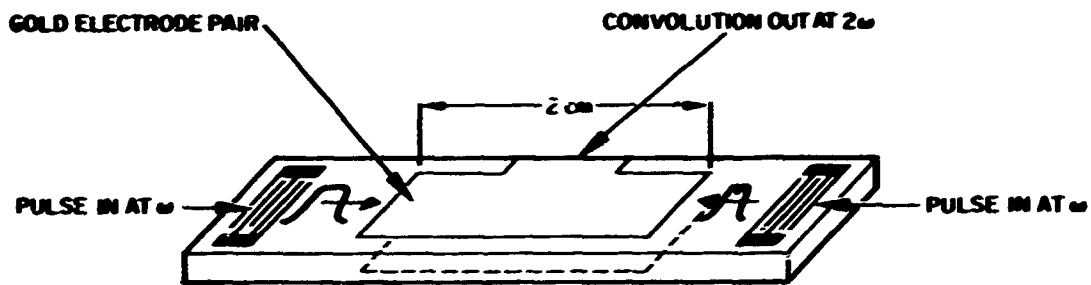
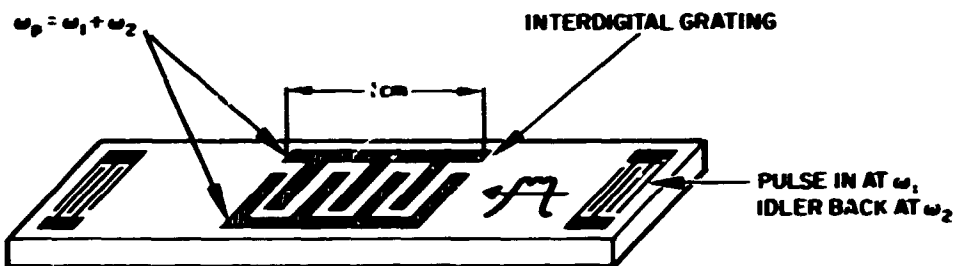


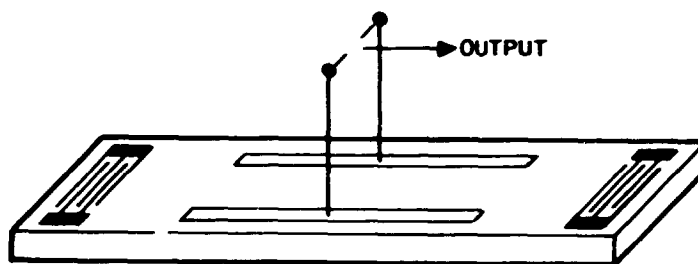
Fig. 1.  
Surface Wave Nonlinear Inter-  
actions (Svaasand).



(a) YZ-CUT  $\text{LiNbO}_3$  DELAY ROD



(b) YZ-CUT  $\text{LiNbO}_3$  DELAY ROD



(c) STRIP COUPLER (LUUKKALA)

Fig. 2. Surface Wave Nonlinear Interactions (Luukkala and Kino).

Kino and Luukkala<sup>2</sup>, Shaw<sup>4</sup>, and Quate and Thompson<sup>5</sup> originally discussed the signal processing implications of these types of devices.\*

The basic operation is the convolution operation shown in Fig. 3. Acoustic surface waves generated at the two end transducers travel toward the center, eventually start to overlap, cross, and then separate. Because the waves are traveling in different directions, the envelope of one of the signals undergoes a time reversal with respect to the other. As a consequence, the output becomes the convolution of the two input functions, rather than their correlation.

In order to attain a correlation of two signals, the procedure in Fig. 4 may be employed. In this case, one of the signals has been time reversed elsewhere. Now the output is the correlation of the two signals instead of the convolution.

For the special case of a linear FM CHIRP signal, it is possible to time reverse the signal by electronic means, mixing it with a higher frequency than using the lower side band of the mixer output to generate the time reversed signal.

Figure 5 shows that, used as a convolution filter, the device may be used to obtain a variable time delay. The input pulse is put in on one transducer, a narrow pulse of variable timing on the other transducer, and a delayed pulse that is also narrowed in time is obtained in the central region. The time delay produced depends upon the time difference between the two signal inputs. This operation does not correspond to setting a variable time delay unless the narrow pulse timing is synchronized with the signal pulse.

Figure 6 shows the pulse compression operation, which has been demonstrated by W. L. Bongianni<sup>6</sup>. Essentially, pulse compression is obtained by convolving a frequency modulated signal with its time reversed signal. In our work, pulse compression was demonstrated by using electronic time inversion of a linear FM signal developed by a voltage controlled oscillator.

---

\* Also, W. C. Wang, "A Convolution Integrator" presented at Joint Services Technical Advisory Comm., p1B, (1966).

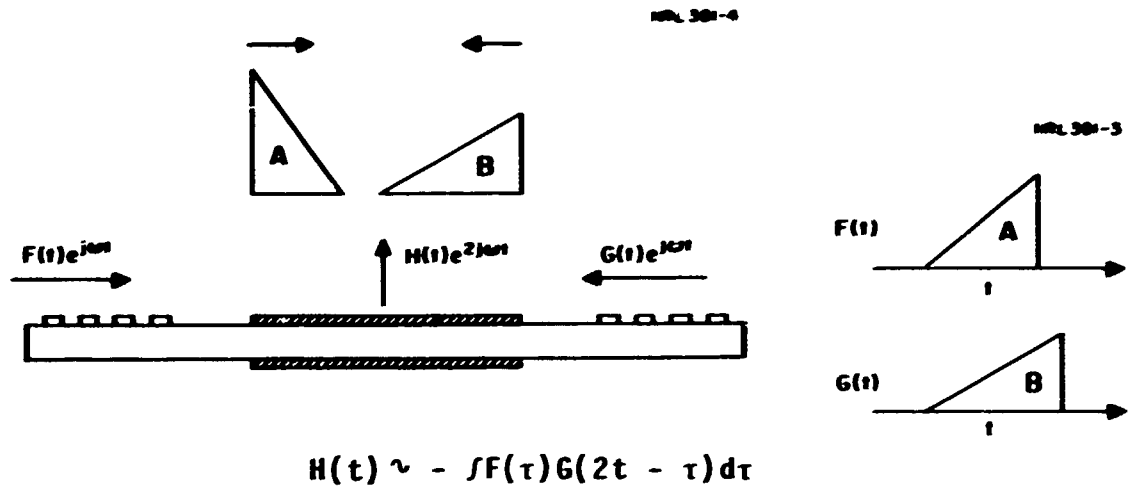


Fig. 3. Signal Processing Modes - Convolution Operation.

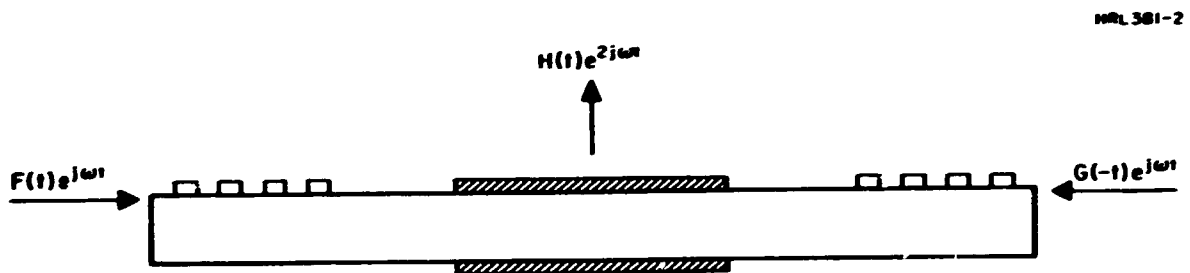
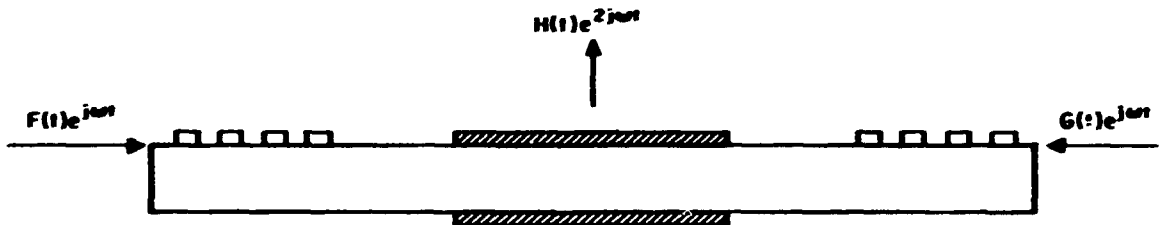


Fig. 4. Signal Processing Modes - Correlation Operation.



$$H(t) \sim \int F(\tau) G(2t - \tau) d\tau$$

$$\text{Let } G(2t - \tau) = \delta(t_0)$$

$$H(t) = F(2t - t_0)$$

Signal delay =  $\frac{t_0}{2}$ ,  
 signal narrowed by 2

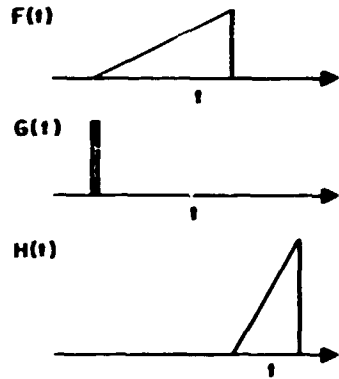
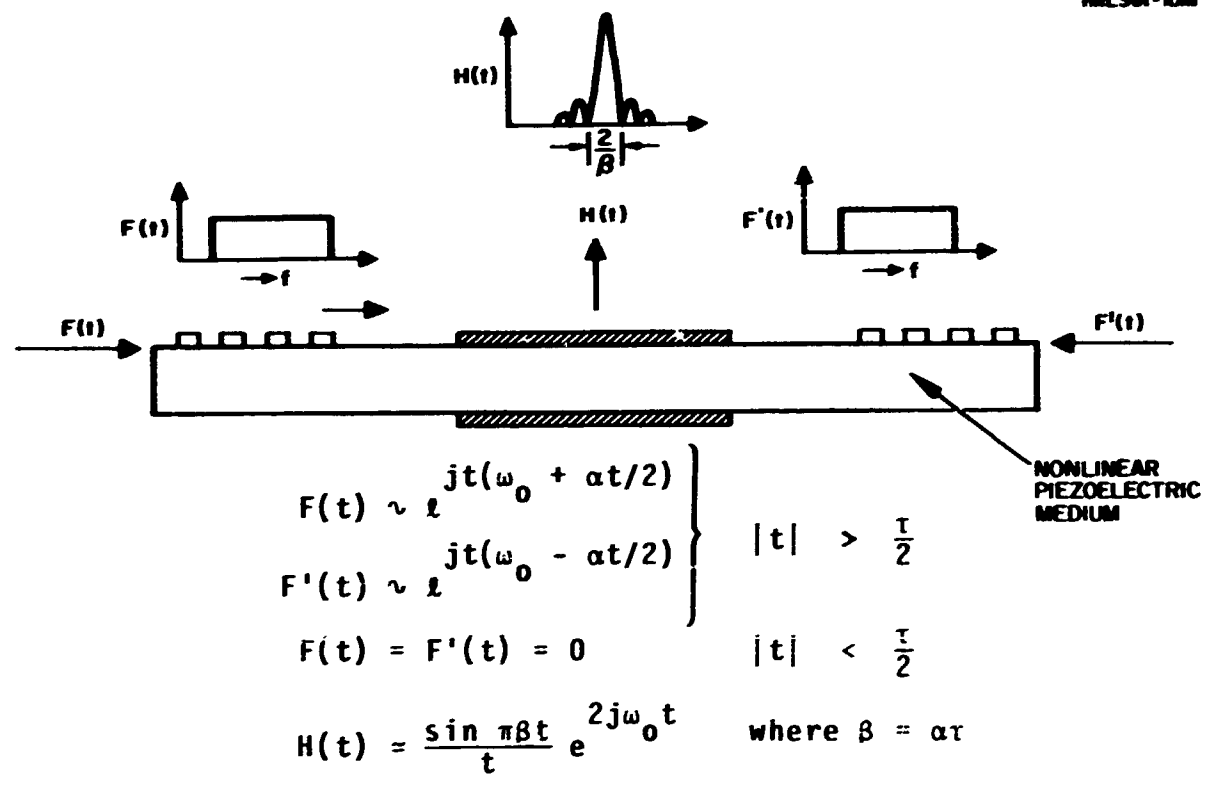
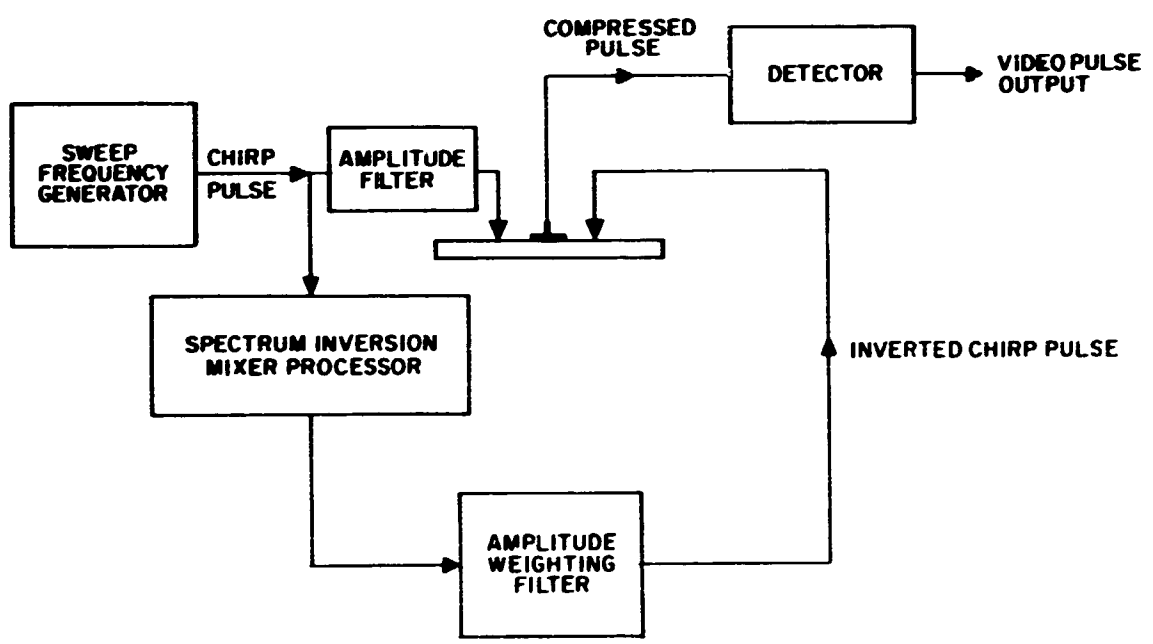


Fig. 5. Signal Processing Modes - Variable time Delay Operation.



(a) Pulse Compression Operation



(b) Pulse Compression System.

Fig. 6. Signal Processing Modes - Pulse Compression.

### 3. EXPERIMENTAL AND THEORETICAL INVESTIGATION OF NONLINEAR INTERACTION DEVICES

#### 3.1 CHOICE OF MATERIALS

In order to test the conversion efficiency obtainable for  $\text{Bi}_{12}\text{GeO}_{20}$  and for Y-cut Z propagating lithium niobate, four devices were constructed with the objective of testing the conversion efficiency of the two materials.

- A  $\text{Bi}_{12}\text{GeO}_{20}$  filter with a 5  $\mu\text{sec}$  coupling region. The center frequency of the 20-finger-pair periodic input transducer was 50 MHz. The device is on the  $\langle 111 \rangle$  cut with propagation in the (110) direction. The aperture of the transducer was 37.5 acoustic wavelength in this and in the following devices.
- A similar  $\text{Bi}_{12}\text{GeO}_{20}$  filter on  $\langle 100 \rangle$  cut  $\text{Bi}_{12}\text{GeO}_{20}$  with propagation in the (110) direction.
- A lithium niobate filter with an 8.5  $\mu\text{sec}$  coupling region on a sample of Y-cut Z-propagating lithium niobate with input transducers centered at 50 MHz.
- A Y-cut Z-propagating lithium niobate filter with a 4.5  $\mu\text{sec}$  coupling region (using a 9  $\mu\text{sec}$  delay line) with input transducers centered at 100 MHz.

Measurements were taken of the untuned insertion losses of the devices used as a delay line. In addition, the peak output for the convolution of two 2.7  $\mu\text{sec}$  rectangular pulses was measured. The output was terminated by the  $50\Omega$  impedance of the input stage of the output detector circuit. At the time these tests were made, the circuit model for the device had not been developed, therefore three measurements were made at the same frequency of 50 MHz. Indications were that the longer coupling region on the lithium niobate favors the measurements on the  $\text{Bi}_{12}\text{GeO}_{20}$ : The output power is given by

$$P_{\text{out}} = K P_{\text{in}}^2 K^1$$

where  $P_{\text{in}}$  is the input power level and  $K^1$  is the insertion loss of the device as a delay line.  $K$  is a constant, depending upon the material

properties and the geometrical construction. The experiment was designed to give a nearly equivalent geometrical factor; therefore,

$$K = \frac{P_o}{K^2 P_{in}^2}$$

is a measure of the nonlinear efficiency of the material. The results of these measurements are summarized in Table I. On the basis of these measurements, it was decided that further effort in the program should be concentrated on Y-Z lithium niobate. The conversion efficiency was somewhat better than the best case in  $\text{Bi}_{12}\text{GeO}_{20}$ . Lithium niobate has other advantages. First, the surface wave propagation velocity is 3480 m/sec compared to about 1710 m/sec for  $\langle 111 \rangle$  cut, (110) propagating  $\text{Bi}_{12}\text{GeO}_{20}$ , or 1690 m/sec for  $\langle 100 \rangle$  cut (110) propagating  $\text{Bi}_{12}\text{GeO}_{20}$ . As a consequence, higher frequency and larger bandwidth transducers can be fabricated on the niobate. Second, the surface coupling constant as determined by  $\Delta V/V$  is 0.78 percent and 0.70 percent for the two  $\text{Bi}_{12}\text{GeO}_{20}$  cases and is 2.2 percent for lithium niobate. That is, the surface wave conversion efficiencies are greater for lithium niobate, so the insertion efficiencies for the transducers will be greater on this material. Lithium niobate shows a large anisotropy in the propagation velocity near the Y-Z direction, in such a way as to greatly minimize acoustic beam spreading along the Z direction. This can minimize losses due to diffraction of the acoustic energy and of the interaction region between the two transducers.

An alternate approach to the determination of the nonlinear coupling is to obtain a direct measurement of the nonlinearity by applying a dc field to the piezoelectric material and measuring the change of velocity of the propagating acoustic surface wave. Such measurements have been reported to characterize the nonlinearity in volume acoustic waves. This concept was tested using a convolution filter constructed on Y-Z lithium niobate and on  $\langle 111 \rangle$  cut (110) propagating bismuth germanium oxide. The test frequency was 100 MHz on the  $\text{LiNbO}_3$  and 50 MHz on the  $\text{Bi}_{12}\text{GeO}_{20}$ . Twenty-finger-pair periodic

TABLE I

## Nonlinear Efficiency Measurements Summary

Material	Frequency, MHz	Available Input Power per Channel, dbm	Line Insertion Loss, dB	Peak Output Power, dbm	K, Corrected Conversion Loss Factor, dB
LiNbO <sub>3</sub> (Y-Z)	50	+9	11	-79	-86
Bi <sub>12</sub> GeO <sub>20</sub> <111> cut (110) prop	50	+9	23	-94	-89
Bi <sub>12</sub> GeO <sub>20</sub> <100> cut (110) prop	50	+9	25	-105	-98
LiNbO <sub>3</sub> (Y-Z)	102	+22	14	-54.5	-89.5

T645

input transducers were used. An evaporated aluminum plate coupling structure in the center of the LiNbO<sub>3</sub> and a chromium plate coupling structure were applied to the two devices. The experiment was to measure the phase shift through the delay line as a voltage was applied to the plate. From the change in phase, the change in acoustic velocity under the plate can be determined.

The results obtained on this lithium niobate sample are shown in Table II.

The effects of the field on the velocity were not very great, but the procedure works well on lithium niobate and a detectable change in the velocity can be observed.

**TABLE II**  
**Field Dependent Phase Shift**

Applied Field, V/cm	Observed Phase Shift Over 4.5 $\mu$ sec Delay, deg	Relative Change in Velocity, $\Delta V/V$
$1.33 \times 10^3$	0.05	$0.3 \times 10^{-6}$
$2.57 \times 10^3$	0.09	$0.55 \times 10^{-6}$
$5.33 \times 10^3$	0.18	$1.1 \times 10^{-6}$
$6.67 \times 10^3$	0.25	$1.5 \times 10^{-6}$

T646

The procedure did not work on  $\text{Bi}_{12}\text{GeO}_{20}$ , not because there is no observable velocity change but because a much larger change in velocity occurs due to another effect. Namely, the  $\text{Bi}_{12}\text{GeO}_{20}$  is semi-conducting. Biasing the plate positive decreases the surface wave velocity; biasing the plate negative increases the velocity. The effect is not symmetrical, however, and it shows a large time constant (~second) upon application of the voltage. Moreover the material is photoconductive. Light causes a change in the resistance of the sample and changes the surface wave velocity also. Although these are very interesting effects, they precluded a direct measurement of the nonlinear coupling strength in this material.

### 3.2 TRANSDUCER DESIGN

As is shown in the subsequent section on the design theory of the nonlinear convolution filter, the nonlinear interaction that leads to the convolution function has no inherent frequency dependence of its own. The consequence is that, except for electrical tuning effects associated with the nearly capacitive output impedance of the device, the frequency dependence of the insertion loss replicates the frequency response of the input interdigital transducers of the device. Therefore,

tailoring the frequency response of the device reduces to an exercise in tailoring the frequency response of these transducers. The major effort in this regard involved the utilization of broadband input transducers of linear FM design employing aperture weighting of the transducers to control the frequency response.

Interdigital (ID) transducers with periodic electrode spacing have been widely used for the efficient generation and detection of acoustic surface waves on piezoelectric materials. The periodic ID transducer is commonly composed of only a small number of electrodes and utilizes an electrical matching network tuned to the synchronous frequency. In this manner highly efficient transduction is obtained within a limited bandwidth about the synchronous frequency. The bandwidth of a matched transducer is determined by the strength of the piezoelectric coupling in the delay medium and is generally limited to less than 25 percent.

In some earlier work, Hughes has pioneered the development of ultra-broadband surface wave transducers. It was found that transducers composed of multiple electrodes in a nonperiodic ID array are capable of bandwidths of an octave or more. When properly designed, these arrays can be driven without an additional electrical network yielding flat passbands with steep skirts.

A nondispersive delay line employs two identical nonperiodic arrays configured as shown in Fig. 7. Acoustic excitation occurs under the electrodes whose spacing corresponds to the wavelength of the acoustic surface wave at the driving frequency. The position of excitation, therefore, varies with frequency, but for the configuration shown in Fig. 7, the time delay between the input electrodes and corresponding output electrodes is constant with frequency. Hence, the delay line is nondispersive and the bandwidth is determined by the range of electrode spacing in each transducer array. The shape of the passband is determined by the amplitude weighting of the electrodes as a function of frequency and can, therefore, be controlled with a great deal of flexibility. The efficiency of the nonperiodic transducer is proportional to the piezoelectric coupling constant of the substrate. In strong

coupling materials significant improvements in bandwidth over tuned periodic transducers are achieved by sacrificing less than 10 dB in midband transducer loss.

Figure 8 shows the predicted and measured insertion loss versus frequency for an early 40 percent bandwidth design employing 210 electrodes in each array with no amplitude weighting. The 3 dB difference in loss between the two curves is attributed to propagation loss in the 10  $\mu$ sec nondispersive LiNbO<sub>3</sub> delay line. This delay line shows that nonperiodic transducers can indeed operate over bandwidths corresponding to the range of electrode spacing. However, in Fig. 8 the passband is tapered, and there are large inband ripples.

Hughes has shown directly from the circuit model analysis that the passband taper in linear FM transducers can be eliminated by transducer aperture tapering (apodization).<sup>7</sup> It is found that the aperture of the n-th electrode should be

$$W_n = (W_o f_n/f_o)^{-3} (1 + Q_L^2 f_n^2/f_o^2)$$

where  $W_o$  is a constant,  $Q_L$  is the load Q,  $f_o$  is the center frequency, and  $f_n$  is the synchronous frequency of the n-th electrode.

Passband ripple in a broadband surface wave transducer is best discussed with regard to the physical mechanism causing the ripple. The three most important causes are summarized briefly in the following.

- **Fresnel Ripple** – Fresnel ripple results from end effects in the array. In most cases it can be thought of as a mathematical consequence of the finite length of the array without regard to the particular positioning of the electrodes within the array. Fresnel ripple can be reduced by lengthening the array or by weighting the electrodes to suppress the end effects. By appropriately weighting (apodizing) the overlap distance of

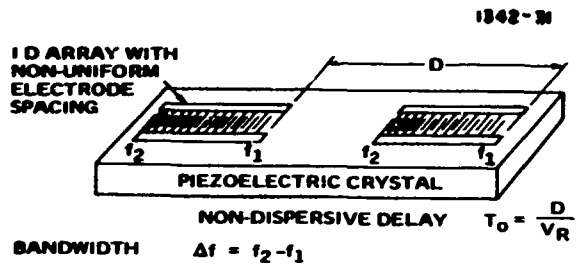


Fig. 7. Broadband Surface Wave Delay Line.

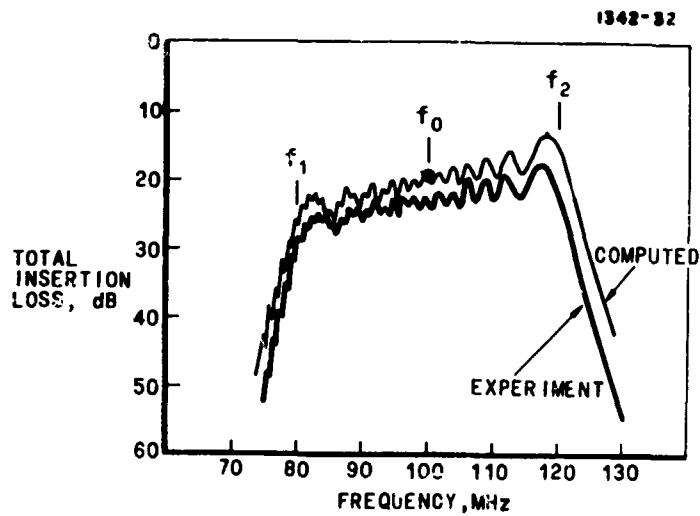


Fig. 8. Computed and Measured Insertion Loss for 40% Bandwidth (210 Electrodes).

the electrodes that are near the end of the pattern, the surface wave excitation can be brought smoothly and gradually to zero at the edges of the passband. The sharp discontinuity in excitation which produces the Fresnel ripple is thereby eliminated. This weighting approach reduces the ripple without requiring excessive array length and, therefore, has many practical advantages. The weighting does, however, reduce the effective bandwidths by rounding the passband skirts.

- Double or Triple Transit Ripple – Double or triple transit ripple results from the interference of the main and multiple transit signals at the receiver taps. The frequency and amplitude of this ripple are determined by the path length to the reflecting transducer and the magnitude of the reflected wave. For typical broadband transducer designs, the level of multiple reflections is small. This type of ripple does however not appear in the response of the convolver when the frequency response is determined from the output pulse amplitude of two correlated pulse envelopes of the carrier frequency. This is a result of the fact that the correlation occurs on the first pass of the pulse under the convolution region of the device. Double transit echos, however, manifest themselves in the appearance of a spurious delayed convolution signal. This signal occurs when both the input signals are reflected from the transducers and pass under the convolution region again.
- Ripple from Acoustic Impedance Discontinuities of Electrodes – Transducers that are properly apodized to remove Fresnel ripple still exhibit a residual ripple due to end effects, because there is a discontinuous

change from periodic, surface loading electrodes to bare substrate at the end of the transducer. These ripples can be reduced by tapering the widths of the electrodes smoothly to zero at the ends of the transducers.

Figure 9 shows the computed and measured response of a non-dispersive delay line operating over an octave bandwidth, in which the transducers were apodized as described to remove passband taper and suppress Fresnel ripple. The ripple compensation described was not incorporated in this design. The measured response contains a 2 dB droop across the octave bandwidth corresponding to acoustic propagation loss in the 11  $\mu$ sec line. As shown later in this report, the transducers can easily be designed with slightly modified apodization to compensate for this droop. With the linear propagation loss subtracted, the delay line demonstrates a 3 dB bandwidth of 62 percent, and a 35 percent delay line bandwidth having only  $\pm 0.5$  dB ripple. Specific transducer designs show that linear FM transducers can be designed with ripple levels less than  $\pm 0.1$  dB.

If a nonlinear device is to be constructed using a coarse grating coupler, a special problem arises if aperiodic input transducers are used. This stems from the fact that two transducers need to be used, centered at frequencies which are displaced, because the difference in frequency  $\Delta f$  of the two input transducers must correspond to the periodicity of the coarse grating. If there is to be no phase distortion at the output, this means that an input of one transducer at frequency  $f_a$  must meet a signal from the other transducer at a frequency  $f_a + \Delta f$ , at a constant time delay. What is required is that the distance between the point where  $f_a$  originates in one transducer to the point where  $f_a + \Delta f$  originates in the other transducer must be constant. For a linear FM formula for the electrode spacing, this requirement is automatically met, provided both transducers are derived from the same spacing formula. A complication arises, however, in determining the required aperture weighting. It is also desired that the aperture at  $f_a$  on one transducer equals the aperture of  $f_a + \Delta f$  on the second

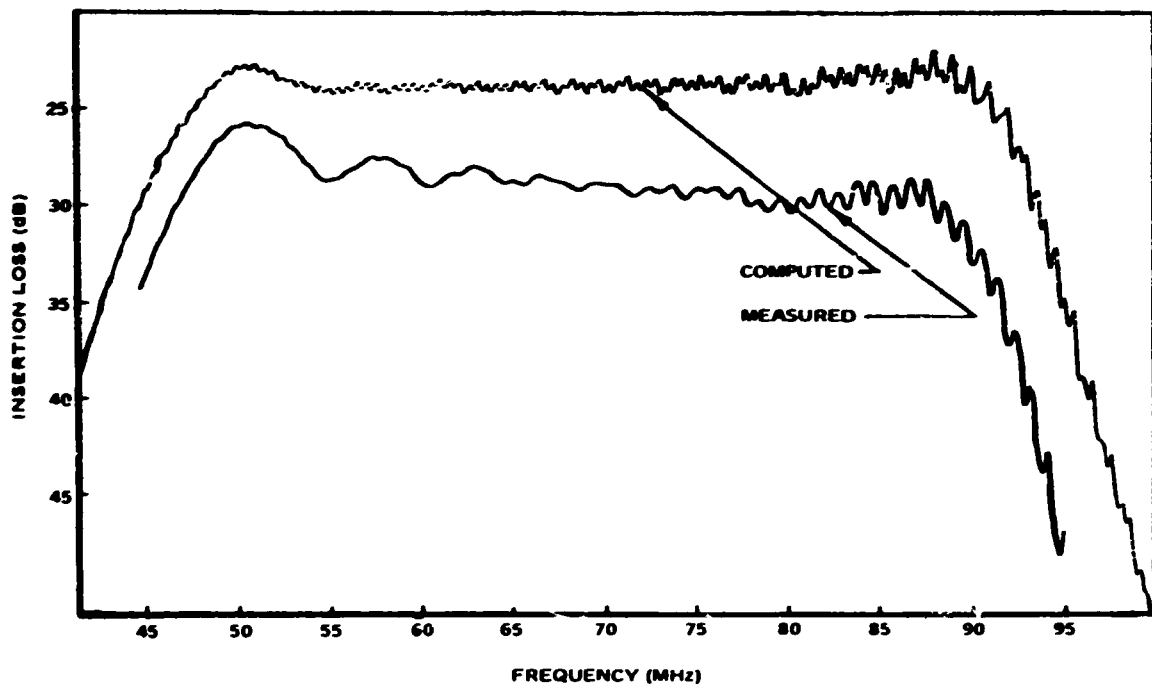


Fig. 9. Comparison of Computed and Measured Insertion Loss for an Octave-Bandwidth Nondispersive Delay Line.

transducer. For this reason, the same aperture weighting formula must be used on both transducers. To maintain uniform response, a weighting formula intermediate between those which would be derived for either transducer must be used.

In case the device is to be used as a variable time delay, input and output aperiodic transducers with long time delays are particularly appropriate. It will be shown that the convolution efficiency varies as the square of the input pulse length. In the case of variable time delay, one wishes to use a very short pulse in one input channel. As a consequence, the input pulse is normally very short. A way to overcome this difficulty is to use very long input transducers.

The design of Fig. 9 was used in many of the investigations under the present program, except that the dimensions of the transducers were reduced by a factor of two to extend the frequency response over the range of 95 to 180 MHz.

Figure 10 shows the insertion loss of this design (in this case measured point by point, which does not reveal some of the ripple detail). The results again agree with the theory with the exception of some dropoff of about 2 dB/octave in the frequency response. This line had a delay between transducers of 9  $\mu$ sec. The 2 dB dropoff was considered acceptable, and the same design was extended to the case where the transducers were 7.1 cm apart, corresponding to a line delay of 21  $\mu$ sec. Figure 11 shows the insertion loss of this delay line construction. As can be seen, the line now shows an average frequency dependent slope of about 5 dB/octave. The clear conclusion of these results is that the magnitude of the frequency dependent slope is a function of the delay between transducers.

The 5 dB slope was considered serious enough to necessitate redesign of the transducer to remove this slope; this redesign was completed.

The detailed formulas used for the design of the aperture weighted transducers are given here:

CONVOLUTION RESPONSE ANGLED BACK DEVICE

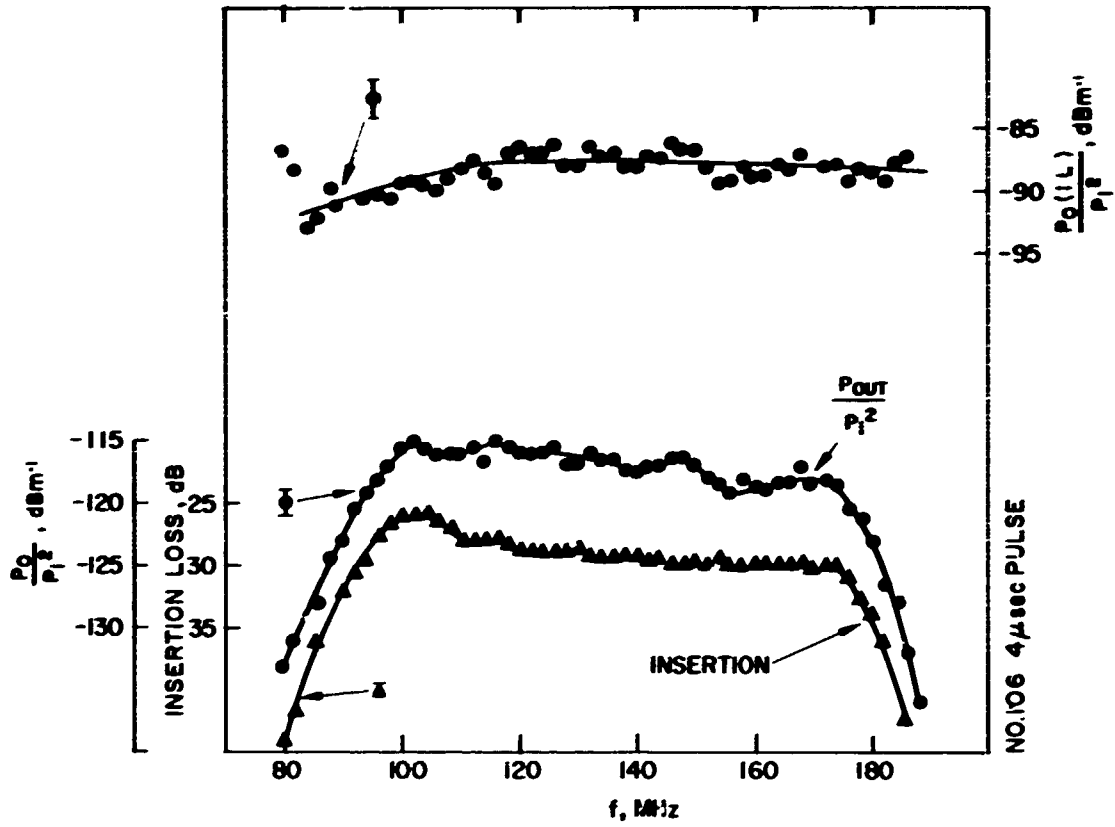


Fig. 10. Measured Performance of 95 to 180 MHz Broadband Convolver.

$$W_{ro} = W_o \left\{ \begin{array}{l} \left[ \frac{1 + \frac{f_n^2}{f_o^2}}{2 \left( \frac{f_n}{f_o} \right)^3} \right] \cos^2 \frac{5\pi}{2} \left( \frac{f_n}{f_{min}} \right) \quad f_{min} \leq f_n < 1.2 f_{min} \\ \left[ \frac{1 + \frac{f_n^2}{f_o^2}}{2 \left( \frac{f_n}{f_o} \right)^3} \right] \quad 1.2 f_{min} \leq f_n \leq \frac{8}{9} f_{max} \\ \left[ \frac{1 + \left| \frac{f_n}{f_o} \right|^2}{2 \left| \frac{f_n}{f_o} \right|^3} \right] \cos^2 \frac{9\pi}{2} \left( \frac{f_n}{f_{max}} \right) \quad \frac{8}{9} f_{max} < f_n \leq f_{max} \end{array} \right.$$

The  $\cos^2$  weighting at the end of the array is applied to reduce the Fresnel ripple caused by termination of the array. In this equation,  $w_n$  = aperture of the fingers corresponding to frequency + n and  $w_o = 1.155$  mm. This choice of  $w_o$  gives its array a capacitive reactance of  $50\Omega$  at the center frequency of 140 MHz:

$$f_{min} = 80 \text{ MHz}$$

$$f_{max} = 200 \text{ MHz}$$

Since the array has a linear FM dispersion characteristic, the frequency corresponding to a given position of the array is given by:

$$f_n = 200 \left[ 1 - \frac{X_n \cdot 0.6}{47.283} \right]$$

The array length in the given design is 47.283 mils.

Now the acoustic power into the array at a given frequency is proportional to the square of the acoustic aperture for this design,

because the equivalent parallel radiation resistance is inversely proportional to the aperture. In order to introduce an additional frequency dependence in the design, the new aperture should be given by

$$W_n = W_{no} 10 K \frac{f_n}{f_{max}} \cdot C$$

C is a scale constant that determines the place at which the apertures match, and K is determined by the additional frequency slope required. For a ratio of

$$\frac{W_n^2 (90)}{W_n^2 (180)^2} \cdot \frac{W_{no}^2 (180)}{W_{no}^2 (90)} = 10^{-0.5}$$

corresponding to a 5 dB/octave correction. For  $f_{max} = 200$  MHz, one finds

$$10^2 K \left( \frac{90}{200} - \frac{180}{200} \right) = 10^{-0.5} \text{ or } K = 0.555$$

The revised aperture at a given finger position  $X_n$  is then given by

$$W_n = W_{no} 10^{0.555} \left[ 1 - \frac{0.6 X_n}{47.283} \right] \cdot 200 \cdot C$$

For the apertures to match at the low frequency end of the array, C is such that:

$$W_n = W_{no} 10^{-0.333} \frac{X_n}{47.283}$$

Using this relation, corrected values of aperture can be calculated. Since the procedure results everywhere in a reduction of aperture and thus of the capacitance, the final result must be scaled up to return to a capacitive reactance of  $50\Omega$ . The final correction formula was:

$$W_n = 1.3 W_{no} 10^{-0.333 \frac{X_n}{47.283}}$$

The experimental results obtained for the insertion loss of the modified design are shown in Fig. 12. The procedure has worked very effectively to give an average flat band response within about  $\pm 1/2$  dB. The character of the ripples was in good agreement with the original theoretical predictions. This then is the transducer design that was ultimately used in the program to construct the delivered broadband convolution filter.

As will be noted in the design theory section of this report, an aperture weighted broadband transducer proved not to be the optimum configuration. The reason for this is that the convolution structure, whether plate or coarse grating, needs to be wide enough to accommodate the maximum aperture; while for best conversion efficiency, it is desirable to minimize the device width. For this reason, some preliminary work was done on design of a transducer using a general aperiodic design, not linear FM. This procedure, which was developed by Hughes, enables one to design broadband transducers that have a constant aperture. No time was available for incorporation of this design in the delivered item. Under the present program the procedure was applied to the design of broadband transducers which would be suitable for the convolution filter. Under some subsequent work at Hughes, delay lines incorporating one of the designs were constructed and tested. The results confirmed the theoretical prediction. This work is described in the Appendix.

Two convolution filters were also delivered during the program in which the input and output transducers were a periodic 5-finger-pair design centered at 146 MHz and a 7-finger design centered at 195 MHz. In the case where moderate bandwidths of 20% or less are required, these designs are appropriate.

Reproduced from  
best available copy.

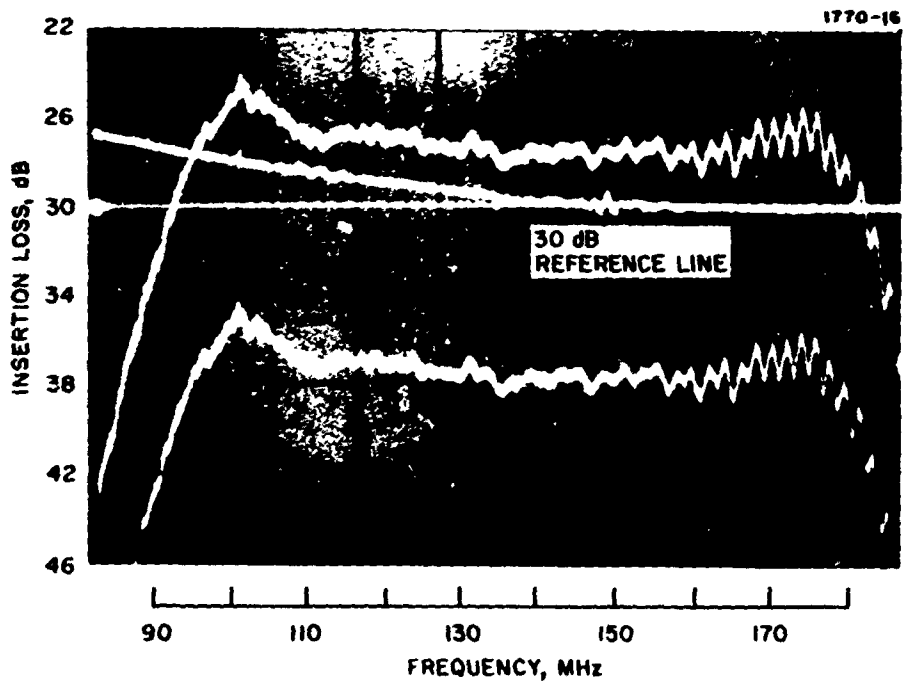
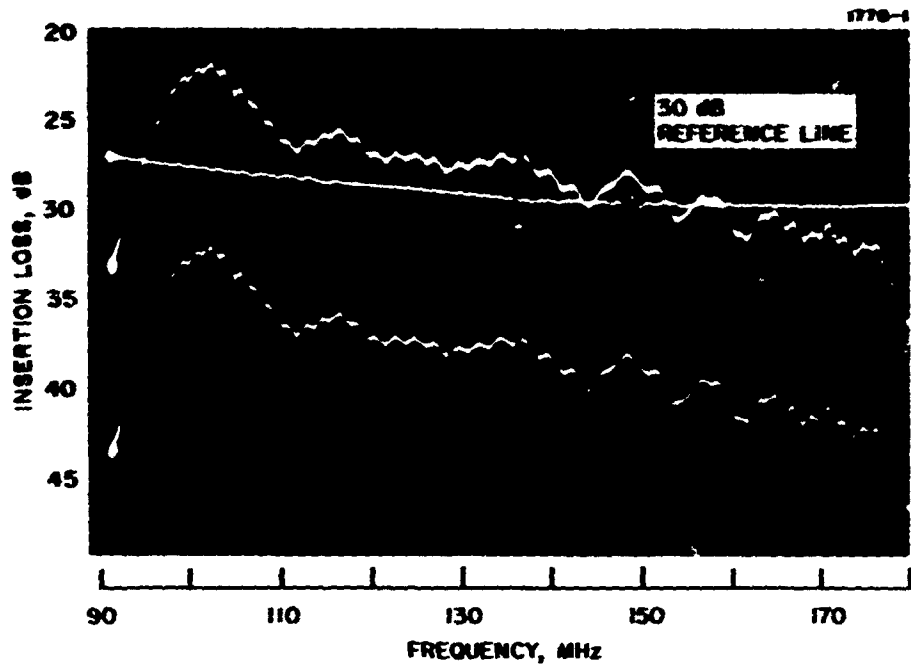


Fig. 12. Delay Line Insertion Loss: Modified Broadband Design.

### 3.3 ELIMINATION OF SPURIOUS SIGNALS

In addition to the derived convolution or correlation signal, the input surface waves in these devices can generate both spurious surface wave and bulk wave signals. The generation or detection of these signals can be suppressed by the geometrical configuration of the device.

Using a plate coupled structure, spurious signals associated with nonlinear surface wave effects and with bulk wave generation are observed. Figure 13 shows a simple narrow band device on Y-Z lithium niobate with a rectangular coupling plate and 20-finger-pair periodic input transducers. Figure 14 shows the output at the coupling plate when two rectangular pulses at a carrier frequency of 102 MHz are simultaneously fed to the two inputs. One should observe only the central triangular pulse, but additional spurious signals are evident. The other two signals are associated with rf pickup. These can be eliminated by shielding the three parts and by using electrical filters on the input to further reduce rf input. A low pass filter is used on the input circuits with a cutoff frequency of about 110 MHz. This decreases the second harmonic content of the input signal which can feed through to the output plate. A high pass filter is used on the output circuit, which cuts off frequencies below 200 MHz and rejects any fundamental signals and effectively removes the rf input, as shown in Fig. 15, but some spurious signals remain. In this device, the last smaller signal to appear is a bulk wave signal which is generated at the input transducer. It appears in this device because the back surface was not well damped acoustically. The magnitude of this signal can be affected by changing the termination at the rear surface; it is not present in other devices mounted with black wax. The (b) and (c) portion of Fig. 15 shows the output with only one input or the other. The convolution signal disappears, but the spurious signals remain. The remaining spurious signals correspond in time to the arrival of the acoustic surface wave at the leading and trailing edges of the convolution plates. These signals correspond to a traveling second

M 7949

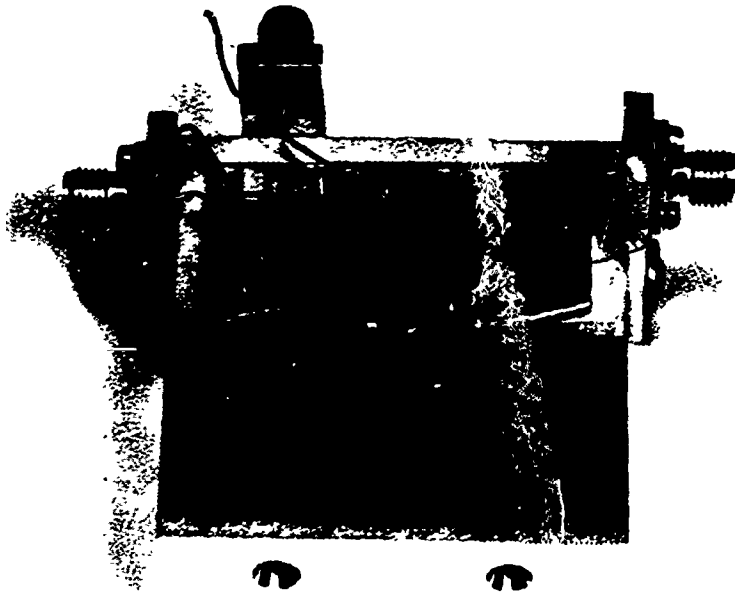
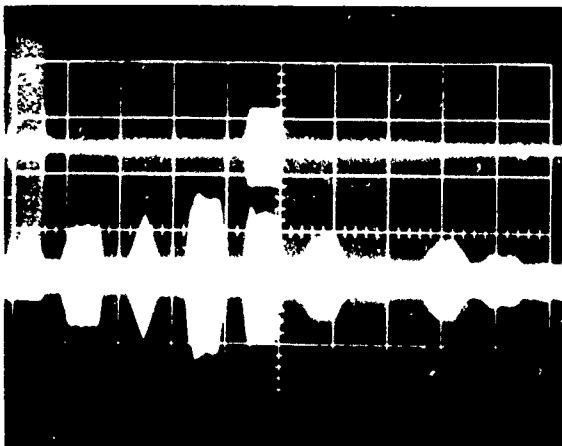


Fig. 13. Rectangular Plate Coupler with Periodic Input Transducers on Y-Cut Z-Propagating Lithium Niobate.

Reproduced from  
best available copy.



INPUT

Rectangular Coupl-  
ing Plate: Leading  
to Large Spurious  
Output

OUTPUT

Fig. 14. Surface Wave Convolution Filter Showing Spurious Signals.

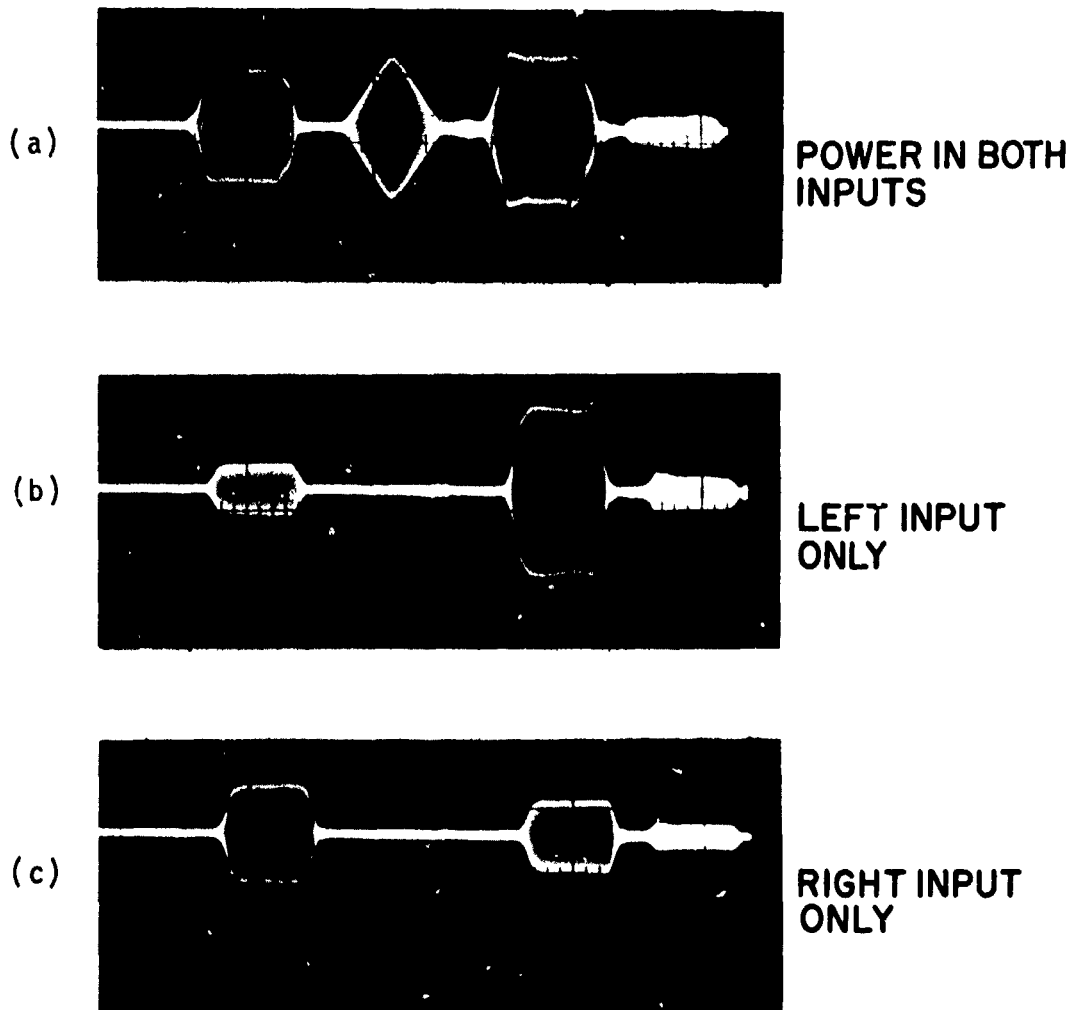


Fig. 15. Details of Spurious Signal with Rectangular Coupling Plate.

harmonic signal and cannot be eliminated by filtering the input, because they are due to the generation of the second harmonic by the fundamental, as shown in the work of Lean. The edge of the convolver plate acts as a single element pickup for this traveling second harmonic wave. It was hypothesized that if this were the case, it should be possible that suppression of this signal would occur if the edge of the pickup plate were angled, as shown in Fig. 16. This would then average the charge carried by the traveling second harmonic over a number of wavelengths, as shown schematically in Fig. 17.

The results obtained for the narrow band, angled plate, end device are shown in Fig. 18, where the spurious signals have now been effectively reduced by the modified construction. In addition, the latter of the two spurious signals is also suppressed if the presence of the convolution plate introduces significant dispersion into the propagation velocity underneath the coupling plate. This will occur if the plate is made of gold, which introduces a high dispersion, rather than the aluminum used in our case, which introduces only a small amount of dispersion.

Figure 19 shows schematically the broadband convolution filter we constructed. This device uses the original aperture weighted linear FM transducer design for the input and output transducers.

The high frequency end of the transducers are both at the right side of the pattern. The transducer design had a total number of 97 fingers and was designed for a nominal bandwidth of 70 percent. The design was scaled and tested at two center frequencies, 70 and 140 MHz; the figure shows the dimensions for the 140 MHz device.

Detailed measurements of the frequency response at the output terminal are considered later. It is noted here that a rapidly varying frequency dependent output was observed which was not predicted from the response of the input transducers. The normalized response over a small frequency interval is shown in the upper curve of Fig. 20. The maxima and minima in the response correspond to severe convolution pulse distortion for small changes in input frequency. Figure 21(a) shows a nearly triangular output at 98.1 MHz and the badly distorted

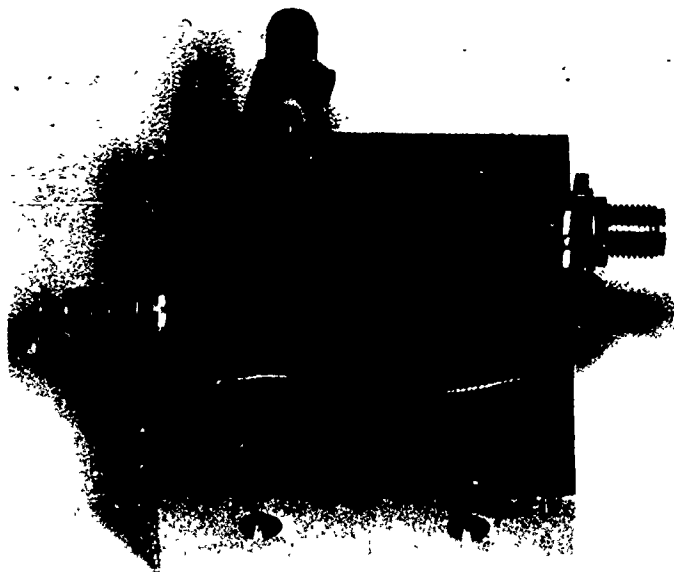
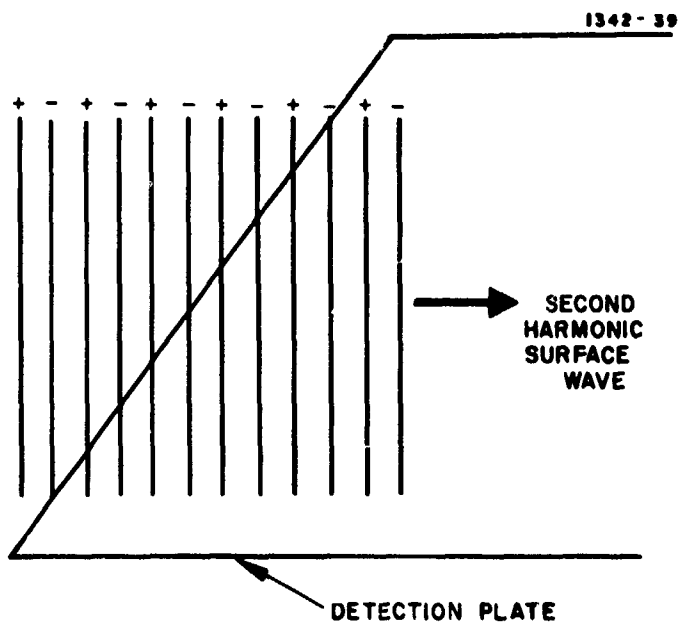


Fig. 16.  
Paralleloiped  
Coupling Plate.

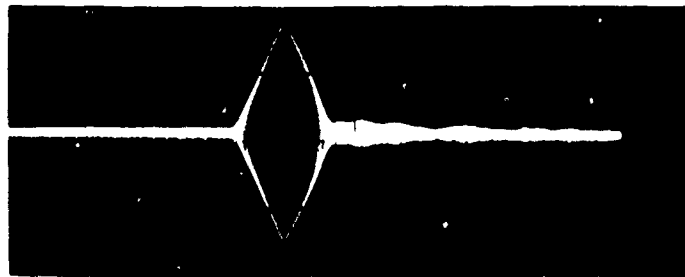
Fig. 17.  
Averaging Effect  
of Angled Ends of  
Paralleloiped.



1315-17

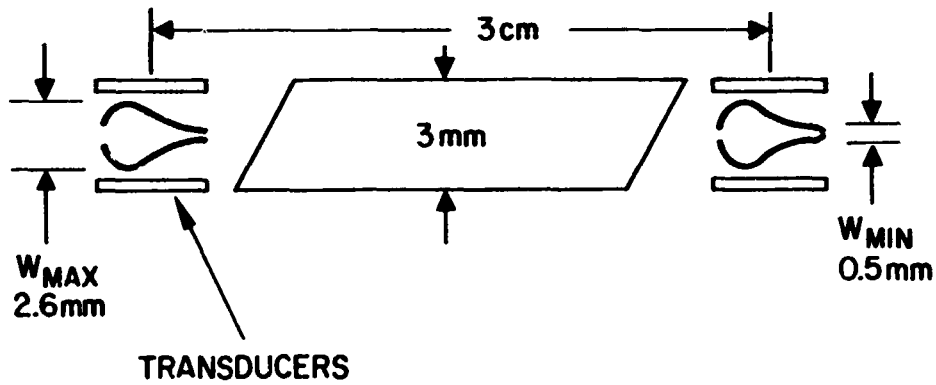


RECTANGULAR PLATE



PARALLELOIPIPED PLATE

Fig. 18. Results with Paralleloiped Plate.



### Transducers

97 Fingers

Linear FM, Aperture weighted design.

45 - 90 MHz, nominal

or 90 - 180 MHz, nominal (Dimensions, shown)

Fig. 19. Broadband Convolution Filter Schematic.

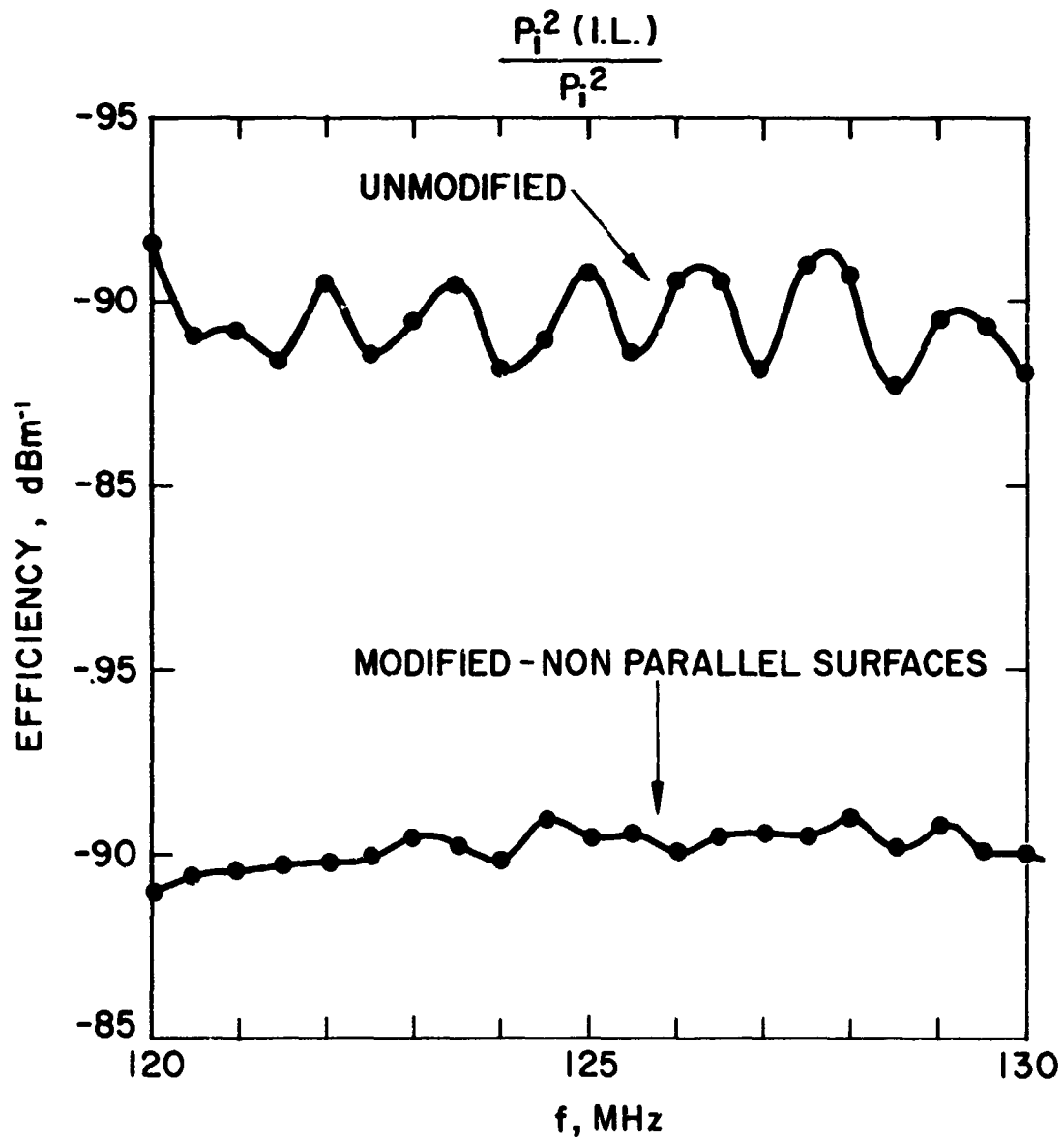
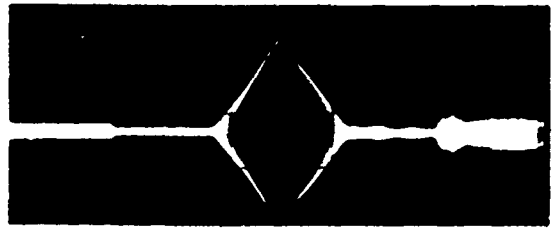
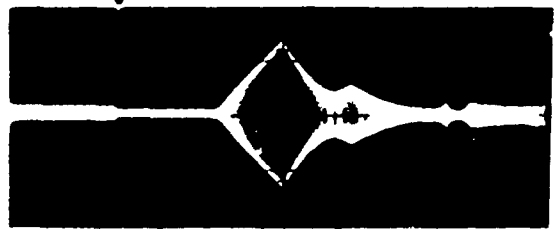


Fig. 20. Pulse Distortion in Broadband Convolution Filter.

Reproduced from  
best available copy. ©



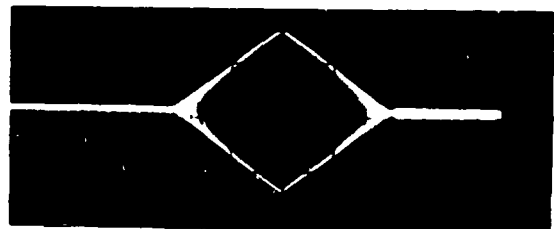
(a) 98.1 MHz



(b) 98.6 MHz



(c)



(d)

Fig. 21. Bulk Wave Generation Effect.

pulse at 98.6 MHz. As the input pulse is made much shorter, a series of successive output pulses is observed in Fig. 21(c). In this case all of the signal disappears if either of the two inputs is removed. We concluded that the extra signal was due to the generation of a bulk wave by the nonlinear interaction of the two surface waves. The extra signal is detected as the dipole layer associated with this bulk wave is annihilated as it strikes the bottom surfaces, or as it is progressively annihilated in successive reflection from the top and bottom surfaces.

This is shown schematically in Fig. 22. A piezoelectrically active shear wave with a velocity of 4425 m/sec and a piezoelectrically active longitudinal wave with a velocity of 6803 m/sec can propagate along the Y-axis of the lithium niobate. The sample thickness in this case was 2.1 mm, corresponding to a time delay of about 0.32  $\mu$ sec across the crystal. The observed time delay corresponds approximately to the bulk longitudinal wave. The solution to this bulk mode problem was in fact indicated by Svaasand in his early report. It requires cutting the back of the crystal at an angle with respect to the front surface, as indicated in Fig. 23. We have used a relatively shallow angle of about  $4^\circ$ . This construction averages the unwanted wave over several wavelengths. This construction minimizes the pulse distortion and also serves to remove the oscillation from the frequency response of the device. The result is illustrated in Fig. 21(a), which shows the output for a corrected angle bulk construction, and in Fig. 20, where the lower wave shows the frequency response of the corrected device. The response is now nearly smooth. The measurements extend over only part of the passband but clearly show the oscillatory behavior of the uncorrected device and the improvement obtained by the angled construction.

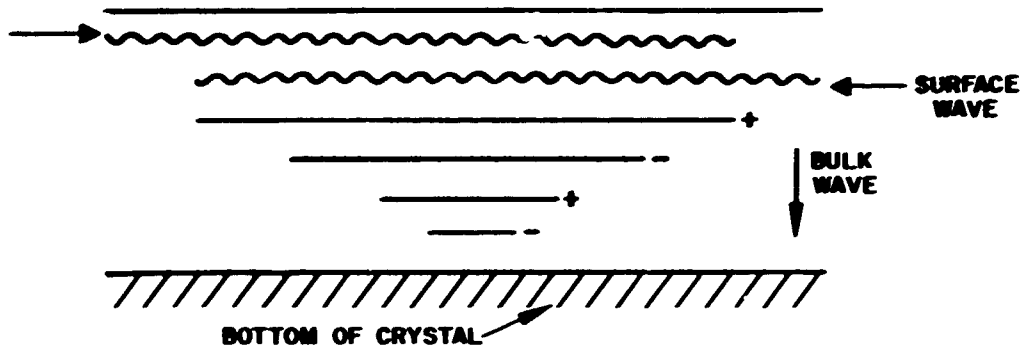


Fig. 22. Suppression of Bulk Wave Interference.

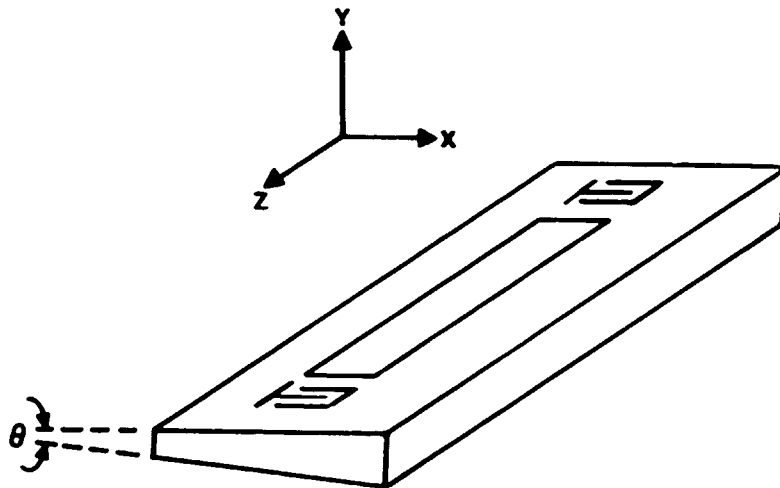


Fig. 23. Bulk Wave Suppression.

### 3.4 DESIGN PARAMETERS

A broadband convolution filter utilizing the original nominal octave bandwidth design (prior to correction for frequency slope) was constructed, and the conversion efficiency as a function of frequency was measured. The results of these measurements led to a design theory that relates the convolution efficiency to the input transducer design, the geometrical design of the plate coupler, and a nonlinear material constant, which can be obtained from the results.

The characteristics of the broadband convolver shown previously in Fig. 19 can be related to a simple design theory which relates the input transducer, coupling structure geometry, electrical termination, and material nonlinearity to the performance of the device. It is expected that the design criteria can be extended in a straightforward manner to the case of a coarse grating coupling structure.

Using the dimensional notation of Fig. 24, the equivalent circuit can be represented approximately as shown in Fig. 25. The circuit is approximate, in that the driving voltage generated by the nonlinear interaction is assumed to have a strictly capacitive internal impedance. Any real part of this internal resistance that would reflect energy dissipation has been neglected. In the equivalent circuit, the entire convolution plate is considered to be a capacitor with area  $W_p L_p$  and a total capacitance  $W_p L_p \epsilon / S$ . That part of the plate containing the interacting signals has an area  $W_a L_a$ , where  $W_a$  is the acoustic aperture of the input transducer and  $L_a$  is determined by the duration of the convolved signals. The internal dipole generated by the nonlinear interaction produces a source voltage of magnitude  $e_g = Q_o \frac{\Delta}{t}$ .

The polarization per unit volume  $Q_o$  is produced by the nonlinear interaction and is proportional to the product of the strains induced by the two surface wave.  $\Delta$  is some mean penetration of the interaction which is of the order of the acoustic wavelength. The input acoustic power from the input sources is  $K_1 P_1$  and  $K_2 P_2$ , where  $P_1$  and  $P_2$  are the available power at the two input ports, and  $K_1$  and  $K_2$

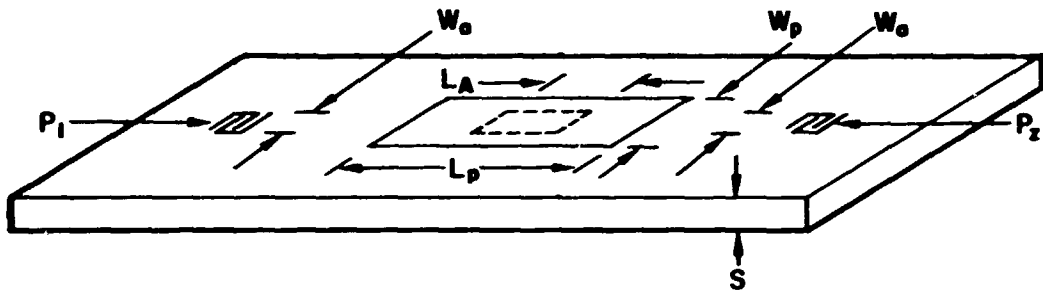
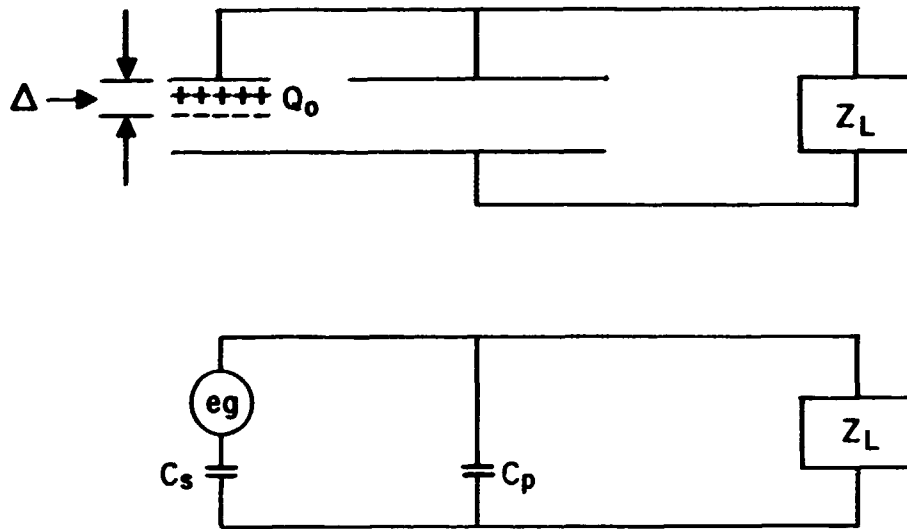


Fig. 24. Convolver Configuration -- Geometrical Symbols.



Where

$$e_g = Q_0 \frac{\Delta}{t} \cdot e^{2j\omega t}$$

and

$$C_s = \frac{w_a L_a t}{s}$$

$w_a$  = acoustic aperture

$$C_p = \frac{(W_p L_p - w_a L_a) t}{s}$$

$L_a$  = interaction length

$W_p$  = plate width

$L_p$  = plate length

also use

$$C_T = \frac{W_p L_p \epsilon}{s}, \text{ total plate capacitance}$$

Fig. 25. Equivalent Circuit of Convolver.

are the conversion efficiencies of the transducers. It may be noted that  $K_1 K_2$  is thus the conversion efficiency of the input-output transducer pair, or  $1/K_1 K_2$  is the insertion loss of the input-output pair used as a delay line.

The number  $K$  has been introduced as a material parameter that is determined by the magnitude of the nonlinear interaction. Carrying out the algebra as in Fig. 26, the conclusions stated in Fig. 27 for the case in which the load on the output plate is purely resistive are reached. The conclusion is that for  $\omega > 1/R_C C_T$ , the output is independent of frequency. Either in this case or if the plate capacitance is tuned with an inductive load  $R_L + j\omega L$ , where  $L = 1/\omega^2 C$ , the maximum output is given by

$$P = K \frac{K_1 P_1 K_2 P_2 L_a^2}{W_P^2 L_P^2} \cdot \frac{1}{R_L}$$

This indicates that the output power may be increased by decreasing the load resistance. However, in the untuned case, the low frequency roll-off point is raised. In the case of a tuned load, the price is a decrease in the percentage bandwidth. The bandwidth  $\Delta f$  is given by  $\Delta f/f \sim \frac{1}{Q}$ , where  $Q$  determined by the output circuit is given by  $Q = 1/R\omega_0 C$  (series tuning) and  $\omega_0$  is the resonant frequency.

The second result is that the output is independent of the acoustic aperture. This is important in that the transducers used in the experiment were designed with an acoustic aperture that was dependent on frequency. Fortunately, this does not introduce an additional frequency dependent term in the convolution output.

The output of the broadband device of Fig. 19 was measured as a function of frequency, using untuned  $50\Omega$  input and output terminations. The input pulses were equal length, equal amplitude pulses of  $4 \mu\text{sec}$  duration. Available delay under the plate was  $7.5 \mu\text{sec}$ . The peak output power in the triangular convolved output signal and the insertion loss of the line were determined at each frequency. The results are displayed in Fig. 28. Three data curves are shown.

$$\text{Power out} = \frac{|e_g|^2 R_L \left(\frac{C_S}{C_T}\right)^2}{R_L^2 + \left(X_L - \frac{1}{\omega C_T}\right)^2}$$

Consider Resistive Load,  $X_L = 0$ . Then

$$\text{Power out} = \frac{|e_g|^2 R_L \left(\frac{C_S}{C_T}\right)^2}{R_L^2 + \frac{1}{\omega C_T^2}}$$

Find Frequency Response. Remember

$$e_g = Q_0 \frac{\Delta}{\epsilon} e^{2j\omega t}$$

But polarization per unit volume

$$Q_0 \sim S_1 S_2 \text{ (strain product)}$$

And Power input

$$P_1 \sim K_1 S_1^2 W_a V_{ac} \cdot \Delta$$

$$P_2 \sim K_2 S_2^2 W_a V_{ac} \cdot \Delta$$

where  $V_{ac}$  = acoustic velocity. But  $\Delta \sim 1/\omega$ . So

$$S_1 \sim \left( \frac{\omega P_1}{W_a V_{ac}} \right)^{1/2}$$

or

$$|e_g| = \frac{K \sqrt{P_1 P_2}}{W_a V_{ac}}$$

where  $K$  = effective nonlinear coefficient independent of frequency.

Fig. 26. Convolver Design Equations.

Power out then is given by

$$P_o = K \frac{K_1 K_2 P_1 P_2 L_a^2}{w_p^2 L_p^2} \frac{R_L}{R_L^2 + \frac{1}{\omega C_T}^2} .$$

Conclusions:

1. for  $\omega > 1/R_L C_T$ , output is independent of frequency.
2. output is independent of acoustic aperture.

Fig. 27. Results of Design Analysis.

## CONVOLUTION RESPONSE ANGLED BACK DEVICE

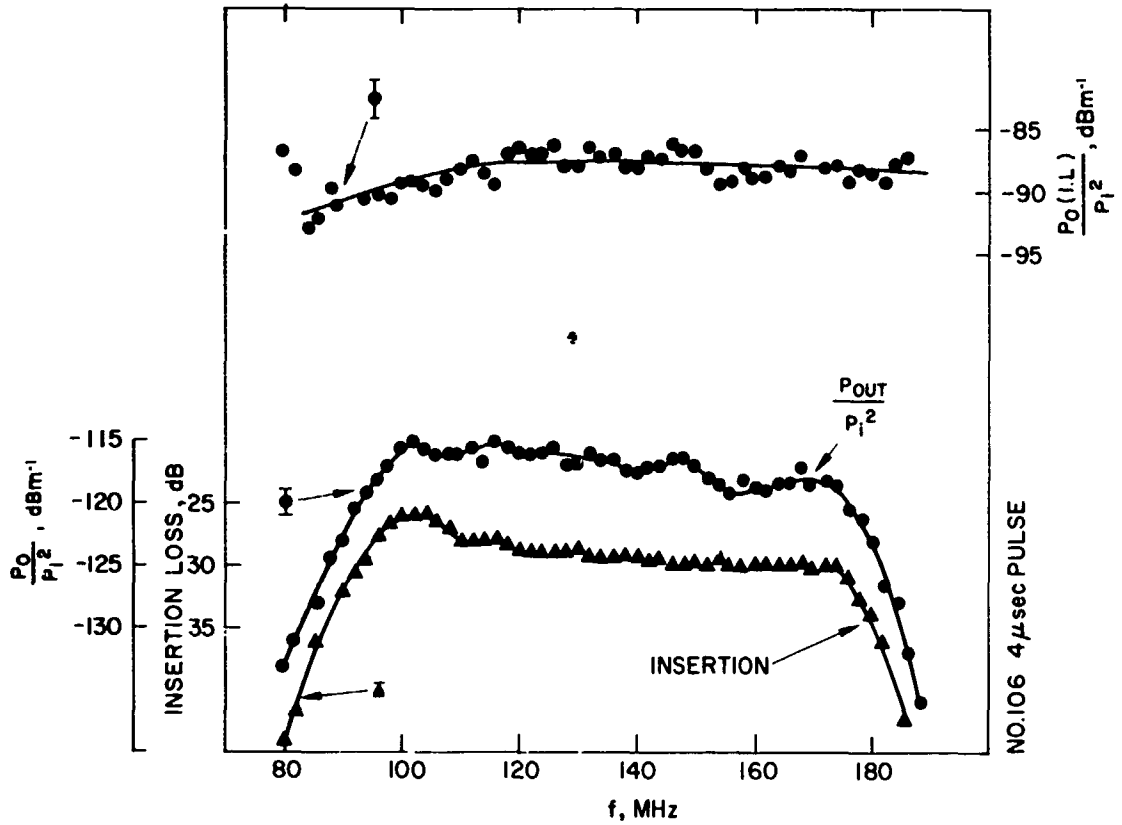


Fig. 28. Measured Performance of 95 to 180 MHz Broadband Convolver.

The bottom curve is the insertion loss at the line; the next curve above it is a plot of peak output power divided by the square of the input power  $P_o/P_i^2$ . This is a measure of the performance of the device. If conversion from the input to the nonlinear output introduces no frequency dependence of its own, this curve should replicate the insertion loss curve. Finally, we have defined a convolution efficiency term that is simply  $P_o/P_i^2$  multiplied by the insertion loss. This result should be a constant above a low frequency rolloff determined by the load resistance and the coupling plate capacitance. As can be seen, the convolution efficiency is substantially constant with an indication of a low frequency rolloff. The plate capacitance of this device was 26 pF, which would account for a 1.5 dB drop at a 180 MHz output, corresponding to a 90 MHz input.

Measurements of the convolution efficiency have also been made on a device with broadband input transducers scaled to operate in the 45 to 90 MHz range. The major difference was that the width of the convolution plate was 8 mm rather than 3 mm. According to the theory, the convolution efficiency (going as  $1/W_p^2$ ), should have been decreased by a ratio of  $(3/8)^2$  or 8.5 dB. The results shown in Fig. 29, while somewhat scattered (the input transducers had defects, and the angled back correction had not been incorporated), nevertheless indicate a conversion efficiency approximately 10 dB less than for the higher frequency device. It is emphasized that this difference is not a consequence of an explicit frequency dependence but only of the greater plate, width of the coupling structure. One may now determine the effective nonlinear coefficient for the material (Y and Z propagating lithium niobate) from these results.

$$K = \frac{P_o, (I. L.)}{P_i^2} \cdot \left[ \frac{L_p}{L_K} \right]^2 W_p^2 R_L$$

$$K = 10^{-5.7} \cdot \left[ \frac{7.5}{4} \right]^2 \cdot (0.3)^2 \cdot 0.50$$

CONVOLUTION OUTPUT - 70 MHz DEVICE  
 PLATE WIDTH = 8 mm.

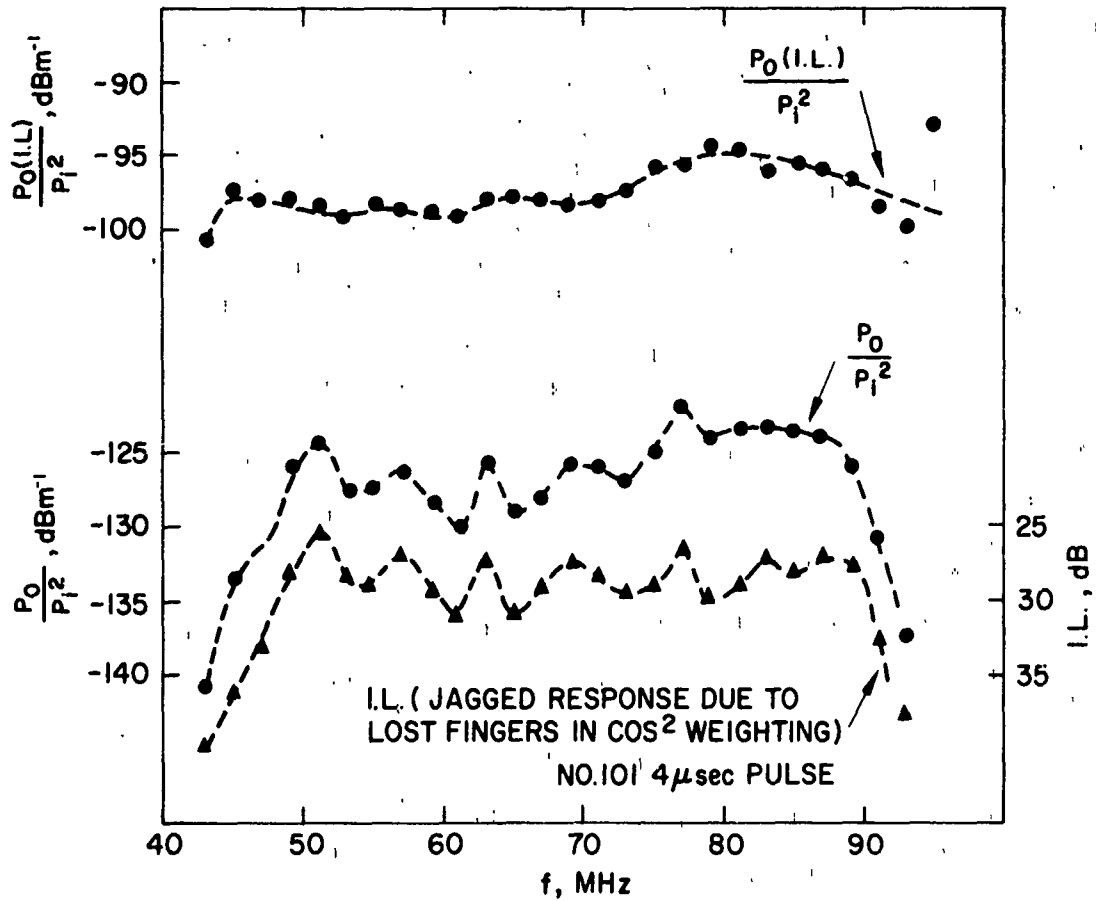


Fig. 10. Measured Performance of 45 to 90 MHz Broadband Convolver.

Thus:

$$K = 1.8 \times 10^{-5} V^2 / (W/cm)^2$$

Although the insertion loss in this class of nonlinear devices is of interest, it should be noted that the primary figure of merit is probably the maximum available power output. Because operation is in the nonlinear regime, the input acoustic power level cannot be arbitrarily increased. Lean 8 has shown that at an acoustic power level of 3W/cm at 100 MHz, the acoustic energy is rapidly transferred into higher harmonic propagating surface waves. This determines the maximum allowable input acoustic power level. This saturation level decreases approximately with increasing frequency as 1/f.

The calculations may be extended to the coarse grating coupler shown earlier in Fig. 2(b). All that is required is to use the input capacitance of the coarse grating structure rather than the plate capacitance, with the result that the output power is still given by

$$P_o = K \frac{K_1 K_2 P_1 P_2}{W_p^2} \left( \frac{L_a}{L_p} \right)^2 \frac{R_L}{R_L^2 + \left( X_L - \frac{1}{\omega C_T} \right)^2}$$

The advantage of this construction is simply that  $C_T$  may be much larger than with plate constructions where the plate thickness is limited by mechanical fabrication problems. For instance, in a coarse grating designed for a difference frequency of 30 MHz, the spacing between the center of the fingers is  $5 \times 10^{-3}$  cm. This means that for an untuned output it is very easy to keep the low frequency cutoff  $1/R_L C_T$  at a low value even for narrow widths, i.e., small  $W_p$ . Or alternatively in a reactively tuned case, the Q of a series tuned circuit  $1/R_L \omega C$  will be smaller; hence, a lower load resistance and higher power output is obtained for a given fractional bandwidth. The power output for a properly matched structure and for a given percentage bandwidth is expected to be proportional to the coupling structure capacitance.

Compared to the previously quoted results, which used a plate coupler on samples of thickness  $2 \times 10^{-1}$  cm, an improvement in convolution efficiency of about

$$\frac{2 \times 10^{-1}}{5 \times 10^{-3}} \cdot (1/4)$$

or 10 dB is anticipated for a 30 MHz coarse grating. The factor of (1/4) is a consequence of the reduced area of one electrode in the structure. This calculation neglects propagation losses introduced by the coupling structure.

### 3.5 TIME DISTORTION

The results obtained by Kino, et al.<sup>9</sup> for coarse grating constructions and the results we obtained on similar devices (which are subsequently discussed) tend to confirm the conclusion that lower conversion loss is obtainable. However, for convolution times of about 15  $\mu$ sec, we found that the time distortion associated with long convolution times becomes very serious. An adequate solution to this problem was not achieved.

The time distortion appears even in plate coupled devices. What happens is that for given input signals the magnitude of the convolved output is a function of the relative delay between the signals. For signals injected simultaneously, the acoustic signals overlap at the center of the convolution region.

As one signal is delayed with respect to the other, the acoustic overlap occurs nearer the other end of the convolution structure. The greater the relative delay, the nearer to the end of the structure this overlap occurs. This effect was measured with the device shown in Fig. 30. The input transducers were 5-finger-pair periodic transducers centered at 146 MHz. (The other transducers were different designs not used for this test.) The extra aluminum triangles at the ends of the structure are intended to compensate for the beam refraction caused by

M8616

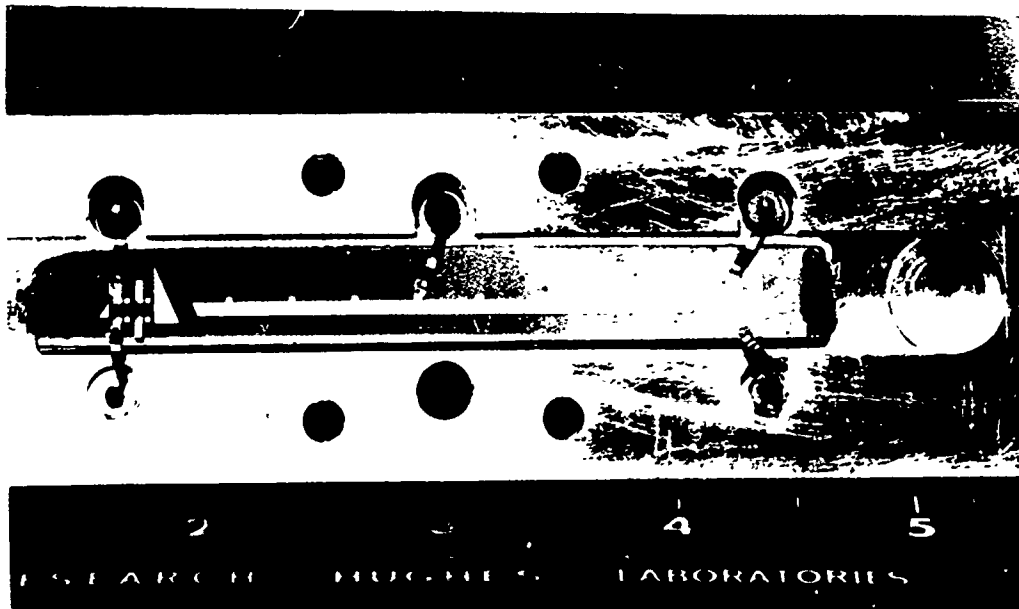


Fig. 30. Narrow Band, Plate Coupled Convolution Filter.

the angled ends of the parallelepiped convolution plate. Without these compensating triangles the beam refracts at the entrance to the convolution plate and tends to be deflected out of the straight path between the inputs. The coupling plate will accommodate a 16  $\mu$ sec integration time. Figure 31 shows the output as a function of delay between 3  $\mu$ sec input pulses at a frequency of 146 MHz. The response is not symmetrical, but reference to Fig. 30 also shows that the mechanical construction is not symmetrical. The contact to the convolution plate is to left of center, while the plate is shifted slightly to the right of the center between transducers. (This latter effect was caused by the inclusion of several possible sets of input transducers in the mask design for this device.) We believe this effect is a consequence of the fact that the length of the convolution plate is approaching the electrical wavelength in the structure at the output frequency (292 MHz). This is made plausible by noting that the relative dielectric constant of lithium niobate is about 40. The wavelength of an unbounded electromagnetic wave in  $\text{LiNbO}_3$  is thus only about 15.8% of the free-space wavelength. At 292 MHz, the free-space wavelength is 103 cm, thus only 16.2 cm in lithium niobate. The length of the convolution plate in the device is 5.1 cm, a significant fraction of the unbounded wavelength. The convolution plate is thus acting as a stripline whose length is a significant fraction of the electrical wavelength. The external impedance that a convolution signal, generated by the acoustic overlap of two signals within the plate, can thus depend upon the position of that signal in the convolution structure. The way in which the impedance to the load is transformed depends upon the length of the intervening line up to the connection and upon the length of the line to the open terminations of the structure itself. As noted in later results using the coarse grating coupler, the time distortion becomes even greater in that case. This is again qualitatively consistent with the explanation, for the larger capacitance per unit length of the coarse grating structure will even further decrease the electrical wavelength in the structure.

### 3.6 COARSE GRATING COUPLERS

As noted in Section 3.4, use of a coarse grating construction for the coupling region has the advantage that the capacitance, per unit length, of the coupling structure is increased. The conversion efficiency for a given output circuit  $Q$  is thus increased in proportion. A second advantage of the coarse grating construction is that the two input transducers operate at different frequencies. This can be used to eliminate the spurious signal caused by double transit echos produced by reflections from the input transducers. The two transducers operated at different frequencies no longer reflect each others' signals.

The use of the coarse grating coupler does impose a limitation on the allowable bandwidth of the input signals. Namely, the bandwidth cannot exceed twice the frequency difference of the two input signals. The reason for this is that it is assumed in this device that the input from one signal is higher by some  $\Delta\omega$  than the frequency from the second input and that correlation is obtained only if  $\omega_1 = \omega_2 + \Delta\omega$ . However, if the first signal contains frequencies at  $\omega_1 = \omega_2 - \Delta\omega$ , an output will also be obtained, which will introduce a spurious signal in the convolution output as if  $\omega_{1 \max} - \omega_{1 \min} = 2\Delta\omega$ . Spurious convolution signals will result.

Kino, *et al.*<sup>9</sup> have shown that when an extended coarse grating coupler is placed on a lithium niobate convolver, the surface wave is severely attenuated by scattering into bulk waves. This occurs because the long periodicity of the coarse grating coupler allows a phase match between the surface wave and higher velocity bulk waves. Kino has tested two solutions to this problem, both of which work. First, the coarse grating may be placed on adjacent piece of material (e. g., glass) and spaced slightly away from the substrate (Fig. 32). This reduces the interaction of the metal film with the substrate and the variation of acoustic impedance caused by this interaction, thus reducing the strength of the bulk wave scattering. Alternately, the spacing may be obtained by depositing a dielectric film between the piezoelectric substrate and the subsequently deposited metal coarse grating structure.

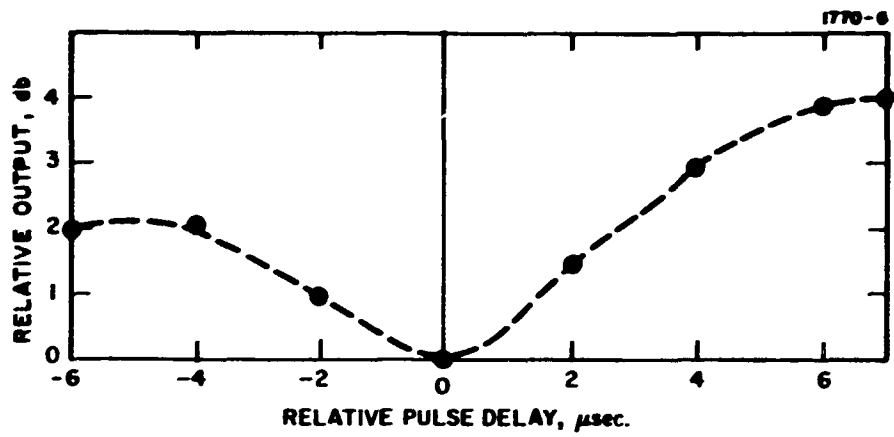


Fig. 31. Time Distortion in Plate Coupled Convolver.

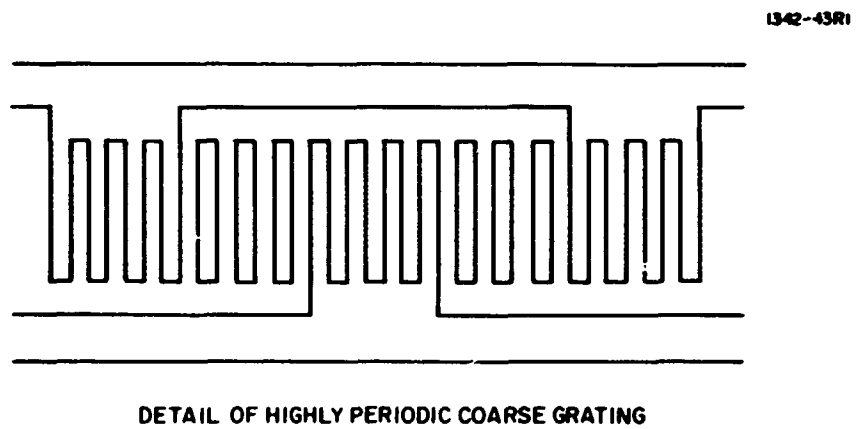


Fig. 32. Coarse Grating Constructions.

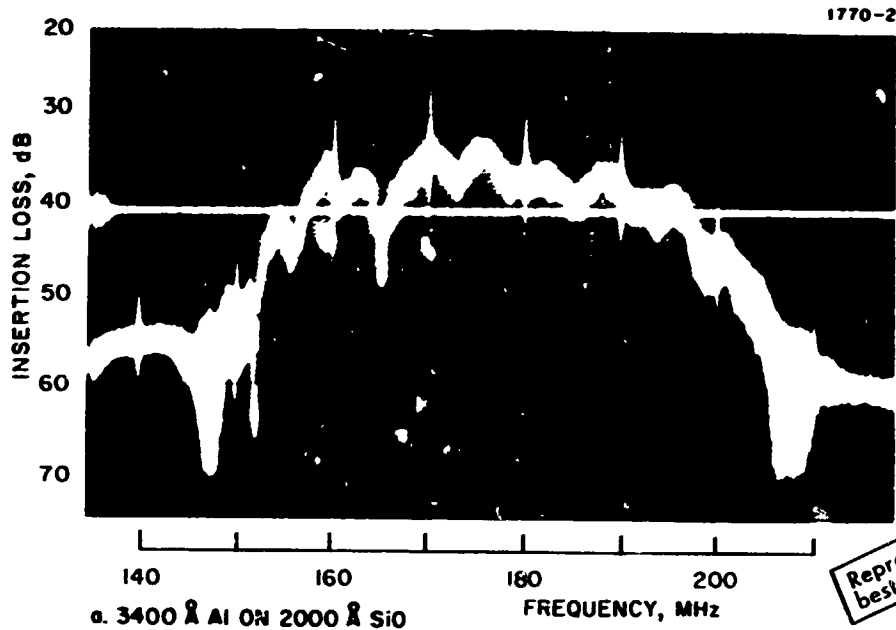
This procedure has been proved to be effective, but it has two disadvantages. First, there is some additional acoustic path attenuation in the dielectric film (SiO<sub>2</sub> was used). Second, the film may introduce some dispersion in the propagation velocity of the surface wave.

An alternate scheme was tested in our laboratories. The idea is to artificially increase the periodicity of the coarse grating structure, as shown in Fig. 32, so that the period is smaller than that of the highest frequency surface wave that is used. This periodicity is obtained by subdividing the fingers in the coarse grating structure and using dummy fingers in the intervening spaces to obtain a higher frequency acoustic period. In this case, it was thought that phase matching to bulk waves is no longer possible because the grating conditions for coherent radiation of the bulk wave are not satisfied, since the basic periodicity of the finger structure is now 7 times 30 or 210 MHz above the input acoustic frequencies that were used.

In order to test a structure with a coarse grating, a mask was ordered which had a 3.5 cm long (10  $\mu$ sec) 30 MHz coarse grating interposed between 5-finger-pair input transducers centered at 146 and 176 MHz, and an alternate mask with the subdivided fingers in the coarse grating. In fact, these input transducers were part of the same transducer pattern shown on the plate coupled device discussed in the previous section. Both 146 and 176 MHz input transducers are available at each end of this pattern. In this way, one can use a pair of matching transducers and measure the transmission loss through the grating.

The subdivided grating concept did not work. After the fact, one may recognize that the fingers in this structure are in fact not all electrically identical. First of all, alternate sets are connected to different summing bars; second, the fingers interposed in the gaps between the sets connected to the summing bars are electrically floating. Thus there still remains in the structure a basic periodicity of 30.5 MHz. As a result, broad residual stop bands were observed at 150 and 180 MHz.

Attention was then focused on the coarse grating structure using an SiO<sub>2</sub> layer between the niobate and an aluminum coarse grating structure. Figure 33(a) shows the transmission through the coarse grating



Reproduced from  
best available copy.

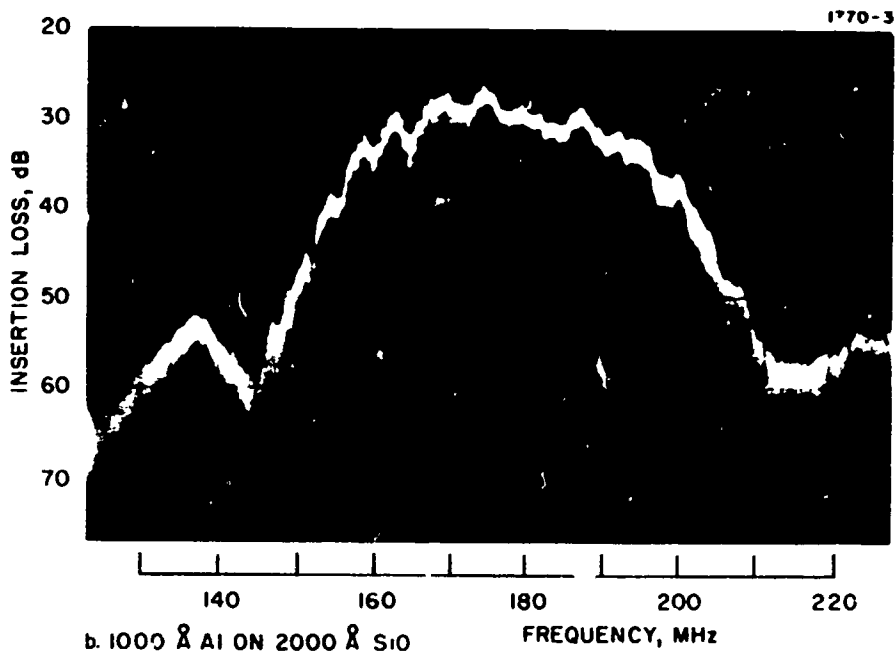


Fig. 33. Transmission through Coarse Grating.

using a layer of thermally evaporated SiO of 2000 Å and a thickness of 3400 Å for the aluminum fingers. These tests were conducted with untuned input 176 MHz transducers. It is clear that some frequency dependent scattering is still evident. The aluminum thickness was then reduced to 1000 Å by slow etching the aluminum. The final aluminum thickness was 1000 Å. The transmission through the coarse grating after this treatment is shown in Fig. 33(b). Not only has the insertion loss decreased, but the magnitude of the irregularities has lessened. From these results, it was decided to use a SiO thickness of 2000 Å for the device and an aluminum thickness of 750 Å, which is essentially that suggested by Kino. The transmission measurement when the frequency was swept very slowly also showed sharp stop bands at the fifth and sixth harmonics of the coarse grating, e. g., 152.5 and 183 MHz. (Deviations from 150 and 180 are probably due to a change in velocity under the structure.) The stop band at 153 MHz is clearly shown in the data of Fig. 33.

As a result of the above experiments the device was redesigned. Input transducers consisting of 5-finger-pair periodic designs at 195 and 225 MHz were provided. The 10 μsec long 30 MHz coarse grating design was retained. This places the input frequencies between the harmonic stop bands, nominally at 180, 210, and 240 MHz.

A device was now fabricated in which the insertion loss at 195 MHz was measured at each stage of the process. The results are tabulated in Table III.

TABLE III  
Insertion Loss Measurements

Stage	Untuned Insertion Loss, dB	Tuned Insertion (series inductor), dB
Transducers Only	18	—
Add 2000 Å SiO	20.5	—
Add Coarse Grating, 750 Å Al	25.5	19

T647

The wiggles in the transmission over the 20% bandwidth were less than  $\pm 0.5$  dB. Sharp stop bands symmetrically placed at  $\pm 15$  MHz with respect to the center of the passband were found as expected. From these results we then obtained an attenuation of  $0.25$  dB/ $\mu$ sec due to the SiO and an additional  $0.5$  dB/ $\mu$ sec due to scattering by the coarse grating. The device was then mounted as shown in Fig. 34. An additional aluminum evaporation was performed to increase the thickness of the aluminum on the sum bars to  $5000 \text{ \AA}$ . This was done in order to minimize the parasitic resistance in the structure. In addition, multiple connections were made to the sum bars in order to attempt to minimize the time distortion effect previously discussed. It may be noted that tests were first made with only a connection to the center of the sum bars, and that the construction shown did improve the results. As will be seen, very serious time distortion remained.

The conversion efficiency for this device was measured with simultaneous  $5 \mu$ sec input pulses displaced in frequency by  $30$  MHz. The input transducers were tuned with series inductors. The output was tuned using a shorted strip line tuning network. This tuner consists of a section of strip line with an adjustable sliding short and an adjustable tap that is connected to the output load.

The output tuner short and tap positions were adjusted for maximum output at  $192$  MHz for the measurements shown. This tuning adjustment was held constant as the input frequencies were changed. The results are shown in Fig. 35. The minimum conversion loss factor  $P_o/P_m^2$  of  $-94 \text{ dBm}^{-1}$  for  $5 \mu$ sec input pulses may be compared with the results later given for a plate coupled device using 5-finger-pair periodic transducers (operating at  $146$  MHz) and with the output and input similarly tuned. The results for the plate coupler gave a minimum conversion efficiency factor of  $-98 \text{ dBm}^{-1}$ . The insertion loss of the transducers on the plate coupled device was  $15$  dB, or  $4$  dB better than the indicated insertion loss of  $19$  dB for the coarse grating.

Reproduced from  
best available copy.

118617

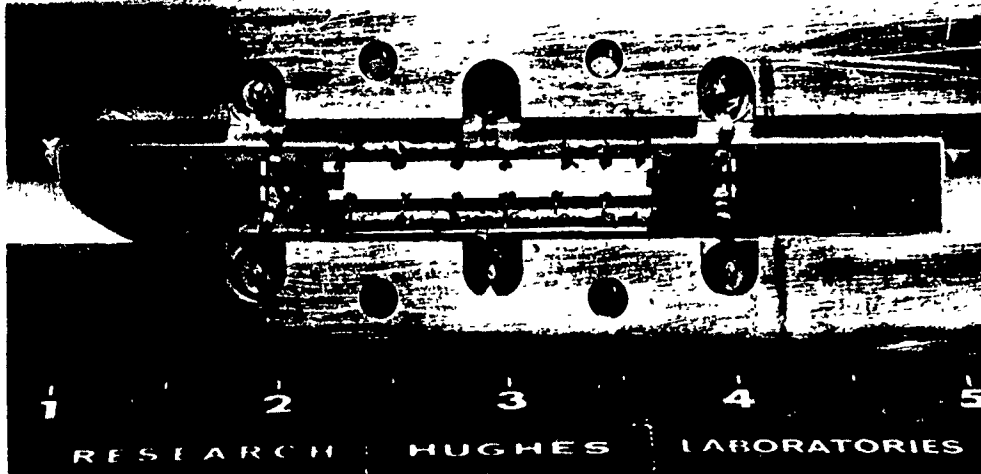


Fig. 34. Mounted Coarse Grating Convolver - 195 and 225 MHz Inputs.

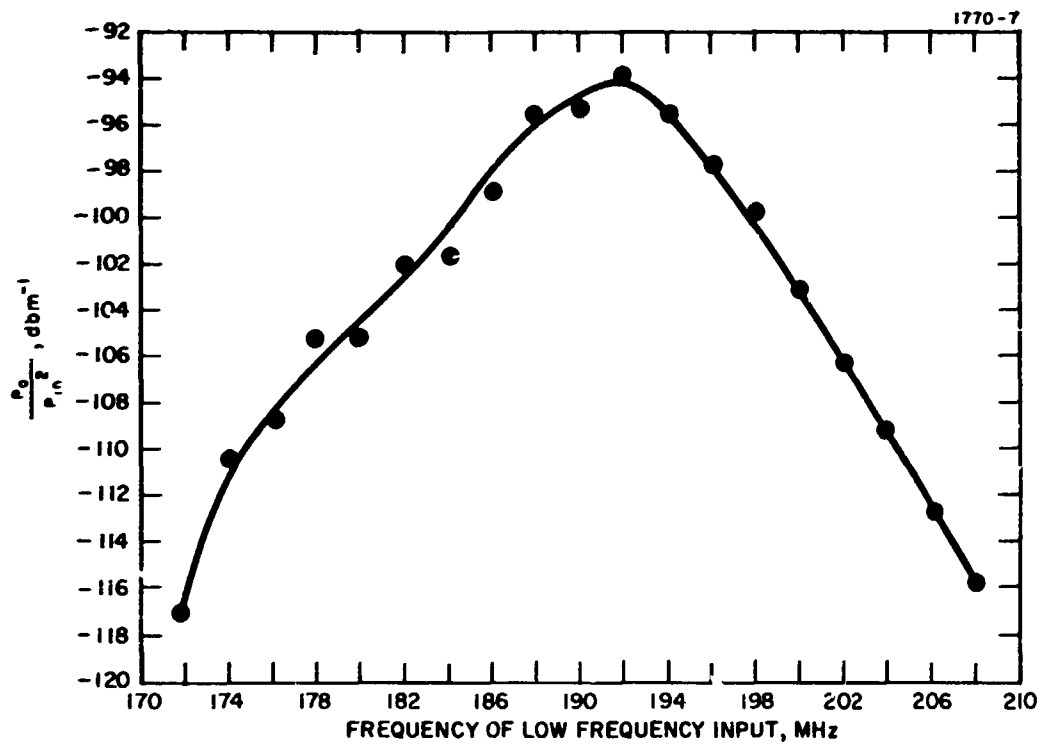


Fig. 35. Coarse Grating Conversion Factor.

The coupling length on the plate coupled device was 16  $\mu$ sec, however, compared to 10  $\mu$ sec for the coarse grating coupler. This should result in a relative decrease of  $(16/10)^2$  or about 4 dB, compensating for the increased transducer efficiency. This comparison then, favors the coarse grating coupler by 4 dB. Further measurements on the time distortion in the coarse grating device indicate that this is a conservative estimate, because the output increased in excess of 10 dB as the relative input times were displaced, producing an acoustic signal overlap near the ends of the coarse grating structure.

The time distortion in this device is shown in Fig. 36; 2  $\mu$ sec pulses were used for this measurement. The dropoff at the very ends occurs when the convolution region no longer contains all of the pulses. The difference between maximum and minimum conversion efficiency was 17 dB. Thus the time distortion in this device is very severe and makes the device unacceptable in its present form.

### 3.7 DIFFRACTION EFFECTS

As discussed in the design section, the output power of the acoustic surface wave filter is inversely proportional to the square of the acoustic beam width for fixed input power level. In the case that the device is to be optimized for maximum conversion efficiencies at lower moderate input power, it is desirable to minimize the width of the structure. However, the aperture of the device cannot be decreased indefinitely, because acoustic beam spreading becomes significant at smaller apertures. The acoustic beams from the two inputs will diverge and not overlap completely. This is illustrated in Fig. 37.

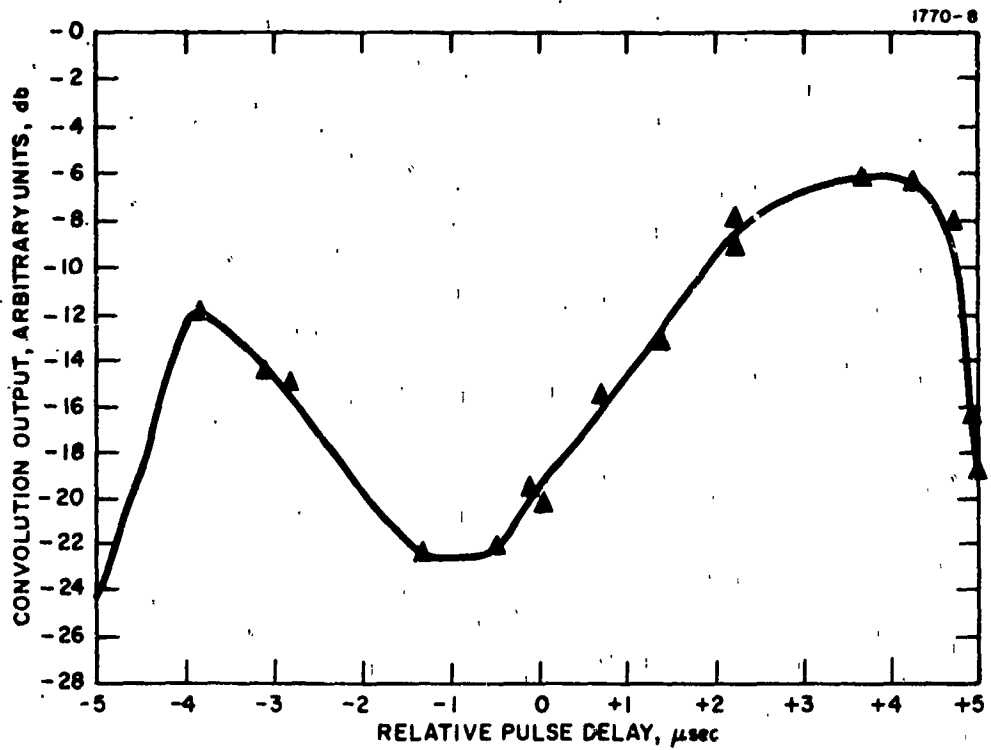


Fig. 36. Time Distortion in Coarse Grating Coupler.

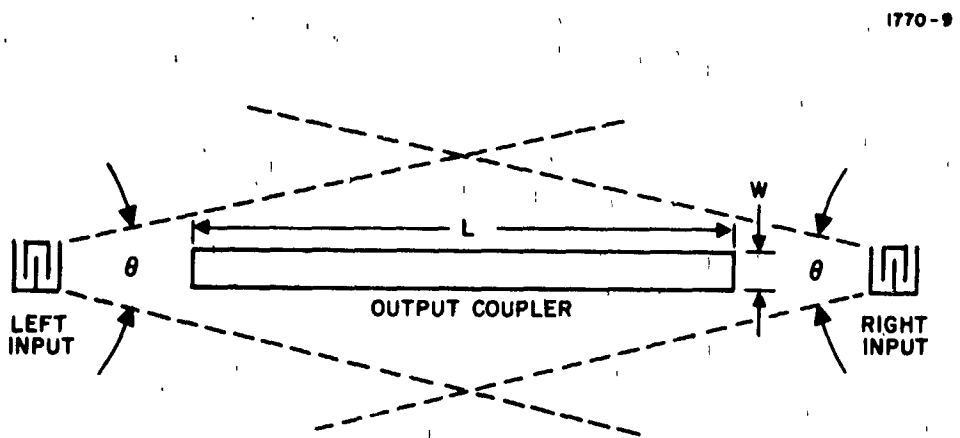


Fig. 37. Schematic Representation of Beam Spreading.

Acoustic surface wave signals of finite aperture generated on the surfaces of polished crystals will, in general, spread and distort during propagation to produce non-straight-crested waves of nonuniform amplitude due to diffraction. This causes a reduction in the convolutor output signal at  $\omega_1 + \omega_2$  due to slight mismatch of the two input signals in amplitude and phase over the area of the output electrode(s). A calculation of the full effect of diffraction mismatch, both transverse to and along the direction of propagation, has not been carried out as yet; however, we can approximate the effect of diffraction by assuming that the main contribution is caused by beam spreading. We neglect any phase errors along the axial direction.

The phase velocity  $V_s$  of acoustic surface waves for the materials and orientations considered for use in this application can be written as

$$V_s = V_o(1 - b\theta^2)$$

where  $\theta$  is the angle of ray propagation with respect to the collinear direction. It is assumed that the transducer electrodes are normal to the crystal collinear propagation direction. It is found that the diffraction in a particular material and orientation can be characterized by the anisotropy constant  $b$ . The far-field diffraction can be used for the design of the acoustic convolution filter to indicate the aperture for which diffraction losses are important.

For this case one may write

$$\theta = \frac{2.78}{\pi} \frac{\lambda}{W} |1 - 2b|$$

The acoustic energy under the convolution plate from the right and left transducers can then be written approximately as

$$P_R = P_o \frac{W}{W + \theta X}$$

$$P_L = P_o \frac{W}{W + (L - X)\theta}$$

where  $P_o$  is the input power at the input to the convolution region. The convolution output generated at any position can then be written as:

$$P_R P_L = \frac{P_o^2 W^2}{W^2 + WL\theta + \theta^2 (L - X)X}$$

At the ends of the plate this reduces to

$$P_R P_L = \frac{P_o^2 W^2}{W^2 + WL\theta}$$

and at the middle to

$$P_R P_L = \frac{P_o^2 W^2}{(W + L\theta/2)^2}$$

Two criteria may be derived from the above expression:

(1) The power output must not be greatly reduced by diffraction. The loss is the greatest at the center of the convolution region where  $P_o^2$  is reduced by the factor  $W^2/(W + L\theta/2)^2$ . For a 3 dB loss, for example, this requires

$$W \geq 1.22 L\theta$$

On Y-Z lithium niobate, where  $\theta = 0.106 \lambda / W$  for an acoustic wavelength  $\lambda$ ,

$$\left(\frac{W}{\lambda}\right) \geq 0.123 \frac{L}{\lambda}$$

For  $L = 5$  cm,  $\lambda = 2.4 \times 10^{-3}$  cm (at 146 MHz)

$$W \geq 0.04 \text{ cm}$$

The minimum aperture used in the constructed devices was 0.125 cm and was imposed by the precision with which alignment of the device with the axis could be maintained during fabrication.

(2) The fact that the available power is a function of position can lead to a time distortion of the kind that has been observed. However, for the dimensions of the constructed devices, this cause of time distortion is calculated to be negligible. Again for  $L = 5$  cm,  $\lambda = 2.4 \times 10^{-3}$  cm,  $W = 0.125$  cm, the ratio of  $P_R P_L$  at the center to  $P_R P_L$  at the ends is only 1.002. This very small number is the result of the fact that for an end to center ratio of two it is only required that  $W \geq 0.102 L \theta$ .

### 3.8 PROPAGATION LOSSES

The insertion losses obtained in our devices were always greater than the theoretical predictions. Moreover, in these cases where simple periodic input transducers were used, it is possible to estimate the insertion loss from measurements of the input impedance of the transducers. In these cases also, the measured insertion losses always exceeded those deduced from the input impedance measurements. As a consequence, a series of measurements was attempted to directly measure the propagation losses associated with the aluminum films. Using a delay line operating at 190 MHz, two tests were performed in which the untuned line insertion loss was measured before and after aluminum deposition over a 5 cm (or 15  $\mu$ sec) section of the line.

Two thicknesses of aluminum were tested, 3000 and 700 Å. The results are given in Table IV. The 700 Å film gave an attenuation of 0.13 dB/μsec; the 3000 Å film produced an attenuation of 0.47 dB/μsec.

TABLE IV  
Aluminum Film Attenuation

Test No.	Test Condition	Attenuation, dB
1	No Al	28
	700 Å Al	30
2	No Al	28
	3000 Å Al	35

T648

The conclusion is that significant acoustic scattering losses were present in the evaporated aluminized films.

### 3.9 DISPERSION EFFECTS

One limitation of all the structures that have been used is that the dispersion in the coupling structure will limit the available instantaneous time bandwidth. The phase dispersion that is introduced has not been measured directly, but for the plate coupled structures may be estimated from the known propagation in the aluminum film regions.

It is generally understood that the velocity of propagation of surface waves on aluminized piezoelectric substrates is slightly frequency dependent or dispersive. Figure 38 shows this effect for aluminum on Y-Z lithium niobate and on ST quartz. In these examples, the velocity decreases with increasing frequency. A wideband pulse propagating through such a dispersive medium undergoes phase distortion of the Fourier components of the pulse proportional to the

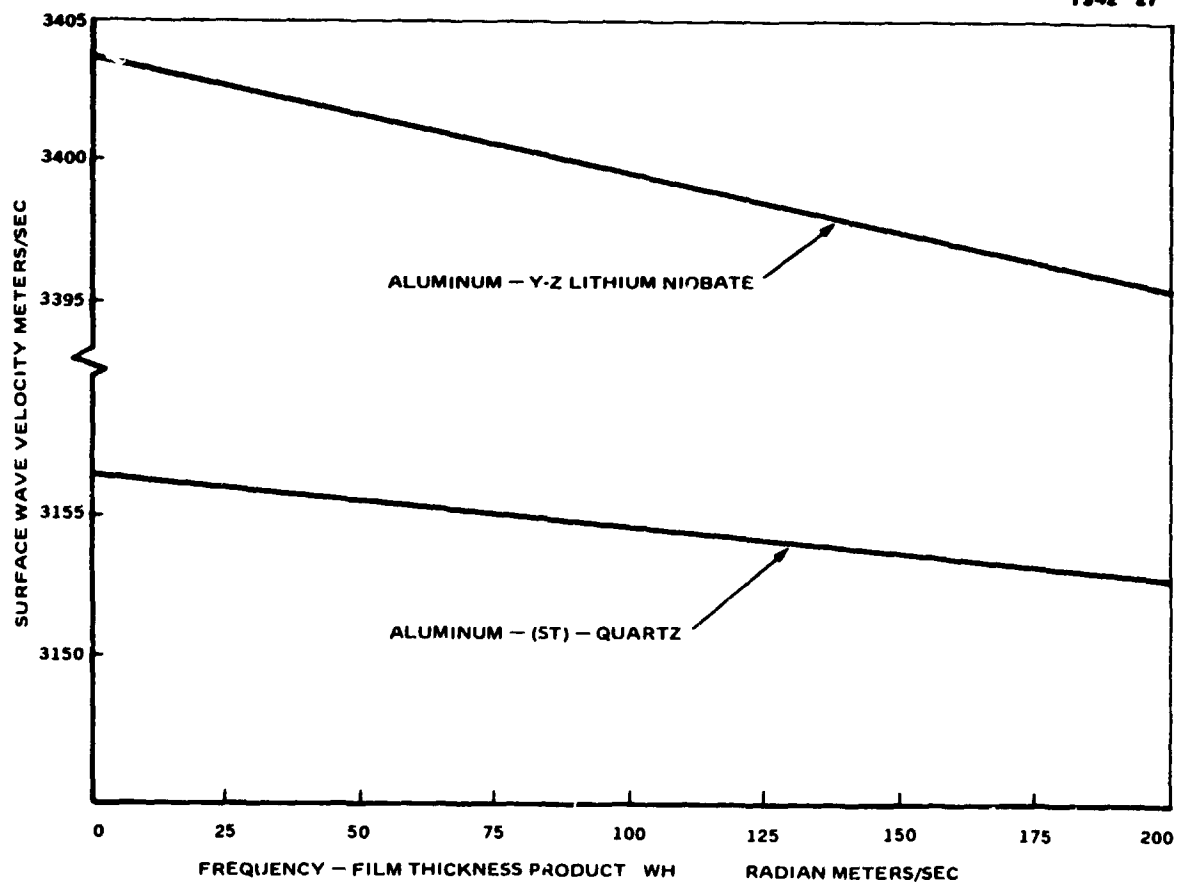


Fig. 38. Dispersion Curves for an Aluminum Film on Y-Z Lithium Niobate and ST Quartz.

propagation path length and the frequency. Consider the linear FM or CHIRP pulse propagating through the dispersive medium (see Fig. 39). If the pulse starts with low frequencies and ends with high frequencies it becomes slightly expanded as it propagates through the dispersive medium. If the CHIRP is reversed (high and then low) it becomes slightly compressed. In the convolver device considered here, if the signal fed from one end is down-CHIRPed, then the signal from the opposite end must be up-CHIRPed in order for the oppositely traveling wave trains to match up at the same position within the convolution circuit. The dispersive effect will cause one of these wave trains to be shortened and the other lengthened, so that complete overlap of the two waveforms can not be accomplished. If we represent the dispersive velocity  $V(f)$  by

$$V(f) = V_0 - \alpha f$$

Where  $\alpha$  is the slope of the velocity versus frequency curve and  $f$  is the frequency, it can be shown that a linear FM pulse starting at frequency  $f_1$  and ending at frequency  $f_2$  that propagates over a path for time  $T$  will have its linear dimension  $L$  increased or decreased by  $\Delta L$ , where

$$\Delta L = \alpha (f_2 - f_1) T$$

In the convolver the relative length change is  $2\Delta L$ , because one wave train expands while the other contracts. This corresponds to a phase shift  $\phi$  given by

$$\phi = 2\pi (2\Delta L / \lambda_2) = 4\pi \frac{\Delta V_2}{V_2} (f_2 f_1) T$$

where  $\lambda_2$  is the wavelength at frequency  $f_2$ , and we are assuming that the wave trains are aligned at  $f_1$ .

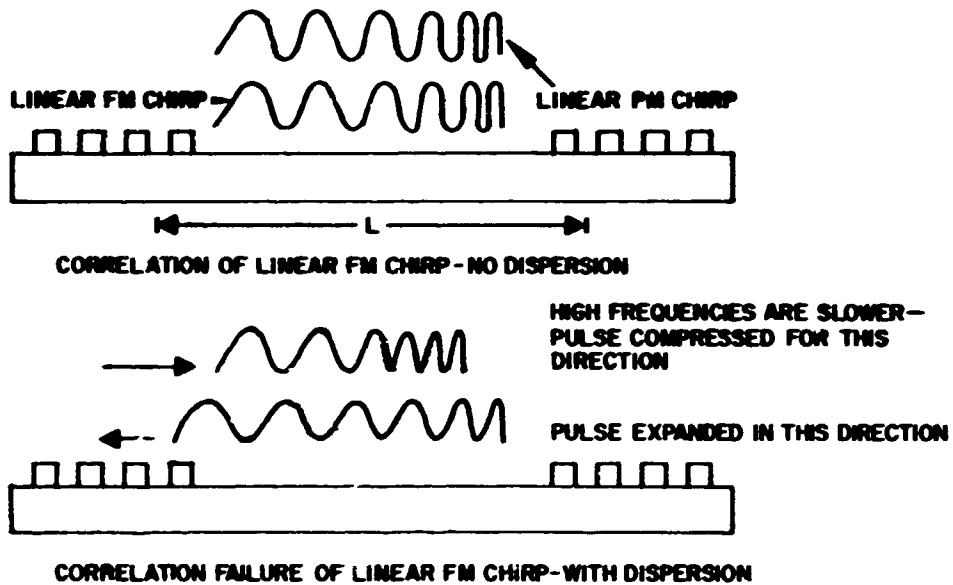


Fig. 39. Pulse Distortion due to Dispersion in Surface Wave Correlation.

If one requires that the position shift of the waves when aligned on one side be much less than one cycle on the other side, one obtains the relationship

$$\frac{\Delta V}{V} \ll \frac{1}{2T \cdot BW}$$

where  $T \cdot BW$  is the time-bandwidth product of the surface wave delay line convolver system.

The propagation dispersion in the aluminum film may be estimated from some direct measurements of acoustic surface wave velocity on bare and Al metallized Y-cut Z-propagating lithium niobate.<sup>10</sup> The results for propagation at 100 MHz are summarized in Table V.

TABLE V  
Results of Aluminum Propagation at 100 MHz

Surface Thickness	$\Delta V/V$
430 Å Aluminum	$2.24 \times 10^{-2}$ (mainly electrical shorting, the accepted value of $2.4 \times 10^{-2}$ is within experimental error)
5400 Å Aluminum	$2.78 \times 10^{-2}$ (electrical shorting plus dispersion)

T649

Aluminum films are considered here as one form of the metallized correlator circuit used for detecting the output signal. This is because of all the metal films we have investigated, aluminum is the best acoustic match to lithium niobate and shows the lowest propagation dispersion.

From this we see that for a 5000 Å film, the surface wave velocity is changed by 0.5% at 100 MHz because of acoustic loading of the surfaces. Thus, assuming a linear dependence on film thickness, we may estimate that the acoustic velocity dispersion is equal to 0.3% for a 3000 Å film at 100 MHz or equally for a bandwidth of 100 MHz. It may be noted that this experimental value is in agreement with calculated dispersion curves shown in Fig. 38.\* From this then, one may estimate that the instantaneous time-bandwidth using a 3000 Å film as used in the constructed devices is given by

$$T \cdot BW < \frac{1}{2} \cdot \frac{V}{\Delta V}$$

resulting in

$$T \cdot BW < 167$$

Film as thin as 750 Å have been tested as indicated in the discussion on propagation losses. Such film would provide a time-bandwidth of ~670.

Dispersion effects in insulating films must also be considered in the design of the interdigitated coarse grating coupler, which is an alternative to the aluminum plate coupler. The coarse grating coupler, when placed in intimate contact with the LiNbO<sub>3</sub> surface, generates bulk waves which tend to interfere with the operation of the correlator device. This mechanism is also a source of increased signal attenuation. One solution to this problem is to elevate the coarse grating

---

\* According to the last equation in this section, this indicates that instantaneous time-bandwidths of several hundred may be achieved. However the distortions (e. g., time sidelobe levels in compressed pulses) may be significant in some cases.

above the substrate by means of spacer rails. Another solution is to use an insulating layer such as  $\text{SiO}_x$  between the grating and the substrate. This can reduce the bulk wave effects caused by electromechanical interaction to a tolerable level at the expense of correlation efficiency. However, the presence of an insulating layer on the substrate will produce dispersion similar to that observed for aluminum layers. Figure 40 shows the measured attenuation and dispersion for  $\text{SiO}_x$  film on ZX  $\text{LiNbO}_3$  measured by W. R. Smith.<sup>11</sup> The dispersion ( $\Delta V/V$ ) measured between  $k_0 h = 0$  and 1.5 is equal to 2.63%. Thus for a 2000 Å thick film, the dispersion for a 100 MHz bandwidth is ~0.06%; the limiting instantaneous time bandwidth produced by  $\text{SiO}_2$  dispersion is about 1660. Experience with layer systems indicates that these values will not change drastically in the Y-Z  $\text{LiNbO}_3$  system.

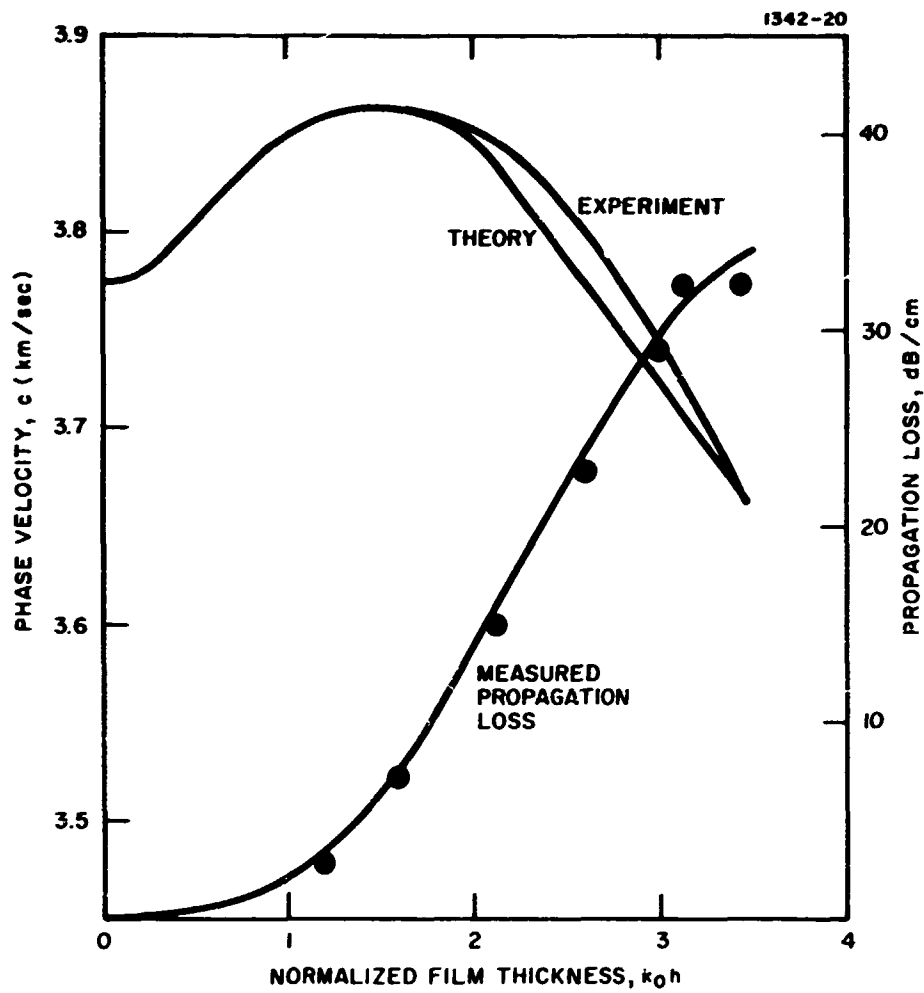


Fig. 40. Phase Velocity and Propagation Loss for  $\text{SiO}_2$  Film on Lithium Niobate.

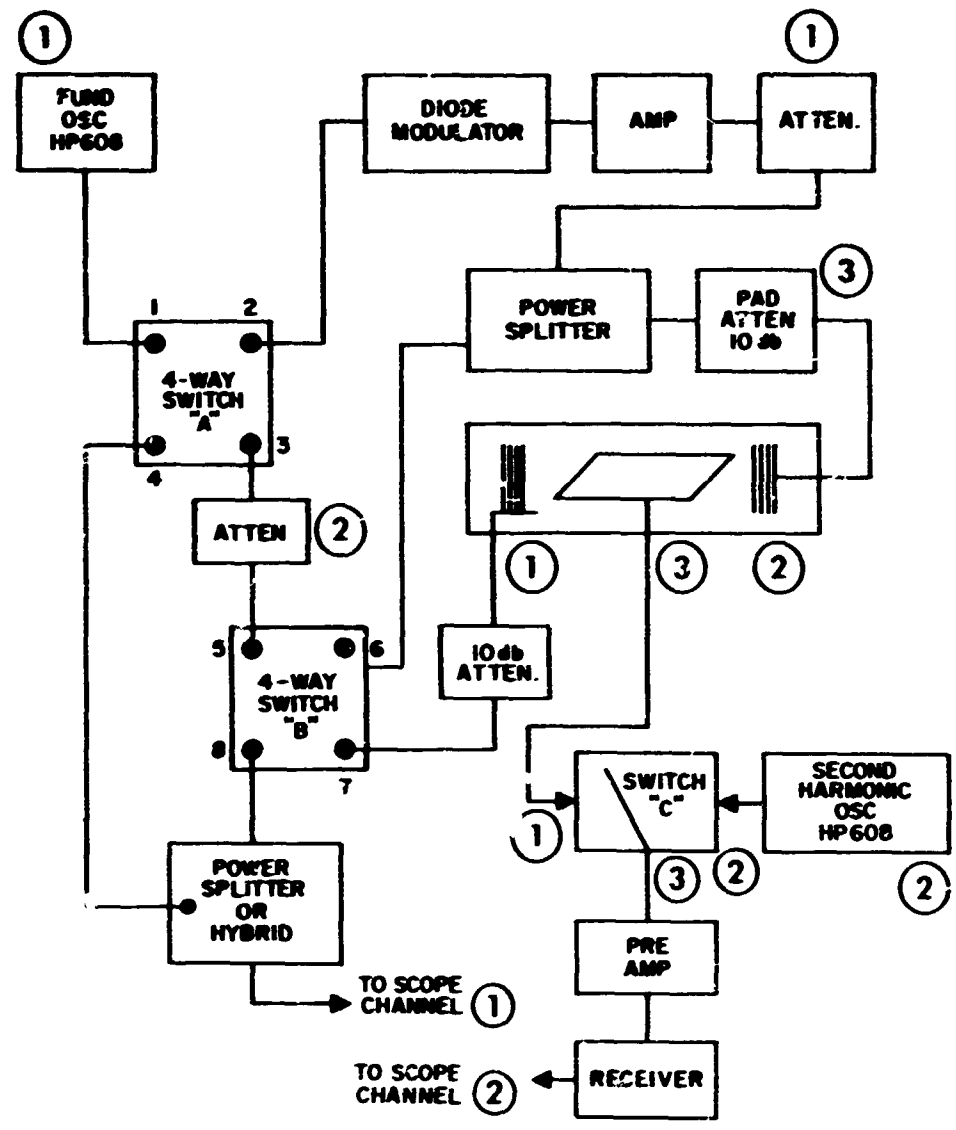
#### 4. DEVELOPMENT OF ELECTRONIC MEASUREMENT APPARATUS

During the course of this program, apparatus were developed and assembled to test acoustic surface wave correlators. Three distinct variations of the available equipment were used to test the autoconvolution efficiency of plate output coupler devices, the crossconvolution efficiency of course grating output coupling devices and the pulse compression efficiency of plate coupling devices using linear FM CHIRP signals. Details of these apparatus are given in the following paragraphs.

##### 4.1 AUTOCONVOLUTION APPARATUS

The first test setup developed under this contract was designed to test the autoconvolution efficiency of plate output coupler, acoustic surface wave correlator devices. This efficiency parameter is derived from measurement of the transduction efficiency of the transducers, the input power to the devices, and the correlated output power. A measurement setup was thus designed which was capable of measuring these parameters by routing signals through coaxial switches so that connections to the device would not have to be changed for each measurement at each given frequency. A diagram of the test apparatus is shown in Fig. 41. For measuring the correlated output power of the device, the signals are routed through the paths described in the following paragraphs.

The input signal was generated in the HP 608 oscillator (1) and routed through switch A from channel 1 to channel 2, thence on through a Relcom S1 diode switch, an Avantek AV8 amplifier, and a Hewlett-Packard coaxial attenuator. This portion of the circuitry is used to shape the signal, after which it passes through a power splitter. One-half of the power passes through a 10 dB attenuator to input No. 2 of the correlator device. The other half of the power passes through switch B (4-way) from terminal 6 to terminal 7 through a 10 dB attenuator to input No. 1 of the device. The correlated output signal at



- ① TRANSDUCER LOSS 20 db TOO LARGE
- ② POWER INPUT 10 db TOO LARGE

Fig. 41. Plate Coupled Convolver Test Apparatus.

the input frequency passes from terminal 3 of the device through terminals 1 and 3 of switch C, through a wideband preamplifier to a tunable receiver. The output of the receiver is displayed on a Tektronix 545 oscilloscope. To measure the correlated output power, switch C is activated to its second position so that a CW comparison signal from oscillator 2 passes from terminal 2 through terminal 3 of switch C to the preamplifier and the receiver. The comparison oscillator frequency and amplitude are adjusted to match the correlated output signal observed on the oscilloscope face, and the calibrated attenuator reading on the oscillator yields the device output power.

The input power was measured by flipping switch B to its alternate position so that half of the input power is routed from terminal 6 to terminal 5 of switch B through attenuator 2, through terminals 3 and 4 of switch A to a power splitter, and thence to channel 1 of the oscilloscope. By alternating the positions of switch A and adjusting attenuator 2 it is possible to compare a 1 mW (0dBm) CW signal from the fundamental oscillator with the attenuated pulsed signal used to perform the correlation experiment. The reading of the attenuator thus obtained is 10 dB greater than the input power to the correlator because of the 10 dB pads used to isolate the device from the generator circuitry. This measure was found necessary for the elimination of frequency tuning effects caused by VSWR in the system.

Measurement of transduction loss was accomplished by allowing switch A to remain in the position with inputs 1 and 2 connected and by switching the position of switch B so that the direct input power through terminals 6 and 5 could be compared with the power transmission through the device via terminals 7 and 8. Both of these signals pass through a matched hybrid coupler to the scope and thus are equally weighted. Again, adjustment of attenuator 2 is used to equalize the direct and the delayed signal. The attenuator reading is 20 dB greater than the insertion loss of the device, because one path contains both 10 dB pads and the other none. Aside from the details of performing the switching operations in proper sequence, the point by point data-taking process for each frequency was routine and repeatable.

The measurement technique did not depend on the calibration accuracy of oscilloscopes but made use of the accuracy of a pair of HP 608 oscillators. The oscillators were also checked against a power meter for further confirmation of the accuracy of their attenuated output from the power ranges used in the experiment.

The efficiency of the convolver devices was calculated from data obtained in this measurement apparatus according to the formula

$$\epsilon(\text{dB}) = P_{\text{out}}(\text{dBm}) - 2 P_{\text{in}}(\text{dBm})$$

where  $\epsilon(\text{dB})$  is the net efficiency in dB,  $P_{\text{out}}(\text{dBm})$  is the correlated output power in dBm at twice the input frequency and  $P_{\text{in}}(\text{dBm})$  is the input power to both terminals of the device in dBm. The efficiency of the correlation circuit normalized for the transduction loss of the delay line is given by:

$$F(\text{dB}) = P_{\text{out}}(\text{dBm}) - 2 P_{\text{in}}(\text{dBm}) + \text{TL}(\text{dB})$$

where  $F(\text{dB})$  represents the correlation efficiency of the device if it had no transduction or propagation losses, and  $\text{TL}(\text{dB})$  represents the transduction and propagation losses of the device. It is important to note that  $\text{TL}$  is the transmission loss of the delay line and  $\text{TL}/2$  is the loss associated with each transducer. However, since each transducer contributes to the input power, the total transmission loss appears in the equation.

#### 4.2 COARSE GRATING TEST APPARATUS

At a later date, a general test apparatus was developed for measurement of coarse grating convolvers where the two input signals would be at different frequencies. This system was also used for measurement of the convolution efficiency of plate output coupler

convolvers. However, it had a limitation: not being able to measure the transduction loss of the devices. That function was performed on the Hewlett-Packard network analyzer. A schematic diagram of the apparatus is shown in Fig. 42.

The apparatus consists of two separate pulsed rf signal generator systems, a common receiver system, and a calibrated comparison oscillator. The system was operated in the following manner. A CW signal from oscillator 1 (HP-608) was passed through a Relcom (S1) modulator to produce a rectangular pulse which was then amplified in the Avantek (AV-8B) amplifier No. 1 to about two-thirds of 1 W and passed through the variable attenuator No. 1. The signal was then fed via switch A either to a precision dc to 500 MHz oscilloscope for setting the input power level to the device or to device input 1 for ultimate measurement of the correlated output signal. A similar setup was used for channel 2. The 4-way switches A and B (Transco microwave M1460-30) were used to route the input power either to the device or to the scope. For measurement of the correlated output signal, the receiver was tuned until a maximum signal appeared on the low frequency oscilloscope with switch C in position 1. Then, switch C was turned to position 2 and oscillator 3 was tuned to give a maximum output signal at the scope following the receiver. The precision attenuator on oscillator 3 was then used to render the CW signal the same deflection size as the correlated output pulse. This was a relatively foolproof simple substitution measurement system. Note that for input channel 1 and input channel 2 at the same frequency (i. e.,  $f_1 = f_2$ ) the output signal occurred at  $2f_1$  and the harmonic oscillator 3 was tuned to  $f_3 = 2f_1$ . However, if  $f_1 \neq f_2$ , as in the case of the coarse grating output coupler, the harmonic oscillator 3 must be set at  $f_3 = f_1 + f_2$ . An HP 8010A pulse generator was used for generating the pulses to drive the Relcom S1 modulators and to provide the trigger for the oscilloscope sweeps. Any modulator with a good on-off ratio, e. g., even an HP mixer can be used here. The pulse generator requirements of a 1 to 5  $\mu$ sec pulse width at an amplitude of several volts can be met by most available laboratory type generators.

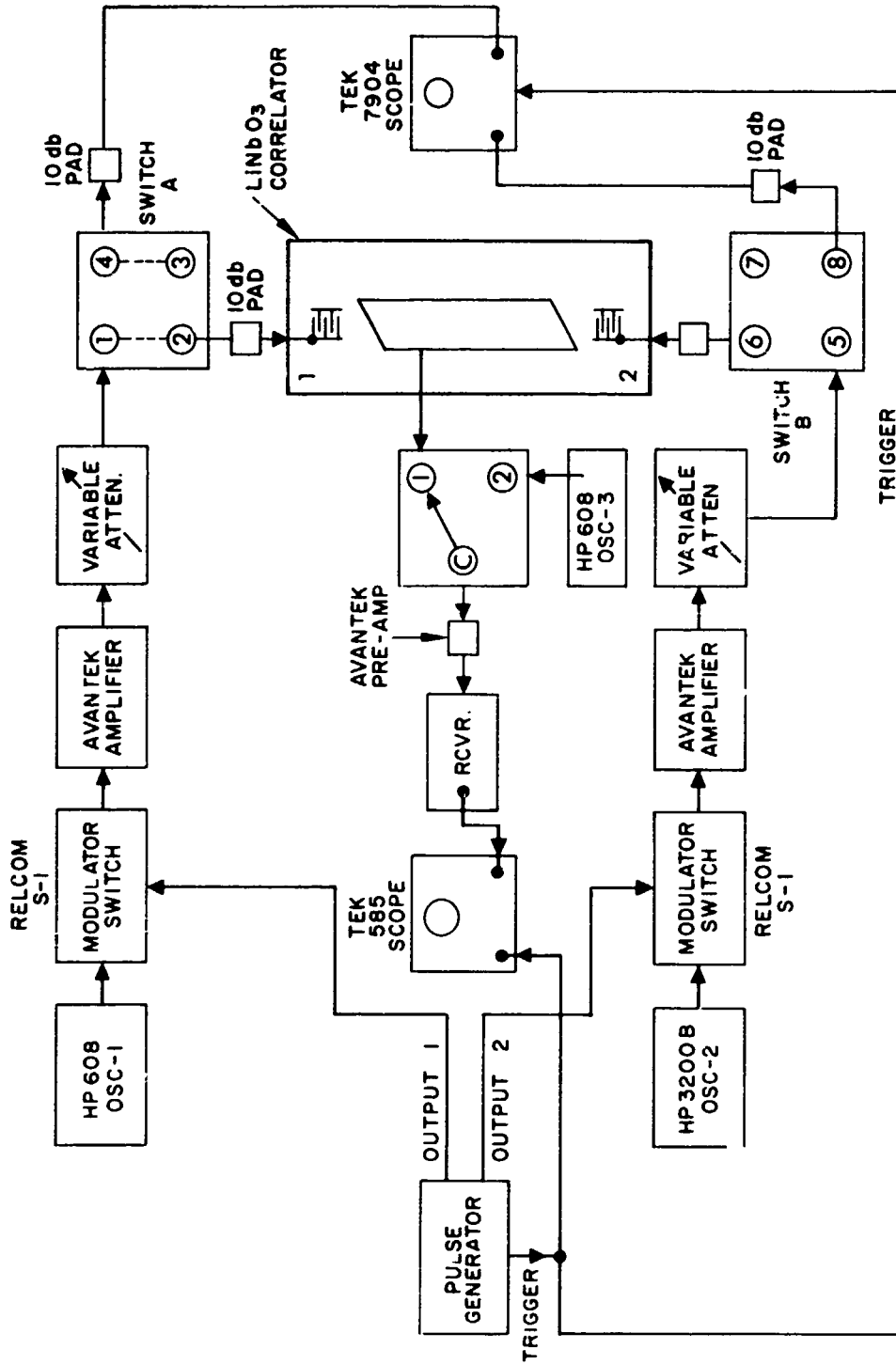


Fig. 42. Two-Input Acoustic Surface Wave Correlator Test Setup.

Padding attenuators of 10 dB have been placed between switches A and B and the scope and device channels. These served to reduce the maximum signal presented to the device and to reduce possible mismatch errors in the measurement of input power. Also, the pads were needed because the Tektronix 7904 scope cannot display the full available rf amplitude from the Avantek amplifier.

In our measurement setup, we have included an Avantek UTA214M amplifier before the receiver for good low noise performance and for a standardized  $50\Omega$  receiver input over the 5 to 500 MHz band. When output impedance matching networks were to be tested, they were connected between the correlator output terminal and terminal 1 of switch C. For the receiver itself, we used a Relcom M1 mixer and a HP 869B sweep oscillator cw operated. The mixer output was amplified via an RHG F30VAR i. f. amplifier and displayed directly on the Tektronix 585A oscilloscope. The variable attenuators used were HP models 355C and 355D.

These measurements were greatly facilitated by the use of switches A, B, and C. This eliminated the need for switching connections for each measurement at each frequency.

#### 4.3 FM CHIRP TEST APPARATUS

Part of the effort expended on this program was directed toward the development of a broadband linear FM CHIRP test system for measuring the performance of surface wave acoustic correlators as pulse compression devices. The heart of the test system was a voltage-tuned oscillator (obtained from Omni Spectra) that had a sweep range from 1 to 1.1 GHz and two mechanically tunable oscillators centered in the 900 and 1200 MHz range. The voltage tunable oscillator had a linearity of  $1/4\%$  at band center and corresponded to the state-of-the-art in commercially available swept oscillators in this frequency range. The frequency stability of this oscillator was dependent on factors such as sweep voltage stability, power supply voltage stability, and ambient temperature. The stability requirements

of the electrical supplies were met by purchasing high quality power supplies and pulse generators. The temperature stability requirement was met by placing all three of the oscillators in the system in a single regulated oven designated for operation at  $40^{\circ}\text{C} \pm 1^{\circ}$ . By using a large thermal mass for a heat sink, the thermal inertia of the system provided isolation against thermal fluctuations. The system was found to be stable in frequency for time periods exceeding one hour. After checking the frequency stability of the oscillator assembly, a system was constructed as shown in Fig. 43 which used two mixer circuits to heterodyne the outputs of the three oscillators. This resulted after suitable adjustment in a pair of signals, one of which swept from 100 to 200 MHz, while the other swept from 200 to 100 MHz as the voltage to the tuned oscillator was varied. Using a high frequency oscilloscope, the simultaneous generation of these up-swept and down-swept signals was verified. A 2 dB amplitude variation of output power over the swept range was observed. This was within the manufacturers' specifications.

The sweep frequency linearity was next checked in the ramp mode of operation using a wavemeter in the path of the swept oscillator output. Excessive deviation from linearity was observed, which was traced to an RC time constant in the biasing circuit to the oscillator. This network acts as a dc isolator for decoupling the ramp generator from the sweep voltage input terminal to the oscillator which must be dc biased. This is necessary because the varactor tuning network within the oscillator package is dc coupled for good low frequency response. Some simple design calculations led to the use of an extremely large capacitance in the coupling circuit and resulted in a more linear frequency sweep with time. Subsequent measurements indicated that some slight nonlinearity also existed in the voltage ramp used to drive the oscillator. It would have been possible to design a coupling network that could correct for all system nonlinearities, but at this point, the linearity was judged adequate for use with the 40 MHz receiver bandwidth. Therefore, we have concluded that it is possible to obtain the required linearity of FM sweep as a function of time to perform

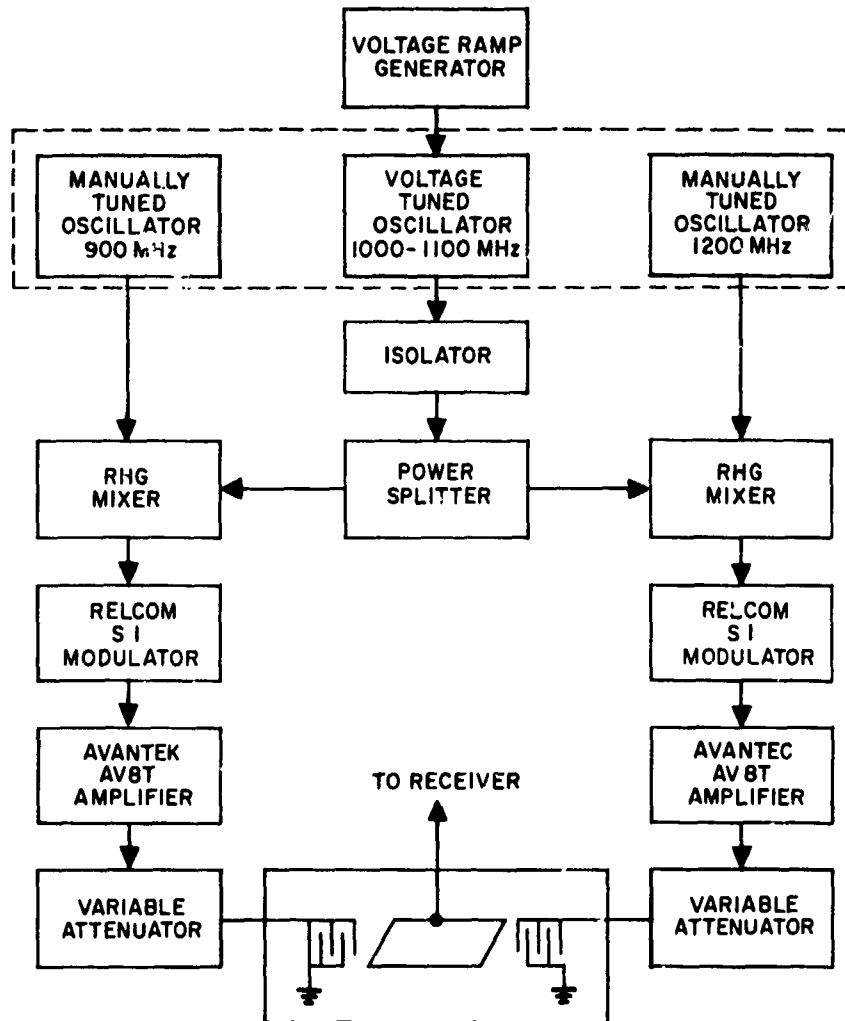


Fig. 43. Pulse Compression Test Schematic.

operations such as pulse compression, but we stopped development at an optimum point where a linear sweep over 20 MHz was more than the acceptance bandwidth of our receiver. This is because of one subtlety ignored earlier in the program. If the input signal is swept from 100 to 120 MHz, the output signal that is at twice the frequency of the input will sweep from 200 to 240 MHz. Therefore, only 20 MHz input sweep completely fills the 40 MHz bandwidth of the receiver.

After the apparatus development was completed, an attempt was made to observe pulse compression over a swept 10 MHz bandwidth. Initially no signal was observed using the wideband receiver, consisting of a Hewlett-Packard mixer followed by a wideband receiver, and an RHG 40 MHz bandwidth (centered at 60 MHz) i. f. strip. By replacing the wideband i. f. strip with an RHG narrow band variable i. f. strip (1 to 6 MHz), we were able to detect a swept correlated signal which could then be tweaked up by varying the time positions of the gated swept rf pulses and the frequencies of the manually tuned oscillators which control the frequencies of the swept output signals. The system was designed originally so that the gating pulses just pass a portion (10 MHz) of the entire sweep ramp (100 MHz) for both the up-CHIRPed and the down-CHIRPed signals. Thus by varying either pulse position in time, the position of the spectrum transmitted into either end of the device could be translated. Varying the frequency of either manually tuned oscillator had a similar effect, except the pulse position could be used to select the most linear portion of the sweep. Once compression of the CHIRP pulse was observed, the wideband i. f. amplifier was reinstalled, and the signal was optimized by the process explained earlier.

Because of the high level nature of the leakage signals into the correlator channel from the input transducers, the wideband i. f. amplifier was found to ring. These ringing oscillations tended to obscure the compressed pulse due to saturation and overload of the i. f. amplifier. A number of changes in the bypass and coupling circuitry were suggested by the manufacturer and were tried with some degree of success, but the ringing was not completely eliminated.

However it was sufficiently reduced in amplitude that the correlation pulse in compressed form was clearly visible and occupied about half of the vertical deflection of the scope. Tricks such as gating the input to the receiver were tried with limited success, since they introduced ringing transients of sufficient magnitude to partially overload the receiver. Finally, some trial and error work on removing ground loops in the bias and power supply lines to the various oscillators and amplifiers in the system and some improvements in the device package led to a tolerable ringing level.

Some data taken with this system are shown in Fig. 44. The maximum output bandwidth of the system was 40 MHz, corresponding to an input bandwidth of 20 MHz (and the output frequency is twice the input frequency). The length of the input pulse which contained this range of frequencies was determined by increasing the input pulse width until no further change in the compressed pulse was seen. For the results of Fig. 44, this pulse length was 1.2  $\mu\text{sec}$ . The output time bandwidth product was thus 40, which should result in a compressed pulse of 0.03  $\mu\text{sec}$  width. The observed half-width is about 0.07  $\mu\text{sec}$ .

Our conclusion from this phase of the effort is that the use of pulse compression results in a precise way of determining the performance of the convolution filter only if the linearity of the dispersed input pulses is very precisely controlled. In retrospect, probably the best way of generating the pulse is to use a linear acoustic surface wave dispersive delay line as the source of the dispersed pulse. The fidelity of this pulse can be tested by using the same linear dispersive filter as a compression filter after frequency inversion using a local oscillator in the same manner discussed in this section.

However it was sufficiently reduced in amplitude that the correlation pulse in compressed form was clearly visible and occupied about half of the vertical deflection of the scope. Tricks such as gating the input to the receiver were tried with limited success, since they introduced ringing transients of sufficient magnitude to partially overload the receiver. Finally, some trial and error work on removing ground loops in the bias and power supply lines to the various oscillators and amplifiers in the system and some improvements in the device package led to a tolerable ringing level.

Some data taken with this system are shown in Fig. 44. The maximum output bandwidth of the system was 40 MHz, corresponding to an input bandwidth of 20 MHz (and the output frequency is twice the input frequency). The length of the input pulse which contained this range of frequencies was determined by increasing the input pulse width until no further change in the compressed pulse was seen. For the results of Fig. 44, this pulse length was 1.2  $\mu$ sec. The output time bandwidth product was thus 40, which should result in a compressed pulse of 0.03  $\mu$ sec width. The observed half-width is about 0.07  $\mu$ sec.

Our conclusion from this phase of the effort is that the use of pulse compression results in a precise way of determining the performance of the convolution filter only if the linearity of the dispersed input pulses is very precisely controlled. In retrospect, probably the best way of generating the pulse is to use a linear acoustic surface wave dispersive delay line as the source of the dispersed pulse. The fidelity of this pulse can be tested by using the same linear dispersive filter as a compression filter after frequency inversion using a local oscillator in the same manner discussed in this section.

## 5. DELIVERED DEVICES

Three versions of the convolution filter were constructed for delivery under the contract. These were as follows.

- A broadband design covering the frequency range of 95 to 180 MHz – The time delay between the two input transducers corresponds to a delay path of 7.1 cm or 21  $\mu$ sec. The coupling structure on this device is a parallelepiped plate that will detect a signal over 5.3 cm inches of delay, or 15.7  $\mu$ sec. The device is shown in Fig. 45.
- The input transducers in this design are an aperture weighted linear FM design. The design used in the delivered part is a modification of that which has been used in the studies throughout most of the present program. The redesign was effected when it was found that the small frequency dependent insertion loss of this design of about 2 dB/octave in the earlier experiments became significantly worse when the delay between input transducer waves increased from 9 to 21  $\mu$ sec. At 21  $\mu$ sec delay, the insertion loss dropped off at the rate of 5 dB/octave. The design was modified by changing the aperture weighting in such a way as to insert a theoretical positive slope of 5 dB/octave. The remedy was successful, and the insertion loss of the device as a delay line is now substantially flat with frequency, except for some ripples in the passband.
- A narrow band design using periodic input transducers with 5-finger-pairs with a nominal center frequency of 150 MHz – The true measured center frequency is 146 MHz. Simple series tuning inductors have been provided for use at the two inputs to the device. The delay between transducers is 18.9  $\mu$ sec, and the

M8616

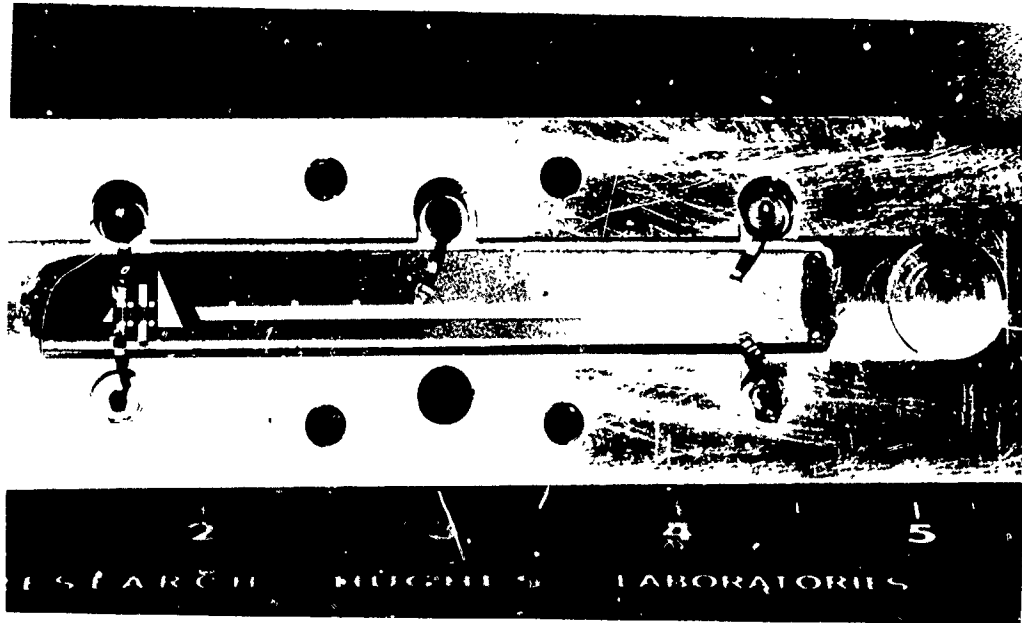


Fig. 45. Broadband Plate Coupled Convolver.

coupling plate will accommodate a signal of 16  $\mu$ sec duration. This device was shown in Fig. 30. A stripline tuner has been provided which can be used at the output terminal of this device. The tuner consists of a length of stripline with an adjustable short at the end and an intermediate adjustable tap from which the output is to be obtained.

- A narrow band design using periodic input transducers with 7-finger-pairs centered at a frequency of 195 MHz - Again simple series tuning inductors have been provided for use at the inputs. The output should be tuned with the stripline tuner. The delay between transducers is 15  $\mu$ sec, and the coupling plate will accommodate an 8  $\mu$ sec signal. This part was built in an attempt to minimize the conversion loss at the expense of bandwidth and convolution time.

Two tests have been performed on each of the devices:

- The insertion loss using the device as a delay line was measured on a Hewlett-Packard Network Analyzer. In this case one input port was used as an input and the other input port was actually used as the output of the delay line.
- The conversion efficiency was measured using the test procedure that was outlined in an earlier report. In this procedure, one measures the quantity  $P_{out} / P_{in1} P_{in2}$  as a function of frequency.  $P_{out}$  is the peak convolution output power for rectangular input pulses of fixed deviation. The pulse length in the tests was 5  $\mu$ sec. The  $P_{in1}$  and  $P_{in2}$  are the power levels at the input pulses. The two levels were kept the same in the tests. One modification of the earlier recommended procedure was incorporated in these tests. Namely, both inputs and the output terminal were padded with

a 3 dB attenuator. This was done to maintain a more nearly constant input and output impedance of  $50 \Omega$  in the presence of some impedance variations in the amplifiers driving the input and the output amplifier. For the narrow band design, the conversion efficiency was determined both with and without the output tuners. The results of these tests are displayed in the accompanying Figs. 46 through 50, and in Fig. 12 of Section 3. 2.

In general, the results are as expected from the work done in this program. However, the following conclusions may be noted:

- The broadband convolver shows a slowly varying oscillation of the gain with frequency. This is probably due to electrical resonance effects in the output circuit. The output capacitance of this structure shows a series resonance with the inductance of the input leads; moreover, the length of the coupling structure has become a significant fraction of an electrical wavelength.
- The 195 MHz narrow band convolvers show a ripple in the passband on the high frequency side of the band. This effect has uniformly showed up in several of these same devices, and is probably due to capacitance coupling to the convolution structure.
- Both of the narrow band convolvers have a greater insertion loss as a delay line than one would deduce from measurements of the input impedance. The additional loss is caused by losses in the aluminum film.

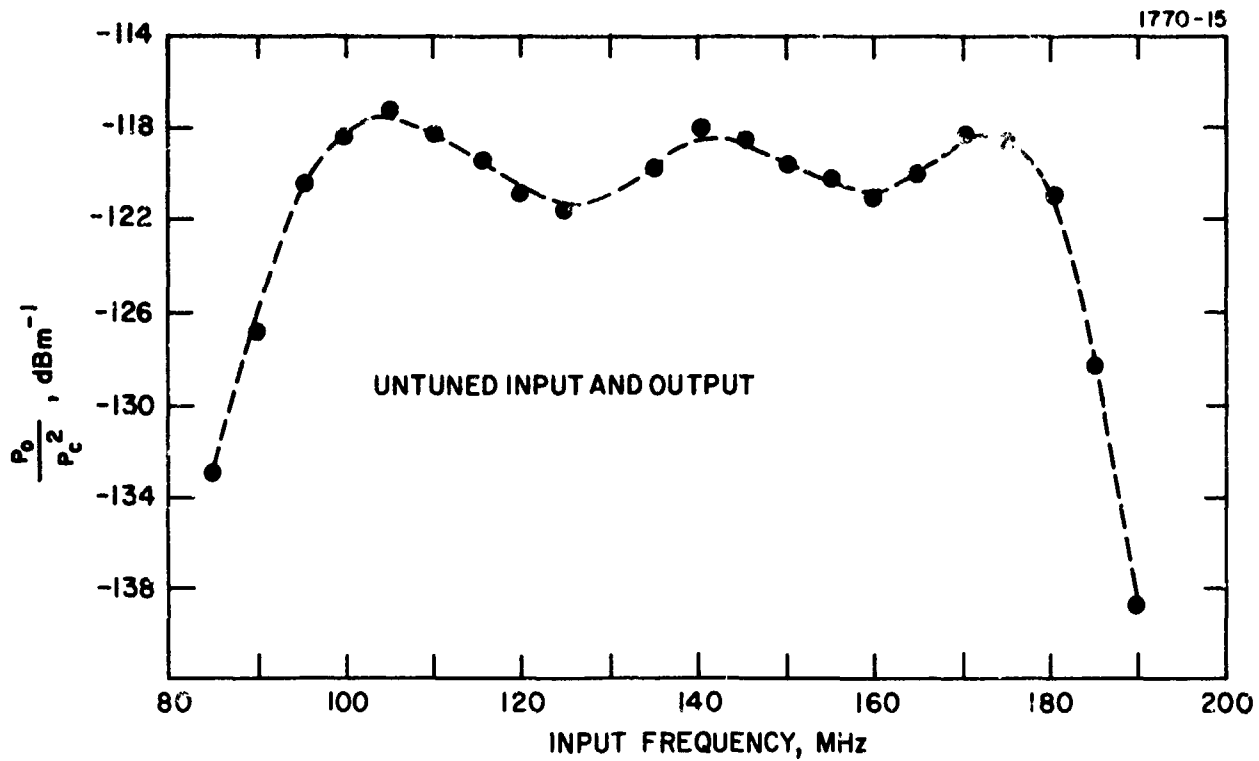


Fig. 48. Broadband Convolver: Convolution Efficiency for 5  $\mu$ sec Pulses.

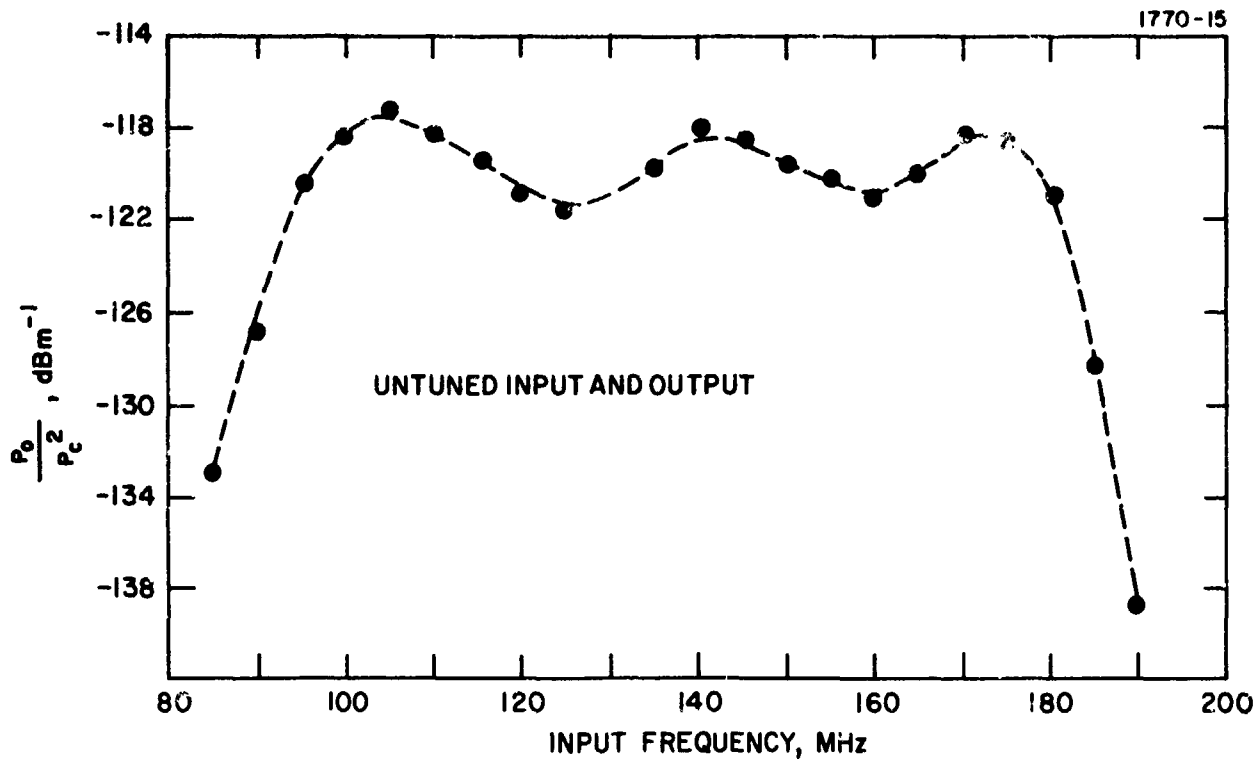


Fig. 48. Broadband Convolver: Convolution Efficiency for 5  $\mu$ sec Pulses.

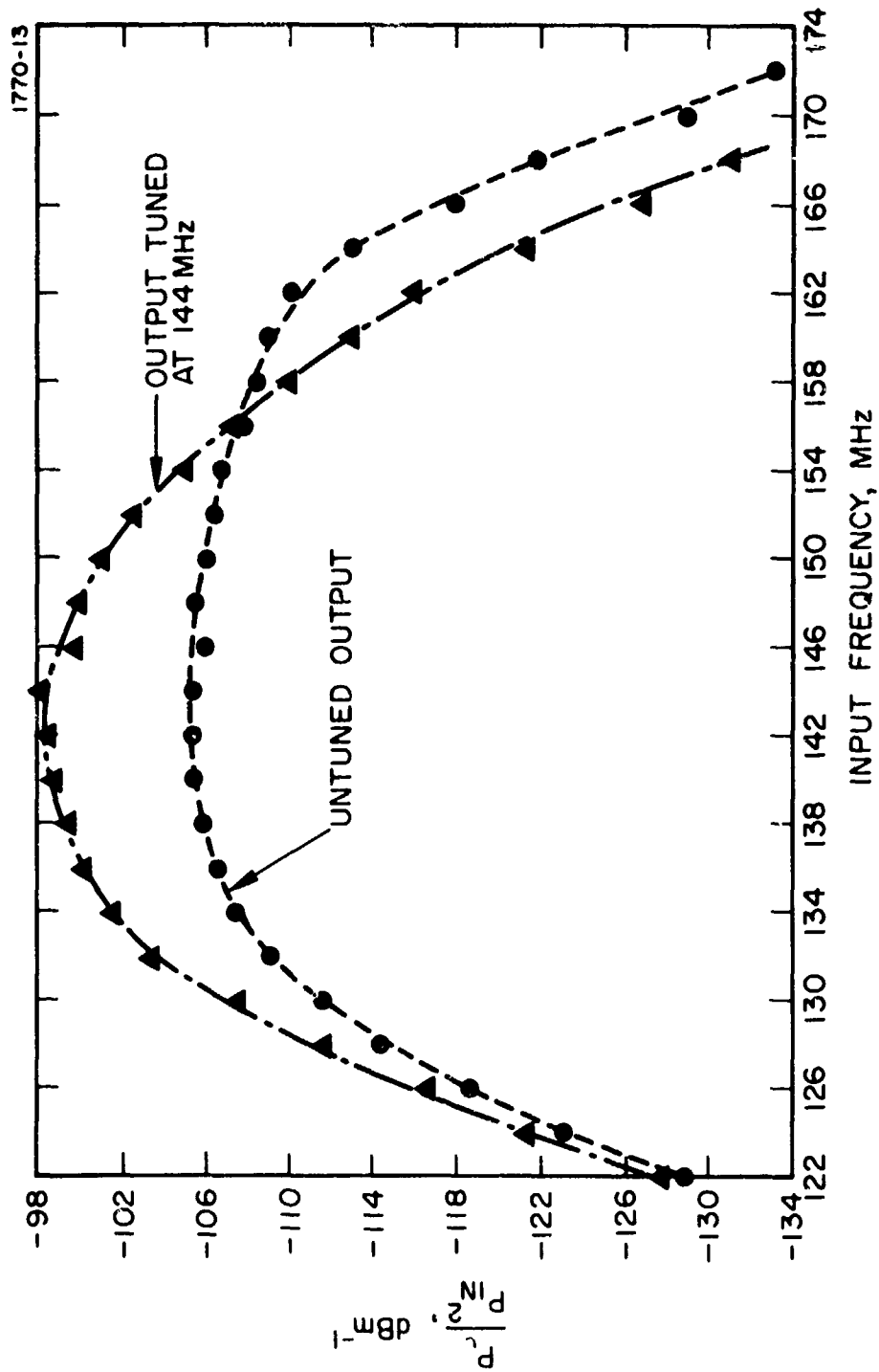


Fig. 49. Narrow Band Convolver: Convolution Efficiency for 5  $\mu$ sec Pulses.

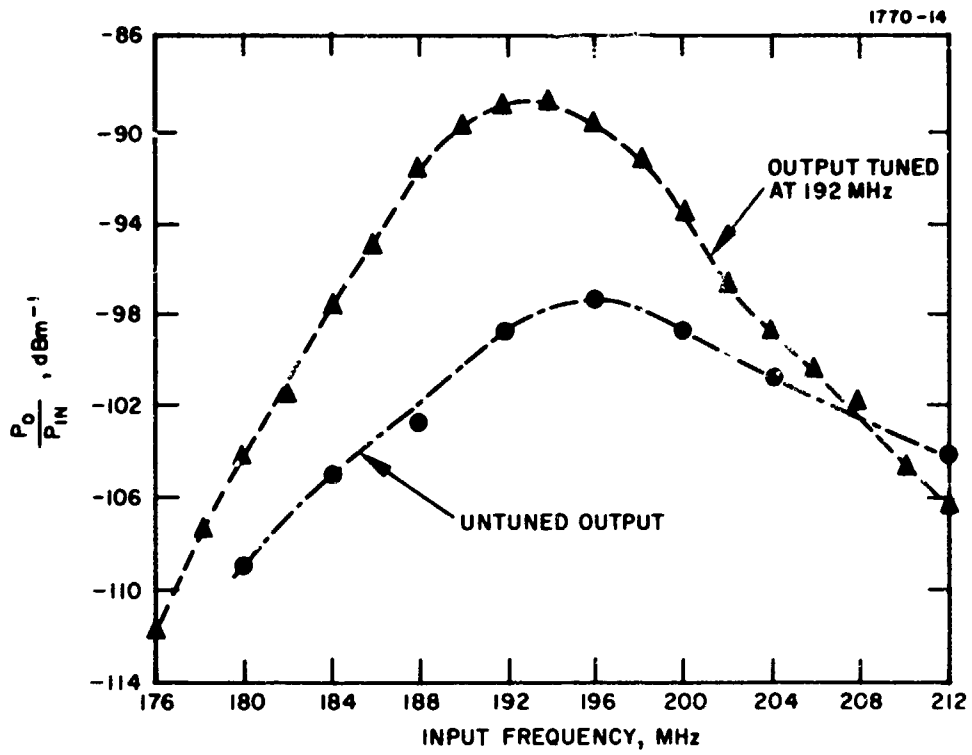


Fig. 50. Narrow Band Convolver: Convolution Efficiency for 5  $\mu$ sec Pulses, 195 MHz Design.

## REFERENCES

1. L. O. Svaasand, "Interaction Between Elastic Waves in Piezoelectric Materials," *Appl. Phys. Letters* 15, 300 (1969).
2. M. Luukkala and G. S. Kino, "Convolution and Time Inversion using Parametric Interactions of Acoustic Surface Waves," *Appl. Phys. Lett.* 18, 393 (1971).
3. M. Luukkala, "Nonlinearity Parameters in Surface Wave Convoluters and Correlators," 1971 IEEE Ultrasonics Symposium, Dec. 1971.
4. H. J. Shaw, "Parametric Acoustic Interactions: A New Approach to Signal Processing" 1970 IEEE Ultrasonics Symposium, Oct. 1970.
5. C. F. Quate and R. B. Thompson, "Convolution and Correlation in Real Time with Nonlinear Acoustics" *Appl. Phys. Lett.* 16, 494, June 1970.
6. W. L. Bongiani, *Proc. IEEE Letters*, 59, 713, April 1971.
7. W. R. Smith, H. M. Gerard, and W. R. Jones, "Analysis and Design of Dispersive Interdigital Surface Wave Transducers," Hughes Aircraft Company Technical Report TP 71-14-12, June 1971.
8. E. G. H. Lean, C. C. Tseng, and C. G. Powell "Optical Probing of Acoustic Surface Wave Harmonic Generation," *Appl. Phys. Lett.* 16, 32, Jan. 1970.
9. G. S. Kino, W. R. Shrene, and M. V. Luukkala, "Surface Wave Parametric Signal Processing," *Electronics Letters* 7, 704, Nov. 1971.
10. M. Waldner, M. E. Pedinoff, and W. R. Jones "Surface Wave Propagation in Layered Media," presented at IBM Conference on Surface Waves, March 1970.
11. W. R. Smith, Stanford Report, ML 1821.

## APPENDIX

### GENERAL APERIODIC TRANSDUCER DESIGN: NONAPERTURE WEIGHTED

This appendix describes the design of transducers based upon a general aperiodic construction in which aperture weighting is not required to obtain flat, broadband response. The designs were based upon some independent research done at the Hughes Aircraft Company. One of the designs has been tested subsequent to the completion of the present program, and the results of this test are also presented.

The alternate approach, which is described here, used aperture weighting only at the ends of the array (if at all) to reduce the passband ripple associated with a finite structure. In the array described here approximately 10% of the fingers at the extreme ends were tapered to prevent sharp discontinuities and the associated Fresnel type ripple. All other electrodes in the transducer are of constant length equal to the optimum for the device.

This technique allows a reduced conversion loss to be obtained for a given number of electrodes or total capacitance, and simplifies the fabrication of the transducer mask while circumventing the problems given above.

The technique employed involves varying the number of transducer elements that are synchronous in any given frequency band so as to provide the desired conversion loss versus frequency.

In general it is convenient to use a computer solution to calculate the finger positions within the array, but the approach can be understood by considering the approximate equation given below for relative conversion efficiency of the transducer:

$$T(\omega) = \sum_{n=1}^N (-1)^n K F \omega^{1/2} \operatorname{sinc} \left( \frac{\omega l_n}{2v} \right) \exp \left( -j \frac{\omega L_n}{v} \right) \quad (\text{A-1})$$

where

$T(\omega)$  = the relative conversion efficiency at frequency  $\omega$

$N$  = total number of elements in the array

$K$  = electromechanical coupling coefficient

$F$  = filling factor

$l_n$  = electrode spacing

$L_n$  = electrode position

$v$  = acoustic velocity

The full equivalent circuit on which the above expression is based and the symbols used are described by Smith, et al. <sup>\*</sup> It should be noted that if a nonlinear field approximation is used rather than the flat field assumptions implicit in eq. (A-1), the sinc function is more correctly replaced by  $J_0$ , the zero order Bessel function. This refinement leads to slightly improved agreement between experimental results and calculation.

However, in either case, the properties of the summation given in eq. (A-1) determine the response at any frequency  $\omega$ . The elements of this summation for a broadband array with 120 fingers are shown in Fig. A-1. Here each element is drawn as a vector on a polar plot and the summation is given by the vector AA' joining the response of the first and last fingers. It can be seen that only those elements between  $N_1$  and  $N_2$  contribute effectively to the response, the phases

---

<sup>\*</sup>W. R. Smith, H. M. Gerard, J. H. Collins, T. M. Reeder, and H. J. Shaw, "Analysis of Interdigital Surface Wave Transducers by Use of an Equivalent Circuit Mode," IEEE Trans. MTT-17, 856-865 (1969).

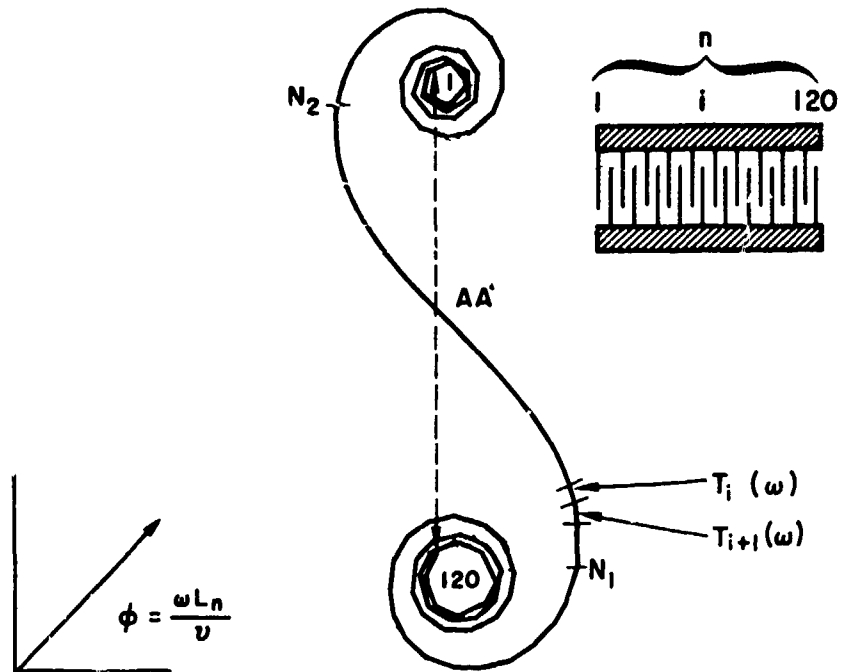


Fig. A-1. Characteristics of Summation Given in eq. (A-1) Illustrating Effect of Phase Rotation of Summated Elements.

of elements outside this range are such that their prime contribution is to the ripple. Hence we can write

$$T(\omega) = T_o(\omega) + \tilde{T}(\omega) \quad (\text{A-2})$$

where

$$T_o(\omega) = \sum_{n=N_1}^{N_2} KF \omega^{1/2} \text{sinc} \left( \frac{\omega l_n}{v} \right) \exp \left( j \frac{\omega L_n}{v} \right) \quad (\text{A-3})$$

$$\approx KF \omega^{1/2} N(\omega) \quad (\text{A-4})$$

$N(\omega) = N_2 - N_1$  is the effective number of fingers at  $\omega$  and  $\tilde{T}(\omega)$  represents the ripple.

Further, if cosine type weighting (for instance) is employed at the ends to reduce the passband ripple  $\tilde{T}(\omega)$  to a sufficiently low level, the conversion efficiency becomes approximately proportional to  $T_o(\omega)$  and hence  $N(\omega) \omega^{1/2}$ .

Thus, by varying the number of effective fingers as a function of frequency across the band, the insertion loss can be made to vary in a predetermined manner without apodization.

As a demonstration of this approach, a transducer with a nominally flat passband was designed. (The conventional linear FM design for this requires a cubic  $(f_o^3/f^3)$  apodization across the band, resulting in a more complex transducer and loss of efficiency, etc.) The device has 120 finger elements, of which approximately 10% at the ends were apodized with (cosine)<sup>2</sup> weighting to reduce passband ripple. All other fingers had equal apertures of 0.06 in. The nominal flat passband width was designed to be 75 MHz at 155 MHz. The calculated response using the full equivalent three-port network described by Smith et al.<sup>A-1</sup> is given in Fig. A-2(a). The measured response of a delay line with two such identical arrays and approximately 10  $\mu$ sec delay on  $\text{LiNbO}_3$  is shown in Fig. A-2(b). As can be seen, the over-all measured slope

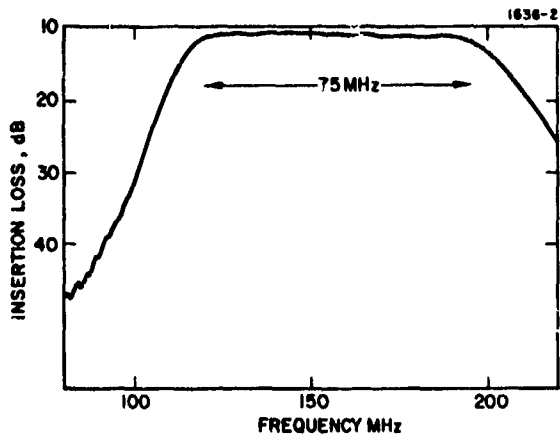
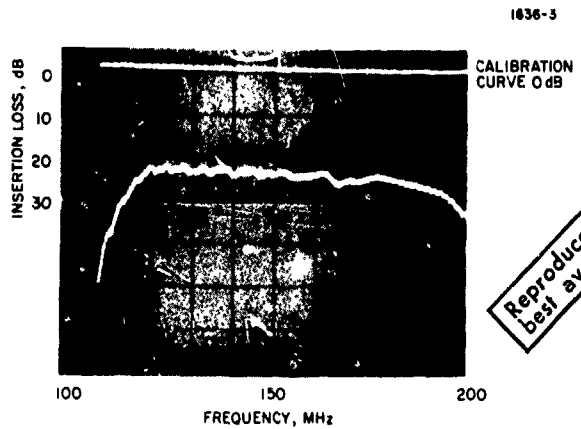


Fig. A-2(a).  
 Conversion Loss for Flat  
 Passband Design Calculated  
 using Three-Port Network  
 after Smith, et al.

Fig. A-2(b).  
 Measured Insertion Loss  
 for Unapodized Design.



Reproduced from  
 best available copy

across the band is approximately 1 dB. (A calibration curve of 0 dB is also included on the photograph for reference.) This slope was not predicted from the theoretical analysis and could result from the transducer leads or differential propagation loss across the band. However, it compares with a variation of approximately 10 dB for an equivalent unapodized linear FM array.

The aperture of the array is shown in Fig. A-3 together with an equivalent linear FM design for the same passband. The shaded area represents space wasted in the linear FM design where no coupling takes place due to apodization. In this case it amounts to about 40% of the total area. In a linear FM design, the number of effective fingers increases across the band as

$$\left[ \frac{2DTf^2}{B} \right]^{1/2}$$

where DT and B are the transit time and total bandwidth of the array, respectively. Hence, very coarse apodization is required to flatten the response, resulting in very significant changes in beam width (about four to one for this case).

In conclusion, it should be stated that the approach described above cannot be applied directly in cases where both the frequency and phase characteristics are specified independently, since the procedure is analogous to phase weighting within the band. However, in many applications this approach can be used to tailor the insertion loss within the filter, with increased efficiency and constant beam width.

This design then would be adequate for incorporation in a convolution filter using a plate coupler. If this type of design is to be incorporated into a design with a coarse grating coupler, a special problem arises because the center frequencies of the two input transducers to such a device must be displaced by a frequency corresponding to the periodicity of the coarse grating structure. The solution of this problem is described in the following.

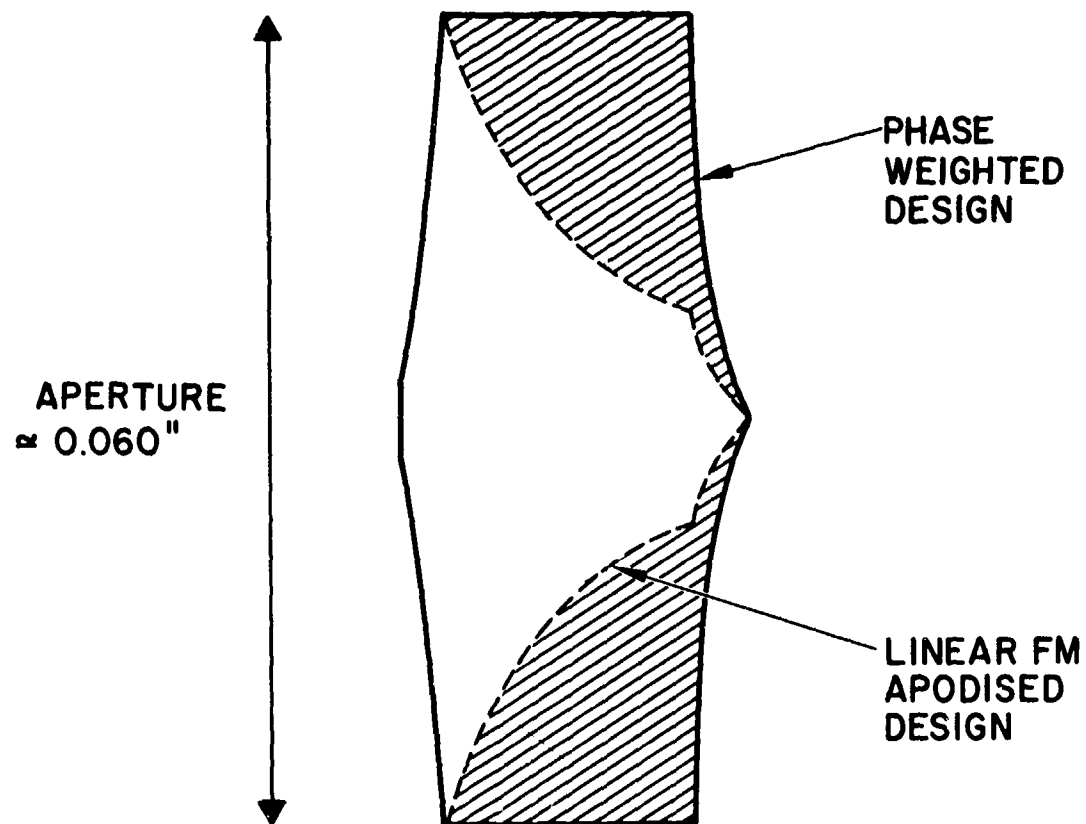


Fig. A-3. Comparison of Over-All Area of Unapodized and Linear FM Design for Equivalent Passband Characteristics.

In order that the signals to be convolved arrive at the output coupler with the correct time distribution, the two input transducers must have proportional frequency versus position characteristics.

The problem is illustrated again in Fig. A-4, where the coupler is shown to be resonant at frequency  $F_0$ . This implies that

$$F'_{\min} - F'_{\max} = F''_{\min} - F''_{\max} = F_0 \quad (\text{A-5})$$

and for effective correlation .

$$F_1 \left( -\frac{L}{2} - \Delta - \delta \right) - F_2 \left( \frac{L}{2} + \Delta + \delta \right) = F_0 \quad (\text{A-6})$$

where  $F_1(x)$  and  $F_2(x)$  are the synchronous frequencies of the first transducers and second transducers, respectively, as a function of position  $x$ . In this case, frequency components spaced by  $F_0$  Hz will cross at the center of the coupler. Obviously with a plate coupler,  $F_0 = 0$ , the two transducers are identical, and both eqs. (A-5) and (A-6) obtain directly.

The design technique to achieve correct correlation when  $F_0 = 0$  is illustrated by reference to a design where

$$\begin{aligned} F'_{\min} &= 140 \text{ MHz} & F''_{\min} &= 200 \text{ MHz} \\ F''_{\min} &= 110 \text{ MHz} & F'_{\min} &= 170 \text{ MHz} \end{aligned} \quad (\text{A-7})$$

and

$$F_0 = 30 \text{ MHz}$$

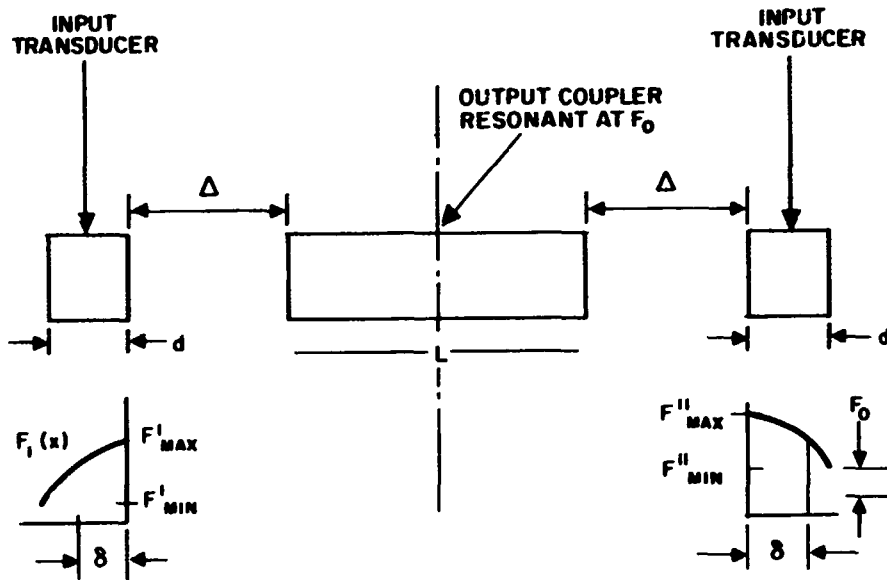


Fig. A-4. Schematic Illustrating the Necessary Timing Relation for Convolver.

The designs in this case were chosen to be spaced at  $\pm 15$  MHz; the phase change  $\Phi(x)$  across the transducer as a function of distance along the transducer can be calculated as

$$\Phi(x) = 2\pi \int_0^d f_{\text{sync}}(x) dx \quad (\text{A-8})$$

where  $f(x)$  is the synchronous frequency at position  $x$ . Then for the shifted transducers

$$f'_{\text{sync}}(x) = f_{\text{sync}}(x) \pm F_0 \quad (\text{A-9})$$

Therefore,

$$\left. \begin{aligned} \Phi'(x) &= 2\pi \int_0^d \left| f_{\text{sync}}(x) + F_0 \right| dx \\ \Phi''(x) &= 2\pi \int_0^d \left| f_{\text{sync}}(x) - F_0 \right| dx \end{aligned} \right\} \quad (\text{A-10})$$

Equation (A-10) gives the phase change as a function of distance of the shifted transducers of length  $d$  such that

$$f'_{\text{sync}}(x) - f''_{\text{sync}}(x) = F_0$$

for all positions  $x$  within the transducer. It remains only to find the position of the fingers that correspond to eq. (A-10). Since for a two-terminal device the fingers must be at phase intervals of  $\pi$ , the finger positions are given by  $x'_n$  and  $x''_n$ , where  $n$  is an integer and

$$\Phi'(x_n) - \Phi'(x_{n-1}) = \pi$$

$$\Phi''(x_n) - \Phi''(x_{n-1}) = \pi$$

The final response can then be calculated. The results of this are shown in Figs. A-5 and A-6 for the two transducers, based upon the original design.

It should be noted that the number of fingers in each transducer will be different, whereas the frequency time characteristics will be proportional.

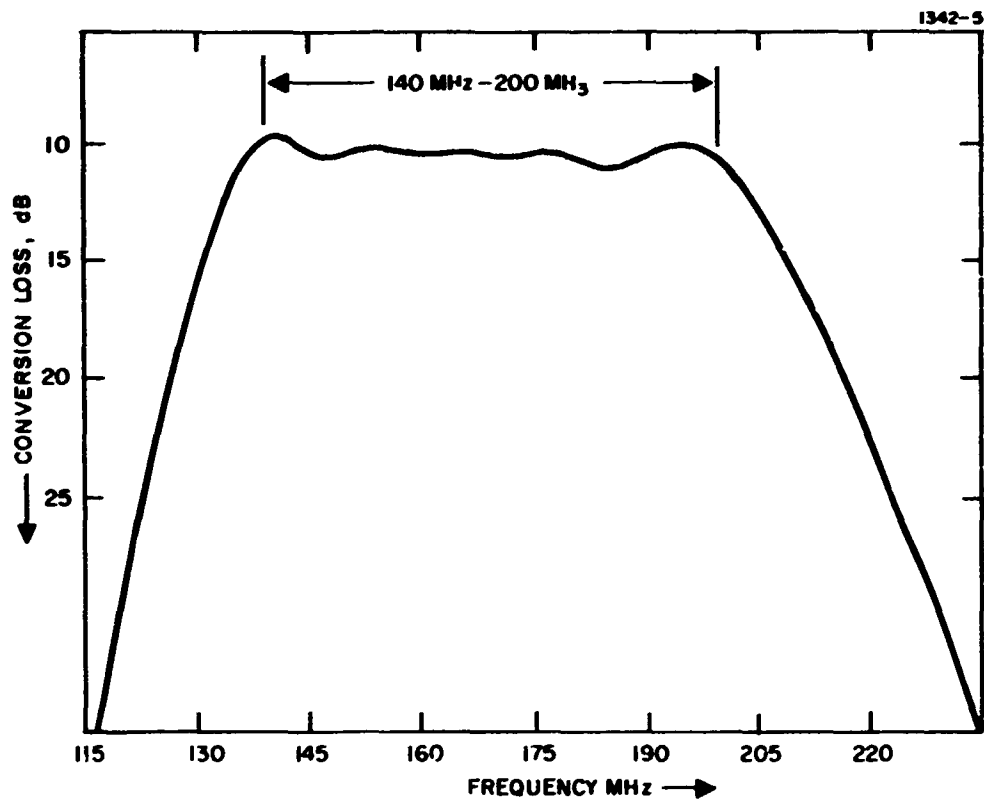


Fig. A-5. Response of Shifted Transducer for Coupling Structure Resonant at 30 MHz High Side.

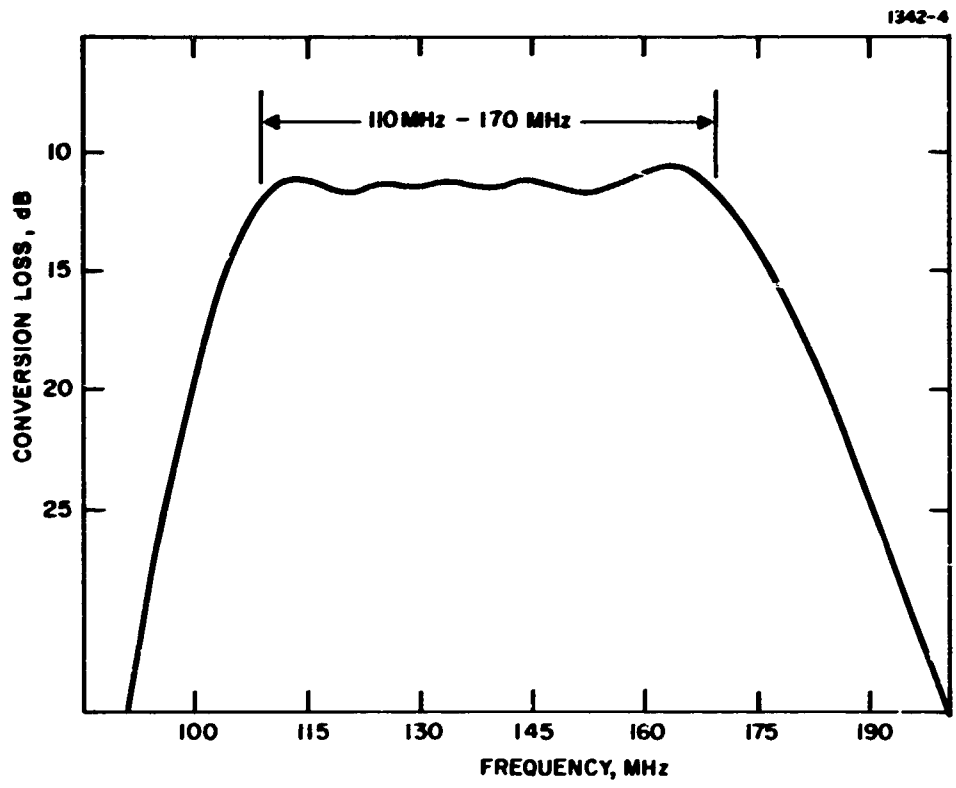


Fig. A-6. Response of Shifted Transducer for Coupling Structure Resonant at 30 MHz Low Side.